Momentum Transport in Gyrokinetic Turbulence

Von der Universität Bayreuth
zur Erlangung des Grades eines
Doktors der Naturwissenschaften (Dr. rer. nat.)
genehmigte Abhandlung

von

Rico Buchholz
aus Rüdersdorf

Contents

List of Figures

List of Tables

Acknowledgements

I thank my advisor Prof. Dr. A. G. Peeters for his support, help and useful discussions.
Thanks to Dr. William Hornsby, Dr. Pierluigi Migliano, Stefan Grosshauser, F. J. Casson and Arne Weikel for their tips and helpful discussions.
For the good cooperation thanks to Walter Guttenfelder.
Furthermore I thank Tobias Sung.
Last but not least I thank F. D. C. Willard for many helpful discussions.

Abstract

In this thesis, the gyrokinetic-Vlasov code GKW is used to study turbulent transport, with a focus on radial transport of toroidal momentum. To support the studies on turbulent transport an eigenvalue solver has been implemented into GKW. This allows to find, not only the most unstable mode, but also subdominant modes. Furthermore it is possible to follow the modes in parameter scans. Furthermore, two fundamental mechanisms that can generate an intrinsic rotation have been investigated: profile shearing and the velocity nonlinearity.
The study of toroidal momentum transport in a tokamak due to profile shearing reveals that the momentum flux can not be accurately described by the gradient in the turbulent intensity. Consequently, a description using the profile variation is used. A linear model has been developed that is able to reproduce the variations in the momentum flux as the profiles of density and temperature vary, reasonably well. It uses, not only the gradient length of density and temperature profile, but also their derivative, i.e. the second derivative of the logarithm of the temperature and the density profile. It is shown that both first as well as second derivatives contribute to the generation of a momentum flux. A difference between the linear and nonlinear simulations has been found with respect to the behaviour of the momentum flux. In linear simulations the momentum flux is independent of the normalized Larmor radius ρ_*, whereas it is linear in ρ_* for nonlinear simulations, provided ρ_* is small enough ($\leq 4 \cdot 10^{-3}$). Nonlinear simulations reveal that the profile shearing can generate an intrinsic rotation comparable to that of current experiments. Under reactor conditions, however, the intrinsic rotation from the profile shearing is expected to be small due to the small normalized Larmor radius $\rho_* \lesssim 5 \cdot 10^{-4}$.
The velocity nonlinearity has been derived and the implementation in GKW has been tested. Simulations at $\rho_* = 10^{-3}$ did not show a significant momentum transport, contrary to what would be expected due to the breaking of symmetry.
Finally, the influence of rotation on particle and momentum transport has been studied, with a focus on the effects caused by the centrifugal force at parameters that represent experiments in NSTX. While the growth rates and frequencies are not strongly affected by the centrifugal effects, they have a strong influence on the particle and momentum flux. For the carbon impurity a hollow density profile has been observed in NSTX. This observation can be explained if centrifugal

effects are kept in the description of the unstable modes. In the modelling of the toroidal momentum transport it has, furthermore, been shown that a "nonlinear term" proportional to the product of the toroidal rotation and its radial gradient (i.e. $\propto u \cdot u'$) can have a significant influence, as it will generate a substantial inward flux of toroidal momentum.

Abstract (German)

Im Rahmen dieser Arbeit wurde der gyrokinetische Vlasov Code GKW benutzt, um turbulenten Transport zu studieren, mit Fokus auf radialen Transport von toroidalem Impuls. Zur Unterstützung der Studien des turbulenten Transports wurde ein Eigenwertlöser in GKW implementiert. Dieser ermöglicht es nicht nur die instabilste Mode zu finden, sondern auch solche mit geringeren Wachstumsraten. Desweiteren ist es möglich die Moden in Parameterscans zu verfolgen.
Es wurden zwei fundamentale Mechanismen untersucht, welche intrinsische Rotation erzeugen können: Profileshearing und die Geschwindigkeitsnichtlinearität. Die Untersuchung von toroidalem Impulstransort in einem Tokamak aufgrund von Profileshearing enthüllt, dass der Impulsfluss nicht akkurat durch den Gradienten der Turbulenzintensität beschrieben werden kann. Aufgrund dessen wurde eine Beschreibung genutzt, welche sich auf Profilvariationen stützt. Ein lineares Model wurde entwickelt, welches in der Lage ist die Variationen im Impulsfluss aufgrund von Variationen im Profil von Dichte und Temperatur, hinreichend genau zu beschreiben. Dieses Model verwendet nicht nur die Gradientenlänge des Dichte- und Temperaturprofils, sondern auch deren Ableitung, also die zweite Ableitung des Logarithmus von Temperatur- und Dichteprofil. Es wurde gezeigt, dass sowohl die erste als auch die zweite Ableitung Beiträge zur Erzeugung des Impulsflusses leisten. Ein Unterschied zwischen linearen und nichtlinearen Simulationen wurde gefunden, in Hinblick auf das Verhalten des Impulsflusses. In linearen Simulationen ist der Impulsfluss unabhänging vom normalisierten Larmorradius ρ_*, wohingegen er für nichtlineare Simulationen linear in ρ_* ist, solange ρ_* klein genug ist ($\leq 4 \cdot 10^{-3}$). Nichtlineare Simulationen zeigen, dass Profileshearing intrinsische Rotation erzeugen kann, die vergleichbar mit experimentell gefundenen Werten ist. Es wird erwartet, dass unter Reaktorbedingungen die vom Profileshearing erzeugte intrinsische Rotation klein ist,da der normalisierten Larmorradius $\rho_* \lesssim 5 \cdot 10^{-4}$ klein ist.
Die Geschwindigkeitsnichtlinearität wurde analytisch hergeleitet und die Implementierung in GKW getestet. Simulationen für $\rho_* = 10^{-3}$ zeigen keinen signifikanten Impulsfluss, entgegen den Erwartungen aufgrund der Symmetriebrechung. Schließlich wurde der Einfluss der Rotation auf Teilchen- und Impulstransport, für Parameter aus einem Experiment an NSTX, untersucht, insbesondere die Effekte die durch die Zentrifugalkraft verursacht werden. Während Wachstumsrate

und Frequenz durch die zentrifugalen Effekte nur schwach beeinflusst werden, haben die zenrifugalen Effekte einen starken Einfluss auf Teilchen- und Impulsfluss. Die Beobachtung, dass ie Kohlenstoffverunreinigung in NSTX ein hohles Dichteprofil haben, kann erklärt werden, wenn zentrifugale Effekte in den Simulationen berücksichtigt werden. Bei der Modellierung des toroidalen Impulstransportes wurde desweiteren gezeigt, dass ein "nichtlinearer Term", proportional zum Produkt aus toroidaler Rotation und radialem Gradienten der Rotation (also $\propto u \cdot u'$) signifikanten Einfluss haben kann, da dieser Term einen erheblichen, zur Mitte gerichteten, Impulsfluss erzeugt.

Declaration

This thesis is my own work, exceptions are marked as such. A part of this work has been published earlier in a peer reviewed journal. Namely Ch. 4 and 6 are based on
R. Buchholz, Y. Camenen, F. J. Casson, S. R. Grosshauser, W. A. Hornsby, P. Migliano and A. G. Peeters, *Toroidal momentum transport in a tokamak due to profile shearing*, Physics of Plasmas **21**, 062304 (2014)
and
R. Buchholz, S. Grosshauser, W. Guttenfelder, W. A. Hornsby, P. Migliano, A. G. Peeters and D. Strintzi, *Influence of centrifugal effects on particle and momentum transport in National Spherical Torus Experiment*, Physics of Plasmas **22**, 082307 (2015),
respectively.

It is noted that Fig. 6.1 was not created by the author of this thesis. Also is noted that Fig. 2.2 has been added to the documentation of GKW.

Chapter 1

Introduction

The energy demand of the earths population increases and, at the same time, there are problems connected with the current energy sources. Coal, gas and oil produce CO_2 and thus enhance global warming. Nuclear fission has security issues and problems with waste disposal. Solar and wind energy on the other hand have the drawback of a fluctuating power output, so without appropriate means of storing, they can not supply the base energy consumption. Thus there are two solutions for the energy problem

- better storages for (electrical) energy
- new types of power plants.

A fusion power plant is a new type of power plant. Although researched for decades, a breakthrough has not yet been achieved, despite considerable progress [1, Fig. 1].
In a fusion reaction light elements are fused to heavier elements, where the sum of mass reduces in the reaction, and is set free as energy in the form of radiation and/or kinetic energy of the products. The energy yields for some important fusion reactions [2, 3] are given in (1.1)-(1.6):

$$\mathrm{D} + \mathrm{D} \rightarrow \mathrm{T}(1.0\mathrm{MeV}) + \mathrm{p}(3.03\mathrm{MeV}) \tag{1.1}$$
$$\mathrm{D} + \mathrm{D} \rightarrow {}^3\mathrm{He}(0.82\mathrm{MeV}) + \mathrm{n}(2.45\mathrm{MeV}) \tag{1.2}$$
$$\mathrm{T} + \mathrm{D} \rightarrow {}^4\mathrm{He}(3.52\mathrm{MeV}) + \mathrm{n}(14.06\mathrm{MeV}) \tag{1.3}$$
$$\mathrm{D} + {}^3\mathrm{He} \rightarrow {}^4\mathrm{He}(3.67\mathrm{MeV}) + \mathrm{p}(14.67\mathrm{MeV}) \tag{1.4}$$
$${}^6\mathrm{Li} + \mathrm{n} \rightarrow \mathrm{T} + {}^4\mathrm{He} + 4.8\mathrm{MeV} \tag{1.5}$$
$${}^7\mathrm{Li} + \mathrm{n}(2.5\mathrm{MeV}) \rightarrow \mathrm{T} + {}^4\mathrm{He} + \mathrm{n} \tag{1.6}$$
$$\mathrm{H_2} + \frac{1}{2}\mathrm{O_2} \rightarrow \mathrm{H_2O} + 2.96\mathrm{eV} \tag{1.7}$$
$$2\mathrm{C_8H_{18}} + 25\mathrm{O_2} \rightarrow 16\mathrm{CO_2} + 18\mathrm{H_2O} + 94\mathrm{eV} \tag{1.8}$$

Here p is a proton (or ionised hydrogen), n a neutron, D and T represent deuterium and tritium, respectively. Reactions (1.5) and (1.6) are breeding reactions for tritium. Note that the latter one, involving the more common isotope ^{7}Li, requires energy. The chemical reaction of hydrogen and oxygen to water (1.7), as well as the combustion of a typical hydrocarbon in petrol (1.8), have been added for comparison. It is easy to see that the released energies are $5-6$ orders of magnitude bigger in the fusion reactions.
Although fusion can potentially generate a high amount of energy, a fusion reaction is not easily achieved. The central problem is to overcome the Coulomb repulsion of the atoms. At each collision between the atoms, there is a chance for a fusion reaction. The chance, described by a cross section, depends on the energy of the particles. The product of collision rate and cross section is thus important and called fusion rate or reactivity. The fusion rate is shown in Fig. 1.1 as a function of temperature for three basic fusion reactions, namely Eq. (1.3), (1.1)+(1.2) and (1.4). As can be seen, the fusion of deuterium and tritium has

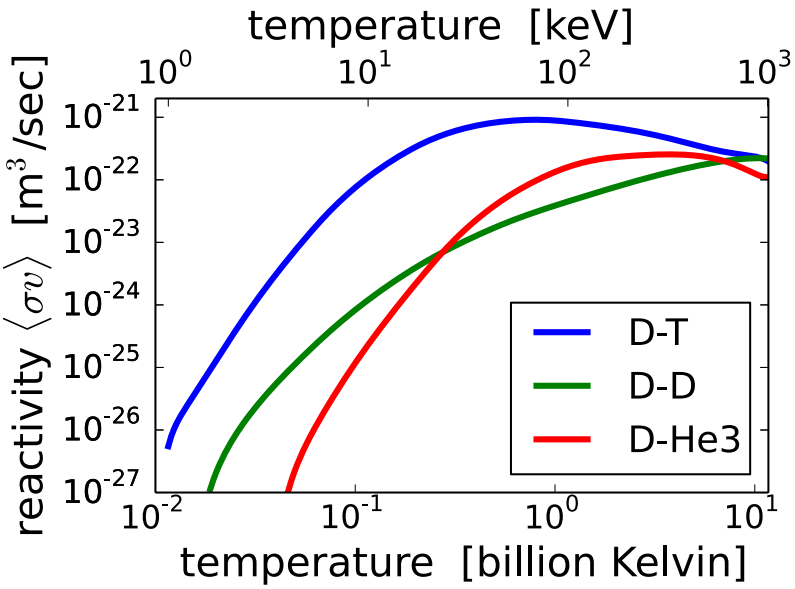

Figure 1.1: Fusion rate $\langle\sigma\nu\rangle$ over temperature for the processes of Eq. (1.3), (1.1)+(1.2) and (1.4), respectively. (from https://en.wikipedia.org/wiki/Nuclear_fusion, 2015/10/01)

the highest reactivity. For this reason the D-T reaction is often proposed for fusion power plants.
Despite the high energy yield (per reaction and per mass) of fusion reactions, still many reactions per second are necessary in a power plant. As can be seen, at a temperature of about $10-100$keV the reactivity has a maximum. As the cross

section at a given temperature is fixed, the only remaining lever for increasing the energy production is the collisionality, which can be increased by increasing the density. Temperature and density alone are not enough to quantify how close the system is to a sustained fusion reaction. There will be energy losses that have to be compensated. How big these are, is measured by the energy confinement time τ. The so called triple product $nT\tau$ of the tree quantities density, temperature and energy confinement time is used to determine the quality of a fusion plasma. This could be increased by about five orders of magnitude (see for example Fig. 1 of Ref. [1]) over the last five decades.
A key ingredient to the increase in the triple product is better confinement, as this affects not only the (energy) confinement time, but also the density and temperature that can be achieved. Because of the necessary temperature of $10^8 - 10^9$K, the reactor fuel is in the plasma state and can not easily be confined. If the particles can move freely, then the confinement times would be of the order of device size divided by particle velocity (which can reach up to 10% of the speed of light for electrons). A magnetic field is thus used to confine the plasma.
The next section gives an overview of the physics of a particle in a magnetic field, more details can be found in Ref. [4].

1.1 Magnetic confinement and drifts

A charged particle in a magnetic field can move freely along the magnetic field, while the velocity perpendicular to the magnetic filed is constrained by the Lorentz force, generating a rotating motion around the magnetic field line, with Larmor radius

$$\rho = \frac{mv_\perp}{qB} \tag{1.9}$$

and (cyclotron) frequency

$$\Omega = \frac{qB}{m}. \tag{1.10}$$

If the field line 'ends' on a wall or if the radius of the circular motion around the field line is larger than the device, particles will be lost. By using a magnetic field that closes upon itself, having the topology of a doughnut, particle losses can be prevented, provided the field is strong enough.
The direction on the torus are referred to as toroidal (the long way round), poloidal (the short way round) and radial (perpendicular to the torus). Closing the field lines as described above, will result in a field that is purely toroidal, which is insufficient to effectively confine the plasma.
To understand this, the motion of a charged particle is investigated. Because of the toroidal geometry, the magnetic field strength decays as $1/R$, where the major

radius R is the distance to the symmetry axis of the torus. Since the curvature of the gyroorbit is inverse proportional to the magnetic field (see Eq. (1.9)), the gyromotion is not closed. Fig. 1.2 sketches the situation, for a sharp drop in the strength of the magnetic field. The gyroorbit is not closed and the particle

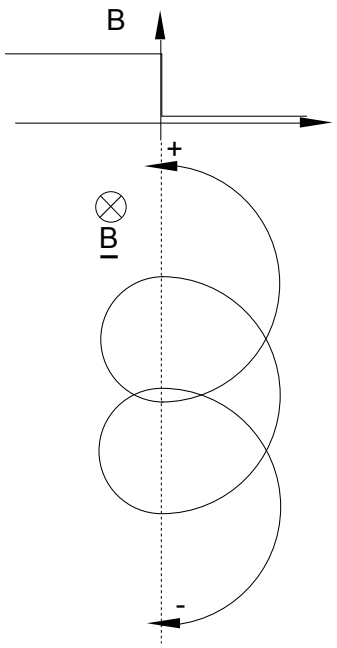

Figure 1.2: Sketch of the physical mechanism behind the gradient drift. The upper part shows the strength of the magnetic field over the radial direction. The lower part sketches the trajectory of a charged particle. The direction of the magnetic field is into the plane. Whether the particle drifts up- or downward, depends on its charge. A positive (negative) charged particle would rotate anticlockwise (clockwise) and thus drift upwards (downwards).

will drift upwards (downwards) if its charge is positive (negative). Because of the resulting charge separation an electric field is produced, which points downwards. The electric field will then cause a $E \times B$-drift

$$\underline{v}_E = \frac{1}{B^2}\underline{E} \times \underline{B}, \tag{1.11}$$

that is independent of the particle charge, and thus in the same direction for electrons and ions. This will be down the gradient of magnetic field strength, i.e. outward. Thus the whole plasma will move outward and the confinement is lost. The drifts above are caused by forces on the particle perpendicular to the magnetic field. The balance of a perpendicular force and the Lorentz force lead to a

drift [2]

$$\underline{u_F} = \frac{1}{qB}\underline{F} \times \hat{\underline{b}} \tag{1.12}$$

$$= -\frac{\underline{a} \times \hat{\underline{b}}}{\Omega} \tag{1.13}$$

with $\hat{\underline{b}}$ the unit vector in magnetic field direction. Important drifts are the already mentioned gradient drift (generated by the mirror force with $\underline{a}_{\nabla B} = -v_\perp^2/2(\nabla B)/B$) and $E \times B$ drift (generated by the force due to an electric field with $\underline{a}_{\underline{E}\times\underline{B}} = q\underline{E}/m$) and the curvature drift (generated by the centrifugal force with $\underline{a} = v_\parallel^2 \hat{\underline{n}}/R$, where $\hat{\underline{n}}$ is the negative of the normal vector from the Frenet-Serret frame, i.e. it points away from the centre).

1.2 Tokamak basics

The outward motion of the plasma can be prevented through the use of a poloidal magnetic field. This will cause the magnetic field lines to wind helically around the torus, with the surface which the field lines traces out referred to as magnetic surface. Good confinement is obtained if these surfaces are nested. It can be shown that the magnetic surfaces, are surfaces of constant poloidal magnetic flux. The latter can then be used as a surface label and one speaks of flux surfaces.
Two main methods to create the poloidal field have been developed, which results in two main device types. The first, called stellerator, deforms the field coils and gives up the toroidal symmetry. This leads to new challenges, as some conservation laws are no longer valid, which can result in the loss of particles. With careful design of the field coils and the fields, these losses can be minimized. As the geometry can get fairly complex, computers are widely used for the optimization. An example for a stellerator is Wendelstein 7-X [5, 6].
The devices that use the other approach are called tokamak and subject of this thesis. Tokamaks preserve the toroidal symmetry and create the poloidal field by a toroidal current in the plasma. To create the current the plasma is used as secondary winding of a transformer. The situation is sketched in Fig. 1.3. As the current in the primary winding can not be increased forever, a tokamak has to operate pulsed (contrary to a stellerator) unless other means of driving the current are found, which is an area of active research [7, 8, 9, 10, 11].
The first tokamaks have been constructed in Russia. In 1962 the T-3 tokamak at the Kurchtov Institute in Moscow achieved a record temperature. After these results were confirmed, tokamaks became the focus of the fusion program, but other reactor types still have been and are being studied. Twenty years later, in 1982, the "H-mode", with doubled confinement time, has been observed for the

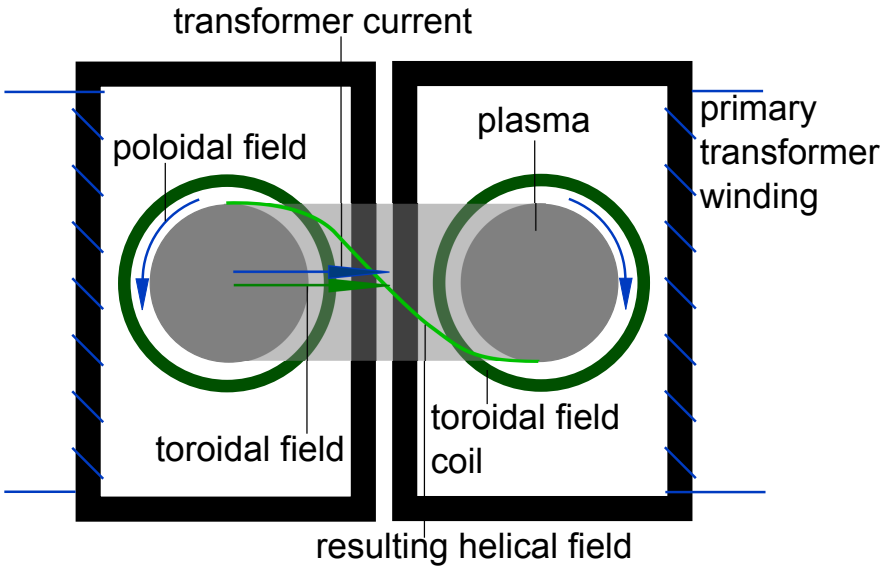

Figure 1.3: Sketch of the fields in a tokamak and how they are created. Not shown are poloidal field coils, which are used to shape the cross section of the plasma. Toroidal direction is along the major circle (long way) around the torus, while poloidal direction is along the small circle (short way around) of the torus.

first time in the ASDEX tokamak [12]. Until 2002 about 60 experiments have been constructed in different countries. Examples for tokamaks include Alcator C-Mod [13], ASDEX Upgrade [14], DIII-D [15], EAST [16], JET [17], JT-60U [18], MAST [19] and NSTX [20]. These stand in different regions of the world and explore different questions. See for example Fig. 2 of Ref. [1] for a size comparison, along with a comparison of the shape and main aspects over time. Also ITER [1], which should reach a ratio of energy output to auxiliary heating of $Q = 10$, and is a proof of a fusion power station concept, is a tokamak. Achievement of the first plasma is expected for 2020, and first deuterium-tritium fusion experiments for 2027. Plans for a demonstration power plant, called DEMO, are already in progress. Contrary to ITER, this will generate electricity.
Costs for these scientific experiments are quite high and require long planning ($\geq 10 - 20y$). Any predictive capability of the performance can be helpful in reducing costs. Therefore an active theoretical research program exists, to which this thesis contributes.
Transport (e.g. of heat, particles and momentum) determines plasma confinement. The main cause of transport is plasma turbulence, which is inherently non-linear, and therefore hard to describe. Even strongly reduced physical models can be solved analytically only in some special cases. Thus numerical simulations are the tool of choice, to make predictions of the performance and/or processes (e.g. transport) of a fusion reactor. Numerical simulations are also the method used in this thesis, aiming at a better understanding of the (transport) processes

in a tokamak and improving the quality of future simulations.
A main point to be studied with simulations are plasma instabilities. Particle orbits are confined, but the collective interaction of particles with the electromagnetic field can generate instabilities. It is differentiated between large and small scale instabilities. Large scale instabilities can lead to a loss of control and a disruption of the plasma. Small scale instabilities can drive transport of particles, energy and momentum and thus decrease the confinement time. The former group can be controlled, for example by careful reactor design and choosing of the operation parameters. The transport in tokamaks, of heat, momentum and particles, is dominated by the small scale turbulence.
There are different types of radial transport in a tokamak. Classical transport occurs due to the collisions of particles in a plasma cylinder, which causes diffusion. Neoclassical transport is caused by effects due to the particle drifts in the inhomogeneous magnetic field of the tokamak. However, as already indicated, the transport found in experiments is larger than what is expected from the (neo)classical theory and attributed to the small scale turbulence.
The simulations for this thesis are obtained with the gyrokinetic Vlasov-code GKW [21, 22]. The foundation for this type of code has been laid in 1968 [23]. As other codes, it can be used to perform linear or nonlinear simulation. GKW also has the capability to treat profile effects, as well as the effects of rotation [24, 25, 26].

1.3 Rotation

Due to the toroidal symmetry the toroidal angular momentum , in contrast to its poloidal counterpart, is a conserved quantity. Consequently, only radial transport processes can influence the development of the toroidal rotation. Experiments have shown a positive influence of toroidal rotation [27, 28, 29] on confinement. In the first tokamak experiments rotation was created externally, especially by the heating (e.g. neutral beam injection (NBI)). This external torque is expected to be small for large devices, but recent experiments have shown that a rotation can develop also without an external torque. This so called “intrinsic rotation” has led to renewed interest in the research on rotation. The physics behind the intrinsic rotation is not yet fully understood.
GKW is formulated in the co-moving frame and thus Coriolis and centrifugal terms appear. For the main ions the Mach numbers are usually small and the influence of the rotation on the plasma transport is limited. However, at a given plasma rotation the relative Mach numbers (rotation velocity divided by thermal velocity) increase with the mass of the ions, as the thermal velocity decreases. Thus centrifugal effects are especially important for heavier ions.

1.4 Outline

Chapter 2 presents the basic theory, needed for the understanding of the following chapters.
Chapter 3 discusses the eigenvalue solver. Most codes in use for the simulation of fusion plasmas, which includes GKW, use some kind of explicit time integration. This kind of approach has some drawbacks, most important that only the most unstable mode can be found. Natural solution to this problem is the use of an eigenvalue solver. As part of this thesis an eigenvalue solver has been implemented and tested.
Chapter 4 discusses the momentum transport due to profile effects. If follows up on, and extends, the results of Ref. [30], which studies the linear physics. In this thesis linear simulations are compared with non-linear simulations. Chapter 5 discusses the second mechanism of momentum transport treated in this thesis: the velocity nonlinearity.
In chapter 6 simulations are made for an experiment of NSTX [20], with a focus on the influence of centrifugal effects, previously neglected in the modelling of this experiment.
Finally the main results of this thesis will be summarized in chapter 7.

Chapter 2

Theory

In this chapter the equations solved in GKW are derived and summarized. See also the documentation of GKW, chapters 1, 2 and 7 of [31], as well as Ref. [32]. Plasma instabilities occur through collective effects of charged particles, but there are too many particles in a plasma to describe them individually. Thus a continuous distribution function $F(\underline{x}, \underline{v}, t)$, that gives the particle density in phase space, is used. the Lagrange equation of a particle in an electromagnetic field is used to derive the time evolution of this distribution function.

2.1 Plasmas instabilities

The two most important instabilities within the framework of this thesis are the ion temperature gradient (ITG) mode and the kinetic ballooning mode (KBM).

2.1.1 Ion temperature gradient mode

The basic mechanism of the ITG mode is explained below. Assume a plasma with a background magnetic field, with a gradient of the magnetic field strength ∇B perpendicular to the field lines. Furthermore assume a gradient of temperature aligned with ∇B (see Fig. 2.1(a)). These conditions occur on the outboard side of a tokamak. It is then assumed that a temperature perturbation exists in the form of a wave with a wavevector perpendicular to ∇B (see Fig. 2.1). The drift of particles due to curvature/gradient of magnetic field strength, is proportional to the particle energy and thus the temperature. An averaged modulated vertical velocity results that leads to a compression, and a density perturbation, which has a phase shift of $\pi/2$, relative to the temperature perturbation. The density perturbation of ions in turn leads to a potential perturbation. The plasma is assumed to be quasineutral, and assuming adiabatic electrons one obtains a potential per-

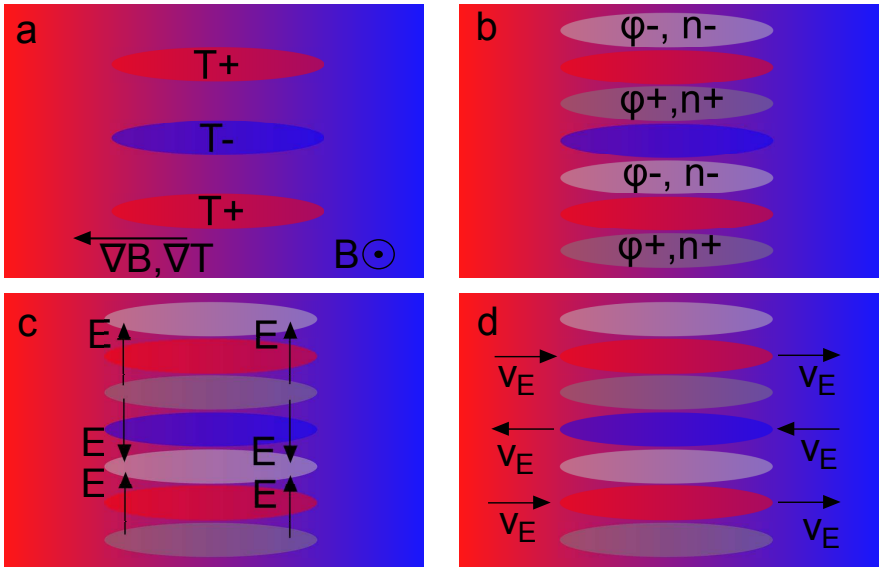

Figure 2.1: Sketch explaining the mechanism behind the ITG mode.

turbation that is in phase with the ion density perturbation (Fig. 2.1(b)). The resulting $E \times B$ drift will enhance the perturbation by moving cold plasma into the cold regions and hot plasma into the hot regions (Fig. 2.1(c+d)), thus leading to an instability.
The situation described here occurs on the outside of the torus. On the inside the perturbation would be damped, as the direction of the temperature gradient is reversed. Therefore the stability of a mode in a tokamak involves a nontrivial average over a flux surface. The unstable mode is expected to be (more or less) localized on the outboard side.

2.1.2 Ballooning modes

Ballooning modes (BM) are a class of modes that are driven by the pressure gradient, and that can be described by the fluid theory magneto hydro-dynamics. There is, however, also a kinetic variant of this mode, the kinetic (Alfven) ballooning mode (KBM). The name ballooning mode refers to the tendency of the mode to be localized on the outboard side of the torus (the same holds for the ITG mode). Because of further similarities (both propagate in the ion diamagnetic direction (positive frequency in GKW), for both the perturbed potential is symmetric with respect to the low field side position, while the perturbed parallel magnetic potential is antisymmetric and out of phase). The dependence on the normalized pressure

$$\beta = \frac{nT}{B^2/(2\mu_0)}, \tag{2.1}$$

however, is different for ITG and KBM. While the ITG is stabilised with increasing β, the growth rate (γ) of the KBM increases with β. Therefore, the dependence of γ on β can be used to identify the mode.

2.2 Ordering

There is a huge span of length and time scales covered inside of a fusion plasma. The length scales range from the size of the tokamak ($\sim$ 1m) down to the electron Larmor-radius ($\sim 10\mu$m). The time scales involved range from the inverse electron gyrofrequency $\sim 10^{-11}$s, over the inverse frequency of instabilities $\sim 10^{-5}$s, to the operation time of the reactor (so far $\sim 10^{1}$s).
This makes direct computations not feasible. Reduced model equations can be obtained by making ordering assumptions. These are used to remove time and space scales that are of less interest. Within the scope of the model that will be used in this thesis, this includes for example the fast gyromotion which is removed by an averaging procedure.
Usual ordering assumptions in gyrokinetic theory [33, 34, 32] are

$$\frac{\omega}{\Omega} \sim \epsilon_\omega \ll 1 \tag{2.2}$$

$$\frac{|\underline{A}_1|}{|\underline{A}_0|} \sim \frac{\Psi_1}{\Psi_0} \sim \epsilon_\delta \ll 1 \tag{2.3}$$

$$\rho\frac{\nabla B_0}{B_0} \sim \rho\frac{\nabla E_0}{E_0} \sim \frac{\rho}{L_B} \sim \epsilon_B \ll 1 \tag{2.4}$$

$$k_\perp\rho \sim \epsilon_\perp \sim 1 \tag{2.5}$$

$$\frac{k_\parallel}{k_\perp} \sim \frac{\epsilon_\omega}{\epsilon_\perp} \ll 1 \tag{2.6}$$

where $\underline{A}$ and Ψ are the vector and scalar potential, $\underline{B}$ and $\underline{E}$ denote the magnetic and electric field, ω and $k_\perp$ are the typical mode frequency and perpendicular wave number while ρ (ρ_*) is the (normalized) Larmor-radius and Ω is the Larmor-frequency.
The first relation means that the frequency of phenomena of interest (ω), is small compared to the cyclotron frequency Ω. The second relation expresses that fluctuations (subscript 1) are assumed small compared to the background (subscript 0). This ordering relation can also be used to split the distribution function F into a background part (F_M) and a perturbation (f)

$$F = F_M + f \tag{2.7}$$

with

$$f \propto \epsilon_\delta F_M. \tag{2.8}$$

and the background (F_M) is assumed to be a Maxwellian. Relation number three states that the logarithmic gradient length scale of the background fields L_B are of the order of the major radius R. The last relation formalizes the assumption that parallel length scales are of the order of the major radius, while perpendicular length scales are of the order of the gyroradius.
Different theories are possible by ordering the three different scaling parameters ϵ_δ, ϵ_B and ϵ_ω. It is usual practice to assume that they are of similar magnitude and, therefore, can be replaced by a single quantity. This approach is also used in this thesis. The single quantity used is the normalised Larmor-radius ρ_*, the thermal ion Larmor-radius ρ_i normalised with the major radius R of the tokamak

$$\rho_* \quad = \quad \frac{\rho_i}{R} = \epsilon_\delta = \epsilon_B = \epsilon_\omega. \tag{2.9}$$

The ordering discussed above leads to an ordering of length scales [34]

$$\nabla_\parallel f \quad \sim \quad \rho_* \nabla_\perp f \tag{2.10}$$

$$L_{\perp,F} \sim \rho_* L_{\perp,f} \quad \Rightarrow \quad \nabla_\perp f \sim \nabla_\perp F \tag{2.11}$$

$$L_{\parallel,F} \sim L_{\parallel,f} \quad \Rightarrow \quad \nabla_\parallel f \sim \rho_* \nabla_\parallel F, \tag{2.12}$$

where $\nabla_\parallel$ and $\nabla_\perp$ depict the component of the gradient parallel and perpendicular to the magnetic (background) field, respectively.
As a last point it is assumed that the time variation of the background quantities $Q = \{B, T, n, \omega_\phi\}$ are small [33]

$$\left| \frac{1}{\omega_{ci}} \frac{\partial \ln Q}{\partial t} \right| \sim \rho_*^3. \tag{2.13}$$

In GKW this is used in the global case (see below) to neglect the change in background quantities completely, they are assumed as constant. In a flux tube (local, see below) simulation they are constant by construction.

2.3 Gyrokinetic Theory

Here we will follow "Derivation of the fully electro-magnetic, non linear, gyrokinetic Vlasov-Maxwell equations in a rotating frame of reference for GKW with Lie transform perturbation method" by Gabor Szepesi [32] and Ref. [34].
We are interested in phenomena on timescales that are longer than the Larmor frequency (see Eq. (2.2)), thus it is advisable to reduce the dimension of the phase space by averaging over the gyromotion of the particles. This is done in the following subsection and leads to the gyrokinetic theory.

2.3.1 Derivation

To derive the equations used in GKW, we start with the Lagrangian of a charged particle in an electro-magnetic field

$$\gamma \;=\; \gamma_\nu dz^\nu = \underbrace{(m\underline{v} + Ze\underline{A}(x))}_{\text{sympletic part}} \cdot d\underline{x} - \underbrace{\left(\frac{1}{2}mv^2 + Ze\phi(\underline{x})\right)}_{\text{Hamiltonian part}} dt. \tag{2.14}$$

This is transformed to a rotating frame (see Ref. [31] and [25]). Assuming

$$\underline{u}_0 \;=\; \underline{\Omega} \times \underline{X}, \tag{2.15}$$

i.e. a rigid body rotation with rotation frequency Ω, one obtains

$$\gamma \;=\; (m(\underline{v} + \underline{u}_0) + Ze\underline{A}(x)) \cdot d\underline{x} - \left(\frac{1}{2}mv^2 - \frac{1}{2}mu_0^2 + Ze(\phi(\underline{x}))\right) dt. \tag{2.16}$$

From this the gyrokinetic Lagrangian can be obtained [35]

$$\begin{aligned}\Gamma \;=\;& (m(v_\parallel \hat{\underline{b}} + \underline{u}_0) + Ze\underline{A}(x)) \cdot d\underline{X} + \mu d\theta \\ & - \underbrace{(\frac{1}{2}mv_\parallel^2 - \frac{1}{2}mu_0^2 + Ze\langle\phi(\underline{x})\rangle + Ze\langle\Phi(\underline{x})\rangle + \mu B)}_{\text{Hamiltionian H}}\, dt.\end{aligned} \tag{2.17}$$

The gyroangle is depicted by θ, while the average over the gyroangle is depicted by $\langle \ldots \rangle$. The magnetic moment is

$$\mu \;=\; \frac{mv_\perp^2}{2B}. \tag{2.18}$$

In the following, the definition

$$\underline{B}^* \;=\; \underline{B} + \frac{m}{Ze}\nabla \times (v_\parallel \hat{\underline{b}} + \underline{u}_0), \tag{2.19}$$

is useful to obtain the equations in compact form. The equations of motion follow from the Poisson brackets [35, 25]

$$\begin{aligned}\{F, G\} \;=\;& \frac{Ze}{m}\left(\frac{\partial F}{\partial \theta}\frac{\partial G}{\partial \mu} - \frac{\partial F}{\partial \mu}\frac{\partial G}{\partial \theta}\right) - \frac{\hat{\underline{b}}}{eB_\parallel^*} \cdot \nabla F \times \nabla G \\ & + \frac{\underline{B}^*}{mB_\parallel^*} \cdot \left(\nabla F \frac{\partial G}{\partial v_\parallel} - \frac{\partial F}{\partial v_\parallel}\nabla G\right)\end{aligned} \tag{2.20}$$

using the generalised Hamilton equation for a function h

$$\frac{\mathrm{d}h}{\mathrm{d}t} \;=\; \{h, H\} + \frac{\partial h}{\partial t}. \tag{2.21}$$

This is used for the coordinates $(\underline{X}, v_\parallel, \mu, \theta)$ ($\partial h/\partial t = 0$ in these cases)

$$\frac{\mathrm{d}\underline{X}}{\mathrm{d}t} = \{\underline{X}, H\} = \frac{\hat{\underline{b}}}{ZeB^*_\parallel} \times \nabla H + \frac{\underline{B}^*}{mB^*_\parallel}\frac{\partial H}{\partial v_\parallel} \tag{2.22}$$

$$\frac{\mathrm{d}v_\parallel}{\mathrm{d}t} = \{v_\parallel, H\} = -\frac{\underline{B}^*}{mB^*_\parallel} \cdot \nabla H = -\frac{1}{mv_\parallel}\frac{\mathrm{d}\underline{X}}{\mathrm{d}t} \cdot \nabla H \tag{2.23}$$

$$\frac{\mathrm{d}\mu}{\mathrm{d}t} = \{\mu, H\} = 0 \tag{2.24}$$

$$\frac{\mathrm{d}\theta}{\mathrm{d}t} = \{\theta, H\} \tag{2.25}$$

Before the Hamiltonian is inserted into Eq. (2.22), some helpful relations are considered. First, note that the perpendicular part of a vector $\underline{p}$ can be given as

$$\underline{p}_\perp = \underline{p} - (\underline{p} \cdot \hat{\underline{b}})\hat{\underline{b}} \tag{2.26}$$

$$= -\hat{\underline{b}} \times (\hat{\underline{b}} \times \underline{p}) \tag{2.27}$$

where for the second line a vector identity (Eq. (E.2)) has been used. This can be used for

$$\underline{B}^* - B^*_\parallel \hat{\underline{b}} = -\hat{\underline{b}} \times (\hat{\underline{b}} \times \underline{B}^*) \tag{2.28}$$

$$= -\hat{\underline{b}} \times (\hat{\underline{b}} \times \frac{m}{Ze}\nabla \times (v_\parallel \hat{\underline{b}} + \underline{u}_0)), \tag{2.29}$$

which in turn helps with the ratio

$$\frac{\hat{\underline{B}}^*}{B^*_\parallel} = \hat{\underline{b}} - \frac{m}{ZeB^*_\parallel}\hat{\underline{b}} \times (\hat{\underline{b}} \times (\nabla \times (v_\parallel \hat{\underline{b}} + \hat{\underline{u}}_0))). \tag{2.30}$$

The rotation of the rotation velocity (Eq. (2.15)) is (using Eq. (E.8))

$$\nabla \times \underline{u}_0 = \nabla \times (\underline{\Omega} \times \underline{X}) \tag{2.31}$$

$$= 2\underline{\Omega}. \tag{2.32}$$

Inserting this into Eq. (2.30)

$$\frac{\hat{\underline{B}}^*}{B^*_\parallel} = \hat{\underline{b}} - \frac{m}{ZeB^*_\parallel}\hat{\underline{b}} \times (\hat{\underline{b}} \times (v_\parallel \nabla \times \hat{\underline{b}} + 2\underline{\Omega})). \tag{2.33}$$

With the identity (E.6)

$$\hat{\underline{b}} \times (\nabla \times \hat{\underline{b}}) = -(\hat{\underline{b}} \cdot \nabla)\hat{\underline{b}} \tag{2.34}$$

this simplifies to

$$\frac{\hat{\underline{B}}^*}{B^*_\parallel} = \hat{\underline{b}} + \frac{mv_\parallel}{ZeB^*_\parallel}\hat{\underline{b}} \times ((\hat{\underline{b}} \cdot \nabla)\hat{\underline{b}}) + \frac{2m}{ZeB^*_\parallel}\underline{\Omega}_\perp. \tag{2.35}$$

The derived relations are now inserted into the equation for the time derivative of $\underline{X}$

$$\begin{aligned}
\frac{\mathrm{d}\underline{X}}{\mathrm{d}t} &= \frac{\hat{\underline{b}}}{ZeB_{\parallel}^{*}} \times \nabla \left(\frac{1}{2} m v_{\parallel}^{2} - \frac{1}{2} m u_{0}^{2} + Ze\langle \phi(\underline{x}) \rangle + Ze\langle \Phi(\underline{x}) \rangle + \mu B \right) \\
&\quad + \frac{\underline{B}^{*}}{mB_{\parallel}^{*}} \frac{\partial}{\partial v_{\parallel}} \left(\frac{1}{2} m v_{\parallel}^{2} - \frac{1}{2} m u_{0}^{2} + Ze\langle \phi(\underline{x}) \rangle + Ze\langle \Phi(\underline{x}) \rangle + \mu B \right) \qquad (2.36) \\
&= v_{\parallel} \hat{\underline{b}} \\
&\quad + \frac{m v_{\parallel}^{2}}{ZeB_{\parallel}^{*}} \hat{\underline{b}} \times (\hat{\underline{b}} \cdot \nabla) \hat{\underline{b}} + \frac{\mu}{Ze} \frac{\hat{\underline{b}} \times \nabla B}{B_{\parallel}^{*}} + \frac{2 m v_{\parallel}}{ZeB_{\parallel}^{*}} \underline{\Omega}_{\perp} \\
&\quad - \frac{mR\Omega^{2}}{ZeB_{\parallel}^{*}} \hat{\underline{b}} \times (\nabla R) + \frac{\hat{\underline{b}} \times \nabla \langle \Phi(\underline{x}) \rangle}{B_{\parallel}^{*}} \\
&\quad + \frac{\hat{\underline{b}} \times \nabla \langle \phi(\underline{x}) \rangle}{B_{\parallel}^{*}} \qquad (2.37)
\end{aligned}$$

The first term on the right hand side is the free motion of the particle along the field line. The last term is the $\underline{E} \times \underline{B}$ drift. The other terms are grouped as background drifts, as they are independent of the perturbed quantities.
The time derivative of the parallel velocity is more straightforward

$$\frac{\mathrm{d}v_{\parallel}}{\mathrm{d}t} = -\frac{1}{m v_{\parallel}} \frac{\mathrm{d}\underline{X}}{\mathrm{d}t} \cdot \nabla H \qquad (2.38)$$

$$m v_{\parallel} \frac{\mathrm{d}v_{\parallel}}{\mathrm{d}t} = -\frac{\mathrm{d}\underline{X}}{\mathrm{d}t} \left(-mR\Omega^{2} \nabla R + Ze\nabla\langle \phi \rangle + Ze\nabla\langle \Phi \rangle + \mu \nabla B \right). \qquad (2.39)$$

Now consider the total time derivative of the distribution function $F(t, \underline{X}, v_{\parallel}, \mu)$, which leads to the gyrokinetic equation

$$0 = \frac{\mathrm{d}F}{\mathrm{d}t} = \frac{\partial F}{\partial t} + \frac{\mathrm{d}\underline{X}}{\mathrm{d}t} \frac{\partial F}{\partial \underline{X}} + \frac{\mathrm{d}v_{\parallel}}{\mathrm{d}t} \frac{\partial F}{\partial v_{\parallel}}. \qquad (2.40)$$

The total distribution function will be split into a background part (F_M) and a perturbation (f)

$$F = F_M + f, \qquad (2.41)$$

making use of the δf formulation and with the ordering assumption already given in Eq. (2.8). Expanding the gyrokinetic equation (2.40) in lowest order ($O(1)$) results in

$$0 = v_{\parallel} \hat{\underline{b}} \cdot \nabla F_M - \frac{1}{m} \hat{\underline{b}} \cdot (Ze\nabla\langle \Phi \rangle + \mu \nabla B - m\Omega^{2} R \nabla R) \frac{\partial F_M}{\partial v_{\parallel}}. \qquad (2.42)$$

The background is given as

$$F_M = \frac{n}{(2\pi T/m)^{3/2}} \exp\left[-\frac{m(v_\parallel - u_\parallel)^2}{2T} - \frac{\mu B}{T} + \frac{\mathcal{E}}{T}\right], \tag{2.43}$$

with $u_\parallel = RB_t/B(\omega_\phi^L(\psi) - \Omega)$ and

$$\mathcal{E} = Ze\Phi - \frac{1}{2}m\Omega^2(R^2 - R_0^2). \tag{2.44}$$

When evaluating derivatives of the Maxwellian, a constant gradient $u' = -(R_A/v_{th})\partial\omega_\phi^L/\partial\psi$ is kept.
Inserting the equations of motion (2.37) and (2.39) into the gyrokinetic equation (2.40) and collect the first order terms, to get the first order equation

$$\frac{\partial f}{\partial t} + (v_\parallel \hat{\underline{b}} + \underline{v}_D + \underline{v}_\chi)\cdot\nabla f - \frac{\hat{\underline{b}}}{m}\cdot(\mu\nabla B + \nabla\mathcal{E}_\Omega)\frac{\partial f}{\partial v_\parallel} = S, \tag{2.45}$$

with the background part

$$S = -(\underline{v}_D + \underline{v}_\chi)\cdot\nabla F_M - \frac{Ze}{T}\left[v_\parallel\hat{\underline{b}} + \underline{v}_D\right]\cdot\nabla\langle\phi\rangle F_M. \tag{2.46}$$

2.3.2 Normalization

The equations implemented in GKW are normalized. There are five reference quantities: for temperature (T_{ref}), density (n_{ref}), mass (m_{ref}), major radius (R_{ref}) and magnetic field (B_{ref}). The velocity grid is normalized with the thermal velocity of the corresponding species, so that the same grid can be used for all species. The temperature that is used for the thermal velocities is

$$T_{GN} = \frac{T_G}{T_{ref}}, \tag{2.47}$$

which is different for each species. The corresponding thermal velocity for a particle with mass m is

$$v_G = \sqrt{\frac{2T_G}{m}}. \tag{2.48}$$

With this the velocity space coordinates are

$$v_\parallel = v_G v_{\parallel N} \tag{2.49}$$

$$\mu = \frac{mv_G^2}{B_{ref}}\mu_N. \tag{2.50}$$

Similarly, the normalized density is given by

$$n_N = \frac{n}{n_{ref}} \tag{2.51}$$

$$n_{GN} = \frac{n_G}{n_{ref}} \tag{2.52}$$

where n_G is the species dependent reference. The normalization of the mass is

$$m_N = \frac{m}{m_{ref}}. \tag{2.53}$$

The reference values of temperature, mass and velocity are related through

$$T_{ref} = \frac{1}{2} m_{ref} v_{thref}^2, \tag{2.54}$$

and thus

$$v_{GN} = \frac{v_G}{v_{thref}} = \sqrt{\frac{T_{GN}}{m_N}}. \tag{2.55}$$

One should keep in mind, that species independent quantities are normalized with v_{thref}

$$t = \frac{R_{ref}}{v_{thref}} t_N \tag{2.56}$$

$$\Omega = \frac{v_{thref}}{R_{ref}} \Omega_N \tag{2.57}$$

$$\rho_* = \frac{\rho_{ref}}{R_{ref}} = \frac{1}{R_{ref}} \frac{m_{ref} v_{thref}}{e B_{ref}}, \tag{2.58}$$

v_G is only used for the velocity space coordinates.
The normalization of the distribution functions and fields is

$$F_M = \frac{n_G}{v_G^3} F_{MN} \tag{2.59}$$

$$f = \rho_* \frac{n_G}{v_G^3} f_N \tag{2.60}$$

$$\Phi = \frac{T_{ref}}{e} \Phi_N \tag{2.61}$$

$$\phi = \rho_* \frac{T_{ref}}{e} \phi_N \tag{2.62}$$

$$A_\parallel = B_{ref} R_{ref} \rho_*^2 A_{\parallel N} \tag{2.63}$$

$$B = B_{ref} B_N. \tag{2.64}$$

This means that all normalized quantities are of order 1. The radius is normalized with the reference radius

$$R = R_{ref} R_N. \tag{2.65}$$

To write the equation for the distribution function in compact form, the following tensors are introduced:

$$\mathcal{F}_N = \frac{B_N^s}{B_N} = \frac{B^s/B_{ref}}{B/B_{ref}} = \frac{B^s}{B} \tag{2.66}$$

$$\mathcal{E}_N^{\alpha\beta} = \frac{1}{2B_N}(\nabla_N x_N^\alpha \times \nabla_N x_N^\beta) \cdot \underline{\hat{b}} \tag{2.67}$$

$$\mathcal{D}_N^\alpha = -2\mathcal{E}_N^{\alpha\beta}\frac{1}{B_N}\frac{\partial B_N}{\partial x_N^\beta} \tag{2.68}$$

$$\mathcal{G}_N = \mathcal{F}_N\frac{\partial \ln B_N}{\partial s_N} \tag{2.69}$$

$$\mathcal{H}_N^\alpha = -\frac{s_B}{B_N\Omega_N}\underline{\Omega}_{\perp N} \cdot \nabla_N x_N^\alpha \tag{2.70}$$

$$\mathcal{I}_N^\alpha = \frac{s_B}{2B_N}(\nabla_N x_N^\alpha \times \nabla_N R_N^2) \cdot \underline{\hat{b}} \tag{2.71}$$

$$\mathcal{J}_N = R_N^2 - R_{0N}^2 \tag{2.72}$$

$$\mathcal{K}_N = \left.\frac{\partial \mathcal{J}_N}{\partial \psi_N}\right|_{s_N} \tag{2.73}$$

$$\mathcal{L}_N = \left.\frac{\partial R_{0N}^2}{\partial \psi_N}\right|_{s_N} \tag{2.74}$$

$$\mathcal{M}_N = \frac{s_j}{4\pi}\frac{\partial}{\partial \psi_N}\left(\frac{1}{\mathcal{E}_N^{\psi\zeta}}\right). \tag{2.75}$$

$\mathcal{D}_N$ is related to the grad B drift, $\mathcal{F}_N$ to parallel derivatives, $\mathcal{G}_N$ to trapping, $\mathcal{H}_N$ to Coriolis drift, $\mathcal{I}_N$ to centrifugal drift, and $\mathcal{J}_N$, $\mathcal{K}_N$ and $\mathcal{L}_N$ to the calculation of the centrifugal potential.
Applying the normalizations to the first order equation (2.45), results in the equations used by GKW and given in the next section.

2.4 Complete Equations

Here the complete set of (normalized) equations for the distribution function for local magnetic simulations in the spectral case in GKW is given [31]. The structure is

$$\frac{\partial g}{\partial t} = \mathrm{I} + \mathrm{II} + \mathrm{III} + \mathrm{IV} + \mathrm{V} + \mathrm{VI} + \mathrm{VII} + \mathrm{VIII} + \mathrm{X} + \mathrm{XI}, \tag{2.76}$$

with the terms

$$\begin{aligned}
\mathrm{I} &= -v_\parallel \mathbf{b}\cdot\nabla f \to -v_R v_\parallel \mathcal{F}\frac{\partial \hat{f}}{\partial s},\\
\mathrm{II} &= -\mathbf{v}_D\cdot\nabla f \to \\
&\quad -\frac{\mathrm{i}}{Z}\left[T_R E_D \mathcal{D}^\alpha + T_R v_\parallel^2 \beta' \mathcal{E}^{\psi\alpha} + 2m_R v_R v_\parallel \Omega \mathcal{H}^\alpha + m_R\Omega^2 I^\alpha + Z\mathcal{E}^{\beta\alpha}\frac{\partial\Phi}{\partial x_\beta}\right] k_\alpha \hat{f} +\\
&\quad -\frac{\rho_*}{Z}\left[T_R E_D \mathcal{D}^s + T_R v_\parallel^2 \beta' \mathcal{E}^{\psi s} + 2m_R v_R v_\parallel \Omega \mathcal{H}^s + m_R\Omega^2 I^s + Z\mathcal{E}^{\beta s}\frac{\partial\Phi}{\partial x_\beta}\right]\frac{\partial \hat{f}}{\partial s}, \qquad (2.77)\\
\mathrm{III} &= -\mathbf{v}_\chi\cdot\nabla g \rightharpoonup -\rho_*^2\frac{\partial\chi}{\partial x_\beta}\mathcal{E}^{\beta\alpha}\frac{\partial g}{\partial x_\alpha} = \rho_*^2\mathcal{E}^{\psi\zeta}\left(\frac{\partial\chi}{\partial\zeta}\frac{\partial g}{\partial\psi} - \frac{\partial g}{\partial\zeta}\frac{\partial\chi}{\partial\psi}\right)\\
&\qquad \rightharpoonup \mathcal{T}\Big(\mathcal{E}^{\psi\zeta}\left[\mathcal{T}^{-1}(ik_\zeta\hat{\chi})\mathcal{T}^{-1}(ik_\psi\hat{g}) - \mathcal{T}^{-1}(ik_\zeta\hat{g})\mathcal{T}^{-1}(ik_\psi\hat{\chi})\right]\Big), \qquad (2.78)\\
\mathrm{IV} &= +\frac{\mathbf{b}}{m}\cdot(\mu\nabla B + \nabla\mathcal{E}_\Omega)\frac{\partial f}{\partial v_\parallel} \to v_R\left(\mu B\mathcal{G} + \frac{1}{2}\frac{\partial\mathcal{E}_R}{\partial s}\mathcal{F}\right)\frac{\partial\hat{f}}{\partial v_\parallel}, \qquad (2.79)\\
\mathrm{V} &= -\mathbf{v}_\chi\cdot\nabla F_M \to \mathrm{i}k_\alpha\hat{\chi}\mathcal{E}^{\alpha\psi}\left[\frac{1}{L_n} + \frac{m_R\Omega^2}{T_R}\mathcal{L} + E_T\frac{1}{L_T} + \frac{2v_\parallel}{v_R}\frac{RB_t}{B}u'\right]F_M\\
&\qquad +\rho_*\frac{\partial\hat{\chi}}{\partial s}\mathcal{E}^{s\psi}\left[\frac{1}{L_n} + \frac{m_R\Omega^2}{T_R}\mathcal{L} + E_T\frac{1}{L_T} + \frac{2v_\parallel}{v_R}\frac{RB_t}{B}u'\right]F_M, \qquad (2.80)\\
\mathrm{VI} &= -\mathbf{v}_D\cdot\nabla F_M \to \frac{1}{Z}\left[T_R E_D\mathcal{D}^\psi + 2m_R v_R v_\parallel\Omega\mathcal{H}^\psi + m_R\Omega^2 I^\psi + Z\mathcal{E}^{s\psi}\frac{\partial\Phi}{\partial s}\right]\\
&\qquad \times\left[\frac{1}{L_n} + \frac{m_R\Omega^2}{T_R}\mathcal{L} + E_T\frac{1}{L_T} + \frac{2v_\parallel}{v_R}\frac{RB_t}{B}u'\right]F_M, \qquad (2.81)\\
\mathrm{VII} &= -\frac{Ze}{T}v_\parallel\mathbf{b}\cdot\nabla\langle\phi\rangle F_M \to -\frac{Z}{T_R}v_R v_\parallel\mathcal{F}\frac{\partial\widehat{\langle\phi\rangle}}{\partial s}F_M, \qquad (2.82)\\
\mathrm{VIII} &= -\frac{Ze}{T}\mathbf{v}_D\cdot\nabla\langle\phi\rangle F_M \to \\
&\quad -\mathrm{i}\left[E_D\mathcal{D}^\alpha + \beta' v_\parallel^2\mathcal{E}^{\psi\alpha} + \frac{2m_R v_R}{T_R}v_\parallel\Omega\mathcal{H}^\alpha + \frac{m_R\Omega^2}{T_R}\mathcal{I}^\alpha + \frac{Z}{T_R}\mathcal{E}^{\beta\alpha}\frac{\partial\Phi}{\partial x_\beta}\right]k_\alpha\,\widehat{\langle\phi\rangle}\,F_M\\
&\quad -\rho_*\left[E_D\mathcal{D}^s + \beta' v_\parallel^2\mathcal{E}^{\psi s} + \frac{2m_R v_R}{T_R}v_\parallel\Omega\mathcal{H}^s + \frac{m_R\Omega^2}{T_R}\mathcal{I}^s + \frac{Z}{T_R}\mathcal{E}^{\beta s}\frac{\partial\Phi}{\partial x_\beta}\right]\frac{\partial\widehat{\langle\phi\rangle}}{\partial s}F_M
\end{aligned}$$

(2.83)

$$\mathrm{X} = -\frac{F_M}{T} v_\parallel \mathbf{b}\cdot\left(\mu\nabla\langle B_{1\parallel}\rangle\right) \rightarrow -2v_R v_\parallel \mu F_M \mathcal{F}\frac{\partial\widehat{\langle B_{1\parallel}\rangle}}{\partial s} \tag{2.84}$$

$$\begin{aligned}\mathrm{XI} &= -\frac{F_M}{T}\mathbf{v}_D\cdot\left(\mu\nabla\langle B_{1\parallel}\rangle\right) \rightarrow -\frac{i}{Z}F_M 2T_R\mu\left(E_D\mathcal{D}^\beta + v_\parallel^2\beta'\mathcal{E}^{\psi\beta}\right)k_\beta\widehat{\langle B_{1\parallel}\rangle} \\ &\quad -\rho_*\frac{1}{Z}F_M 2T_R\mu\left(E_D\mathcal{D}^s + v_\parallel^2\beta'\mathcal{E}^{\psi s}\right)k_\beta\widehat{\langle B_{1\parallel}\rangle}\end{aligned} \tag{2.85}$$

where the arrows represent the transformations to normalized ($\rightharpoonup$) and Fourier ($\rightharpoondown$) quantities and where

$$\hat{\chi} = \widehat{\langle\phi\rangle} + \frac{2\mu T_R}{Z}\widehat{\langle B_{1\parallel}\rangle} - 2v_R v_\parallel\widehat{\langle A_\parallel\rangle}, \tag{2.86}$$

and

$$\hat{g} = \hat{f} + \frac{2Z}{T_\mathrm{R}} v_\mathrm{R} v_\parallel\widehat{\langle A_\parallel\rangle}F_M, \tag{2.87}$$

$$E_D = v_\parallel^2 + \mu B, \tag{2.88}$$

$$E_T = v_\parallel^2 + 2\mu B + \mathcal{E}_R - \frac{3}{2}. \tag{2.89}$$

To compute the perturbed potential (ϕ) the Poisson equation

$$\begin{aligned}0 &= \sum_{sp} Z_{sp} n_{R_{0,sp}}\left(2\pi B\int \mathrm{d}v_\parallel \mathrm{d}\mu J_0(k_\perp\rho_{sp})\hat{g}_{sp}\right. \\ &\quad \left. + \frac{Z_{sp}}{T_{sp}}[\Gamma(b_{sp})-1]\exp(-\mathcal{E}_{Rsp}\hat{\phi})\right)\end{aligned} \tag{2.90}$$

is used, while the parallel

$$\begin{aligned}&\left(k_\perp^2 + \beta\sum_{sp}\frac{Z_{sp}^2 n_{R_{0,sp}}}{m_{Rsp}}\exp(\mathcal{E}_{Rsp})\Gamma(b_{sp})\right)\hat{A}_\parallel \\ &= \beta\sum_{sp} Z_{sp} v_{Rsp} n_{R_{0,sp}} \times 2\pi B\int dv_\parallel\int d\mu v_\parallel J_0\hat{g}_{sp}\end{aligned} \tag{2.91}$$

and perpendicular

$$\begin{aligned}&\left(1 + \sum_{sp}\frac{T_{Rsp} n_{R_{0,sp}}}{B^2}\beta_{ref}\exp(-\mathcal{E}_{sp})(\Gamma_0(b_{sp}) - \Gamma_1(b_{sp}))\right)\hat{B}_{1\parallel} \\ &= -\sum_{sp}\beta_{ref}\left(2\pi B T_{Rsp} n_{R_{0,sp}}\int \mu\hat{J}_1(k_\perp\rho_{sp})\hat{g}_{sp}\mathrm{d}v_\parallel\mathrm{d}\mu\right. \\ &\quad \left. + \exp(-\mathcal{E}_{sp})(\Gamma_0(b_{sp}) - \Gamma_1(b_{sp}))\frac{Z_{sp} n_{R_{0,sp}}}{2B}\hat{\phi}\right)\end{aligned} \tag{2.92}$$

components of Ampere's law are used to compute $A_\parallel$ and $B_{1\parallel}$, respectively.

2.5 Geometry

Because of the large difference in length scale parallel and perpendicular to the field a coordinate system adapted to the problem must be chosen. This coordinate system follows the magnetic field lines, instead of torus-coordinates (i.e. toroidal angle, poloidal angle and minor radius, with major radius as parameter). GKW uses the straight field line Hamada coordinates, (ψ, ζ, s), with ψ the radial direction, ζ the binormal direction and s the parallel direction. The magnetic field in these coordinates has by construction three basic properties. Straightness means $B^\alpha = B^\alpha(\psi)$ $(\alpha \in (\psi, \zeta, s))$. The field alignment is expressed by $B^\zeta = B^\psi = 0$. Finally, ζ is still a symmetry coordinate, i.e. all quantities that are not a function of the toroidal angle, are independent of ζ. From these relations follows

$$\underline{B} \cdot \nabla f = B^s \frac{\partial f}{\partial s} \tag{2.93}$$

In the description of the plasma geometry it is possible to make a trade-off between accuracy and complexity. One can use a rather crude approximation, use real geometry data from an experiment, or something in between. The so called $s - \alpha$ geometry [36, 37] would be in the first category. Within this thesis two of the later geometries have been used, circular [37] and Miller geometry [38], which are described briefly in the next two subsections.

2.5.1 Circular geometry

Circular geometry [37] assumes that the flux surfaces are concentric circles, but in contrast to $s-\alpha$ geometry, keeps all orders in the inverse aspect ratio. Starting from a toroidal coordinate system (ψ, θ, ϕ), which represent the (minor) radius, poloidal angle and toroidal angle, respectively, a coordinate transformation to straight field line Hamada coordinates results in

$$s = \frac{1}{2\pi}(\theta + \epsilon \sin\theta), \tag{2.94}$$

and

$$\zeta = -\frac{\phi}{2\pi} + s_B s_j \frac{|q|}{\pi} \arctan\left[\sqrt{\frac{1-\epsilon}{1+\epsilon}} \tan\frac{\theta}{2}\right]. \tag{2.95}$$

The radial coordinate is the minor radius normalized to the major radius.

2.5.2 Miller geometry

Miller geometry [38] is more complicated compared with circular geometry, but also more realistic. It is a local solution of the Grad-Shafranov equation. The

cross section of the flux surface at constant toroidal angle ϕ is described by the equations

$$R = R_{mil} + r\cos(\theta + \arcsin\delta\sin\theta) \quad (2.96)$$
$$Z = Z_{mil} + r\kappa\sin(\theta + \gamma\sin 2\theta). \quad (2.97)$$

As for circular geometry, θ is the poloidal angle and there are parameters for the major radius, R_{mil}, the minor radius, r, and the elevation, Z_{mil}, of the flux surface. Additionally the parameters δ, κ and γ depict triangularity, elongation and squareness, respectively. An elongation parameter $\kappa \neq 1$ makes the cross

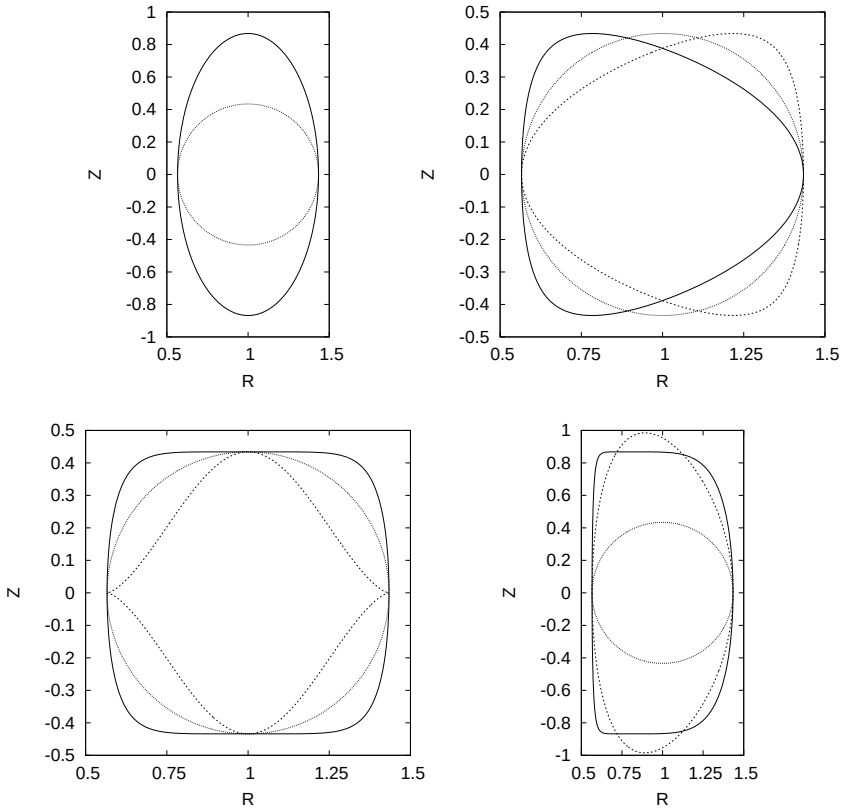

Figure 2.2: Examples for the effects of κ, δ and γ in Miller geometry. The dashed line is in all these plots a circular flux surface as reference. Top left: $\kappa = 2.0$, $\delta = \gamma = 0.0$. Top right: The full/dashed line has $\delta = \pm 0.5$, $\kappa = 1.0$ and $\gamma = 0.0$. Bottom left: The full/dashed line has $\gamma = \pm 0.5$, $\kappa = 1$ $\delta = 0.0$. Bottom right: The full line has $\kappa = 2$, $\delta = 0.5$ and $\gamma = 0.5$. The dashed line is an actual example for a flux surface from an experiment with $\kappa = 2.25$, $\delta = 0.25$, $\gamma = -0.016$.

section elliptical. δ defines the triangularity of the flux surface. For values greater than zero the triangle will point to the outside of the torus. Examples how these

parameters affect the geometry of the flux surfaces are shown in Fig. 2.2, including an example for a geometry of NSTX (except for the minor radius), which has been used in chapter 6. The geometry parameters can be found in Tab. 6.1 (shot #129061).
As the most general solution also includes the radial derivatives of the parameters, these enter the model. While the local model Eq. (2.96)+(2.97) is up-down symmetric, a finite $dZ_{mill}/d\psi$ will break this symmetry. This is easy to see, as a finite $dZ_{mil}/d\psi$ means that the flux surfaces are no longer concentric in vertical direction. All the other parameters and their derivatives do not break up-down symmetry.

2.6 Transport of Impurities and Momentum

While a basic understanding of heat and particle transport for the electrons and main ion species is emerging, there are still many open questions regarding particle transport of impurities and momentum transport. These are thus areas of active research and this thesis contributes to the efforts in these areas.
Transport of toroidal momentum is of interest since a finite toroidal rotation has been found to be benificial for confinement [27, 39, 40]. Radial transport of toroidal momentum is linked to plasma rotation and therefore of interest.
Early experiments found a strong correlation between heat and momentum transport. These experiments used neutral beam injection (NBI) to heat the plasma. The beams exert a torque on the plasma and, therefore, a relatively large plasma rotation is observed. For a long time it was implicitly assumed that the plasma rotation is directly related to the torque, until experiments with no or only a small torque lead to the discovery of the so called intrinsic rotation [41, 42, 43], i.e. the development of a plasma rotation without external torque. This observation led to an increased interest in momentum transport. Especially because ITER is expected to have only a small torque due to the heating system, the intrinsic rotation is of interest.
In GKW the radial flux of particles/heat/toroidal momentum are computed as [31, chapter 10.1]

$$R_{\mathrm{ref}}\Gamma_s^{\psi} = n_{R_0,s}\rho_*^2 v_{\mathrm{thref}}(\mathcal{I}_1 + \mathcal{J}_1 + \mathcal{K}_1) \quad (2.98)$$

$$R_{\mathrm{ref}}Q_s^{\psi} = n_{R_0,s}T_s\rho_*^2 v_{\mathrm{thref}}(\mathcal{I}_2 + \mathcal{J}_2 + \mathcal{K}_2) \quad (2.99)$$

$$R_{\mathrm{ref}}\Pi_{\phi s}^{\psi} = m_s n_{R_0,s} v_{ths} R_{\mathrm{ref}}\rho_*^2 v_{\mathrm{thref}}(\mathcal{I}_3 + \mathcal{J}_3 + \mathcal{K}_3) \quad (2.100)$$

using

$$\mathcal{I}_i = \sum_m \left\{ 2\pi B \mathcal{E}^{\psi\beta} k_{\beta m} \int \mathrm{d}\mu \mathrm{d}v_\parallel \, \hat{\alpha}_i \mathrm{Im}[\langle \hat{\phi}_m \rangle^\dagger \hat{f}_m] \right\} \tag{2.101}$$

$$\mathcal{J}_i = -2 \sum_m \left\{ 2\pi B \mathcal{E}^{\psi\beta} k_{\beta m} \int \mathrm{d}\mu \mathrm{d}v_\parallel \, \hat{\alpha}_i v_R v_\parallel \mathrm{Im}[\langle \hat{A}_{\parallel m} \rangle^\dagger \hat{f}_m] \right\} \tag{2.102}$$

$$\mathcal{K}_i = 2 \sum_m \left\{ 2\pi B \mathcal{E}^{\psi\beta} k_{\beta m} \int \mathrm{d}\mu \mathrm{d}v_\parallel \, \hat{\alpha}_i \frac{\mu T_R}{Z_{sp}} \mathrm{Im}[\langle \hat{B}_{\parallel m} \rangle^\dagger \hat{f}_m] \right\}. \tag{2.103}$$

with $\hat{\alpha}_i = (1, v^2, \frac{s_\mathrm{B} R B_t}{B} v_\parallel)$, for particle, heat and momentum flux, respectively. Also the notation $\sum_m \{\} = \sum_{k_\zeta} \sum_{k_\psi} \int_s$ has been used.
It is common practice to normalize the momentum and particle transport with the heat transport, which reduces the problem of normalisation of the fluxes for comparison. For linear simulation this is even more appropriate, because the absolute values of the fluxes are in this case meaningless, since no saturation occurs.
Momentum transport is closely related to a symmetry breaking in the underlying model equations. It can be shown [44, 45, 46] that for an up-down symmetric equilibrium without plasma rotation the transformation

$$\begin{aligned} &v_\parallel \to -v_\parallel, \; s \to -s, \; \psi \to -\psi \\ &f \to -f, \; \phi \to -\phi, \; A_\parallel \to A_\parallel, \; B_{1\parallel} \to -B_{1\parallel} \end{aligned} \tag{2.104}$$

leaves the local model equations unchanged while reverting the sign of the momentum flux. From this it follows, that under these conditions the momentum flux will be zero, as two modes with equal growth rate but different sign of the momentum flux are equally unstable. The transformation of the system is an expression of a (complicated) symmetry of the system, and a breaking of these symmetry is a necessary condition for a flux of toroidal momentum. This means that each source of momentum transport can be attributed to a symmetry breaking. Relevant mechanisms for symmetry breaking within the scope of this thesis are rotation, the velocity nonlinearity, up-down symmetry breaking through a shift in the vertical position of flux surfaces with radius (specifically a finite dZ_{mill} in the Miller geometry), and radial inhomogeneity in the background distribution or geometry.
To estimate the momentum flux that is to be expected at certain (experimental) parameters, transport models are derived. For the momentum transport these are usually linear and depend on quantities that are related to the rotation velocity and its gradient. The already mentioned discovery of intrinsic rotation has shown that this is not enough to explain the experimental observations.

2.7 Local vs. Global Simulations

The model derived above describes a flux tube (see Fig. 2.3), and can be used in local simulations. This is in contrast to so called global simulations. Global here refers to profile effects, i.e. the effect of a radial variation in plasma parameters and geometry is kept. The model, however, does not retain all finite ρ_* effects. If the normalized Larmor-radius is sufficient small the radial variation of plasma parameters and geometry can be neglected and the local model applies. In this case the computational domain can be chosen to be a flux tube, as sketched in Fig. 2.3. Turbulence is then homogeneous in the plane perpendicular to the mag-

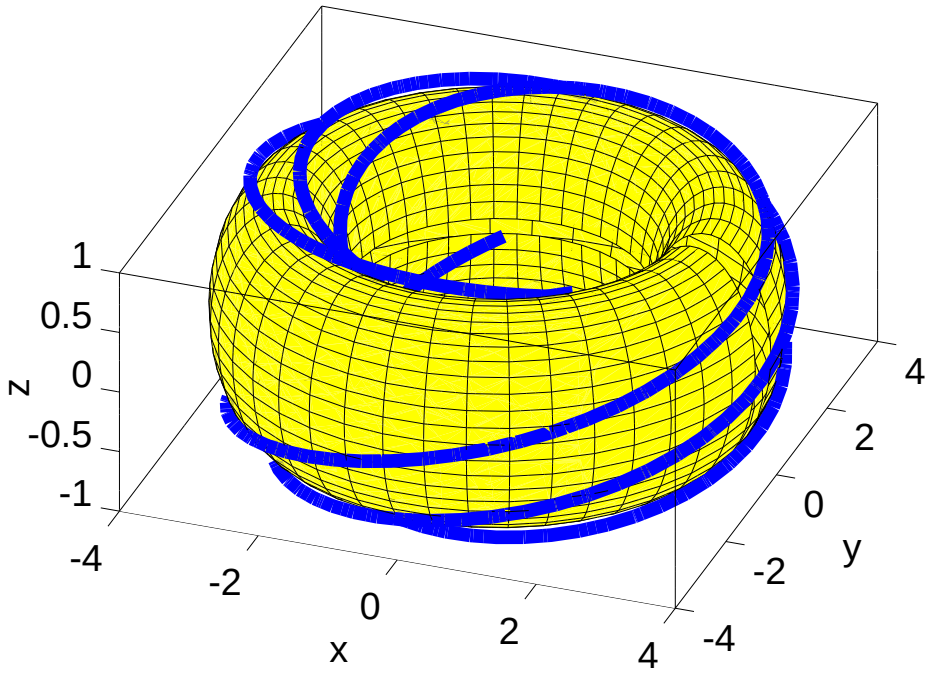

Figure 2.3: A sketch of a "flux tube" (blue line), winding around a torus with circular cross section. The flux tube is shown for multiple rotations ($s \in [-1.5, 1.5]$). The safety factor $q = 1.8$ is a non-integer rational value, and therefore the flux tube would be closed if more rotations would have been shown.

netic field and periodic boundary conditions are applied. Flux tube simulations used in chapters 5 and 6 are considerably less computationally expensive compared with global simulations (chapter 4), but do not retain profile effects and, for instance, do not recover the momentum flux due to the radial inhomogeneity.

Chapter 3

Implementation of an eigenvalue solver

In this chapter an overview is given of the implementation of the eigenvalue solver into GKW. After the motivation for the implementation of this solver, a brief overview of the theoretical background is given. The last sections then discusses the test cases as well as the results.

3.1 Motivation

Frequency and growth rate of the most unstable mode can be obtained with GKW by time integration of the initial value problem. The initial perturbed distribution excites several modes, but only the fastest growing mode survives, as the amplitude of the other modes will decay, in comparison, with time. The result of a simulation is thus the mode with the highest growth rate for the given parameters. Advantage of this method is its robustness.
Nevertheless, there are also some disadvantages. While theoretical possible, it is practically very difficult to obtain other modes than the fastest growing mode. Neither is it possible to get multiple modes with different growth rates. In nonlinear simulations energy is transferred between modes, and also modes with smaller and even negative growth rate (i.e. linearly decaying) are excited. These affect the dynamics of the system, and computing these modes helps to understand the dynamics of the nonlinear simulations.
Finally, the computation time in the time integration method increases strongly, if there are two modes with approximately equal growth rate. An example is shown in Fig. 3.1, which gives the growth rate/frequency versus time for different values of $k_\theta\rho$. At $k_\theta\rho = 0.15$ the most unstable mode is a kinetic ballooning mode, while at $k_\theta\rho = 0.3$ a micro tearing mode is found. In between at $k_\theta\rho = 0.2$ both modes are present with approximately equal growth rate. Extremely slow

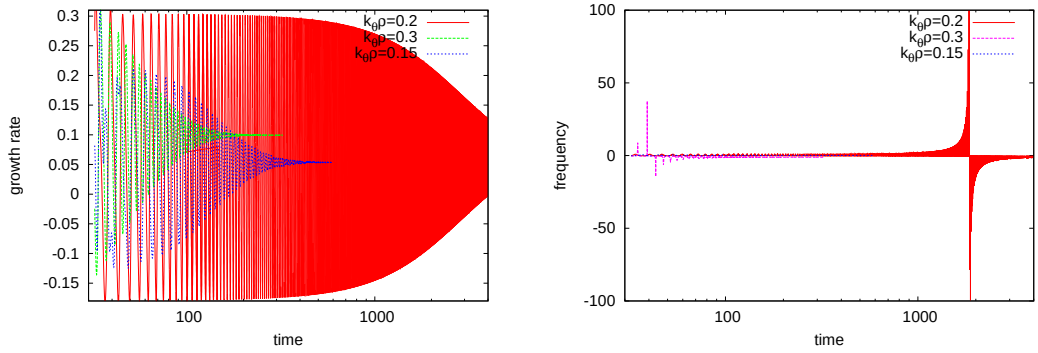

Figure 3.1: Example for runs with mode with similar growth rates. Note the logarithmic scaling of the x-axis. While $k_\theta\rho = 0.15, 0.3$ correspond to a situation where one mode is dominant, $k_\theta\rho = 0.2$ is in-between, and both modes have a similar growth rate. This causes the convergence to be much slower, thus the simulation must be computed much longer. For parameters see shot # 129061 in Tab. 6.1.

convergence is observed, with large, slowly damped oscillations, that can be attributed to the beating of the two modes.
For these three problems using an eigenvalue solver is the natural solution. In general such a solver is used to determine the eigenpairs, i.e. the eigenvalue λ and eigenvector $\underline{a}$, of a linear operator L

$$L\underline{a} = \lambda\underline{a}. \tag{3.1}$$

In GKW the eigenvalue is related to growth rate and frequency of the mode.

3.1.1 Requirements for an external library

The equations solved in GKW have been given in chapter 2. For numerical implementation the distribution function has to be discretized. The total number of grid points will be referred to as system size. Even the smallest problems have thousands of grid points, while for linear simulations of micro tearing modes up to six million points are used. Computing all six million eigenpairs is an impossible task and therefore projectional or subspace methods are used to solve for a limited amount of interesting eigenpairs only. In these methods the system size is reduced, by projecting the discretized model to a smaller subspace, that contains the wanted eigenpairs.
Instead of writing a new eigenvalue solver it is advantageous to use a library package. To proceed it is noted that the eigenvalue problem in GKW has a form

different from Eq. (3.1):

$$\begin{pmatrix} f_{t+dt} \\ 0 \end{pmatrix} = \begin{pmatrix} A & B \\ C & D \end{pmatrix} \begin{pmatrix} f_t \\ \Phi \end{pmatrix}, \tag{3.2}$$

where Φ represents all the perturbed fields. A, B, C and D represent sparse sub matrices, with B and C is the coupling between fields and distribution. The lower row is the Poisson equation, the upper the gyrokinetic equation.
This matrix equation can be transformed to

$$f_{t+dt} = (A - BD^{-1}C)f_t = Lf_t, \tag{3.3}$$

but in general the inverse of a sparse matrix is not sparse and, therefore, L is not a sparse matrix. Equation (3.3) will then require much more operations per time step compared to Eq. (3.2) and thus will be slow. To be able to use the problem in the form of Eq. (3.3), a method must be used in which only the matrix vector multiplication Lf_t is required. This matrix vector multiplication is then not obtained for the non-sparse matrix L, but rather through the solution of Eq. (3.2).
The system size poses another requirement: due to the large systems that have to be handled, the eigenvalue solver should be parallelized. Furthermore, as the equation is treated with a spectral method, the matrix used in GKW is complex and non-hermitian, and thus the library has to support this type of matrix.
Based on the points discussed above, the Scalable Library for Eigenvalue Problem Computations (SLEPc) [47], has been used. This library is build upon the Portable, Extensible Toolkit for Scientific Computation (PETSc) [48].
SLEPc/PETSc are parallelized. SLEPc can handle complex, non-hermitian problems and allows to define a matrix by the result of a matrix-vector multiplication. The library offers different options, but not all of them are made available to GKW. For example the eigenvalue solver used by SLEPc can be changed, but not all of them support complex non-hermitian matrices (see for example Tab. 2.4 of the documentation [49]).

3.2 Theoretical background

Here only a very brief overview of the theoretical background of projectional methods will be given, following the book by Saad [50]. More details about the implementation in SLEPc can be found in the technical reports [51, 52, 53] as well as the documentation [49].
Consider an equation of the type

$$A\underline{x} = \underline{b} \tag{3.4}$$

with a matrix $A \in \mathbb{C}^n \times \mathbb{C}^n$ and vectors $\underline{x}, \underline{b} \in \mathbb{C}^n$. The connection to the eigenvalue problem will be made below.

For this type of equation, one can try to get an approximate solution for $\underline{x}$ from a subspace K of $\mathbb{C}^n$, by using a projection technique. So let K be a subspace of $\mathbb{C}^n$, of dimension $m < n$. K is called search subspace or subspace of candidate approximants. In general also m constraints are necessary to extract the solution from this subspace. These constraints define the subspace of constraints L, with dimension m. A typical choice for the constraints, is orthogonality, i.e. the residual $\underline{b} - A\underline{x}$ must be orthogonal to m independent vectors. This type of constraint will be assumed in the remainder of this section.
There are two classes of projection methods. In the orthogonal ones, the search subspace and the subspace of constraint are the same $K = L$. In oblique methods on the other hand they are different or even totally unrelated.
The problem to solve is in both cases, find

$$\underline{x} \in \underline{x}_0 + K \tag{3.5}$$

($\underline{x}_0$ is the initial guess) such that the residual fulfils the orthogonality condition

$$\underline{b} - A\underline{x} \quad \perp \quad L. \tag{3.6}$$

This can be rewritten using

$$\underline{r}_0 \quad = \quad \underline{b} - A\underline{x}_0 \tag{3.7}$$

and

$$\underline{x} \quad = \quad \underline{x}_0 + \underline{\delta} \tag{3.8}$$

as finding $\underline{\delta} \in K$ with

$$\underline{b} - A\underline{x} = \underline{b} - A\underline{x}_0 - A\underline{\delta} \quad = \quad \underline{r}_0 - A\underline{\delta} \perp L \tag{3.9}$$

or

$$(\underline{r}_0 - A\underline{\delta}, w) \quad = \quad 0, \forall w \in L. \tag{3.10}$$

This orthogonality condition is sketched in Fig. 3.2.

This is the basic form of a projection step. In general more iterations will be necessary to obtain an approximation to the real solution x_* of the linear equation, that is "good enough". The subspaces K and L may change with each iteration.
Introducing two $n \times m$ matrices (V and W), whose column vectors form a basis of K and L respectively, the last equation can be reformulated as searching $\underline{x} = \underline{x}_0 + V\underline{y}$ ($y \in K$) with

$$0 \quad = \quad W^*(\underline{r}_0 - AVy) \tag{3.11}$$

$$W^*AV\underline{y} \quad = \quad W^*\underline{r}_0. \tag{3.12}$$

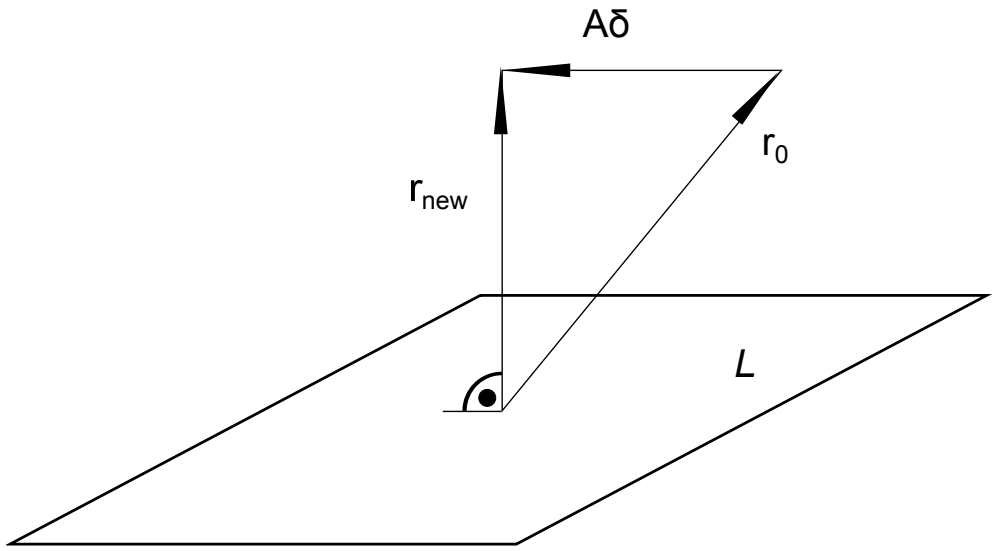

Figure 3.2: Sketch of the orthogonality condition: The vector δ is determined such, that the new residual is orthogonal to the subspace L.

Using this, the new approximation can be written as

$$\underline{x} = \underline{x}_0 + V(W^*AV)^{-1}W^*r_0 \tag{3.13}$$

provided W^*AV is non-singular. From this a prototype for a projection algorithm can be given as [50, Algorithm 5.1]

```
Until convergence, Do
    Select a pair of subspaces K and L
    Choose bases V = {v_1, ..., v_m}
             and W = {w_1, ..., w_m} for K and L
    r := b - Ax
    y := (W*AV)^{-1} W*r
    x := x + Vy
End Do
```

It is left open at this point, how the convergence is determined. The most common solution should be the 2-Norm of the residual r.
As example, with $m = 1$, consider the steepest descent, with a symmetric and positive definite matrix A and the choice $v = w = r$ (i.e. $K = L$) [50, Algorithm 5.2],

```
Compute r = b - Ax and p = Ar
Until convergence, Do
    α ← (r,r)/(p,r)
    x ← x + αr
    r ← r - αp
```

```
    Compute p := Ar
End Do
```

This version avoids one of two matrix vector products of a straightforward implementation. Each step minimizes the norm

$$f(x) \quad = \quad ||x - x_*||_A^2 = (A(x - x_*), (x - x_*)), \tag{3.14}$$

over all vectors of the form $x + \alpha d$ with $d = -\nabla f$.
To make the connection with the prototype assume $n = 1$. Then

$$x \leftarrow \quad x + W(W^*AW)^{-1}W^*r \tag{3.15}$$

$$= \quad x + W\frac{1}{WAW}Wr \tag{3.16}$$

$$= \quad x + \frac{1}{A}r \tag{3.17}$$

where in the first step $V = W$ has been used and in the second step $W \in \mathbb{C}$, as we consider here a 1-dimensional example. The same result can be obtained for the example algorithm

$$x \leftarrow \quad x + \alpha r \tag{3.18}$$

$$= \quad x + \frac{r \cdot r}{Ar \cdot r}r \tag{3.19}$$

$$= \quad x + \frac{1}{A}r. \tag{3.20}$$

(Inserting the definition for r, the result is $x = b/A$, i.e. the exact solution x_* is obtained after one step.)
An important class of projection methods use as subspace K the Krylov subspace. The Krylov subspace K_m is defined as,

$$K_m(A, \underline{r}_0) \quad := \quad span\{\underline{r}_0, A\underline{r}_0, A^2\underline{r}_0, \ldots, A^{m-1}\underline{r}_0\} \tag{3.21}$$

where $\underline{r}_0 = \underline{b} - A\underline{x}_0$. Different kinds of Krylov methods arise by choosing the subspace of constraint L_m and also by different choices for preconditioning.
The typical complexity of such an algorithm is $\propto m^2 n$. This means on one hand, that even for large systems (large n) the computation time remains limited. On the other hand it means that getting many solutions will get expensive, as with the number of eigenmodes the size of the subspace should be increased.
A quite simple and common method is based on Arnoldi's method. It was proposed 1951 for reducing a matrix to Hessenberg form, but Arnoldi suggested already that it could be used to get approximations of some eigenvalues. This method computes a basis of the subspace K and can be given as follows [50, Algorithm 6.1],

```
Choose a vector v_1 such that ||v_1||_2 = 1
For j = 1,...,m, Do
     Compute h_ij = (Av_j, v_i) for i = 1,...,j
     Compute w_ij := Av_j − Σ_{i=1}^{j} h_ij v_i
     h_{j+1,j} = ||w_j||_2
     If h_{j+1,j} = 0 then Stop
     v_{j+1} = w_j/h_{j+1,j}
EndDo
```

First choose a normalised starting vector, then at each step, multiply the previous vector by A and normalise it with Gram-Schmidt (or alternative, e.g. modified Gram-Schmidt, Householder). If the vector vanishes, stop, otherwise repeat (up to m times). The result is a Hessenberg matrix from which the eigenvalues can be calculated, and which are approximations of the eigenvalues of the original matrix. Thus here is the connection to the eigenvalue problem.
This method is a basis for many projection algorithm. Of course this simple scheme can be improved. One particular important improvement is restarting. As with each iteration more time and memory is needed, there is an upper limit that is feasible. To accommodate this, implementations often stop after a certain (adjustable) number of steps and then start anew, using the information gathered so far.
The Krylov-Schur method is a particular important variant because of its combination of reliability and efficiency. For this reason it is also the default solver in SLEPc. For details and differences to the simple version of Arnoldi's method given above consult the SLEPc technical report number 7 [52].

3.3 Tests and Results

In this section some of the tests and results that have been obtained with the eigenvalue solver are described.
But first a few remarks regarding the implementation of SLEPc. Three of SLEPc's solvers are made available: the default Krylov-Schur solver, generalized Davidsen and Jacobi-Davidsen. Furthermore one can choose which eigenvalues should be determined. Largest real part (corresponds to largest growth rate) might be the most obvious choice. Another example would be to look for eigenvalues close to a given growth rate and/or frequency, which is an input parameter (the documentations of SLEPc and GKW refer to this also as target).

3.3.1 First tests

The first check is if the growth rate and frequency match those of the time integration scheme. A parameter set was chosen at which a change of the mode, from ITG to TEM, occurs, when R/L_{T_i} is decreased. The parameters chosen for the first test are those of the Waltz standard case. The wave vector is $k_\theta \rho = 0.43$, the safety factor $q = 2.0$, with magnetic shear $\hat{s} = 1.0$, and inverse aspect ratio $\epsilon = 0.1666$. The density gradient $R/L_n = 3.0$ and the electron temperature gradient $R/L_{T_e} = 9.0$ are held constant, while the ion temperature gradient R/L_{T_i} is varied. The simulations are electrostatic with kinetic electrons and without collisions. The timestep is $2 \cdot 10^{-3}$, $N_s = 165$ grid points along the magnetic field have been distributed over a total of 11 field line rotations. The velocity grid is discretized with $N_\mu = 8$ magnetic moment grid points and $N_{vpar} = 32$ parallel velocity grid points. Two eigenvalues are determined for each R/L_{T_i} and eigenvalues are searched close to the target value $(\gamma, \omega) = (0.247, 0.504)$.
The growth rate and frequency are shown in Fig. 3.3. It can be seen that it is

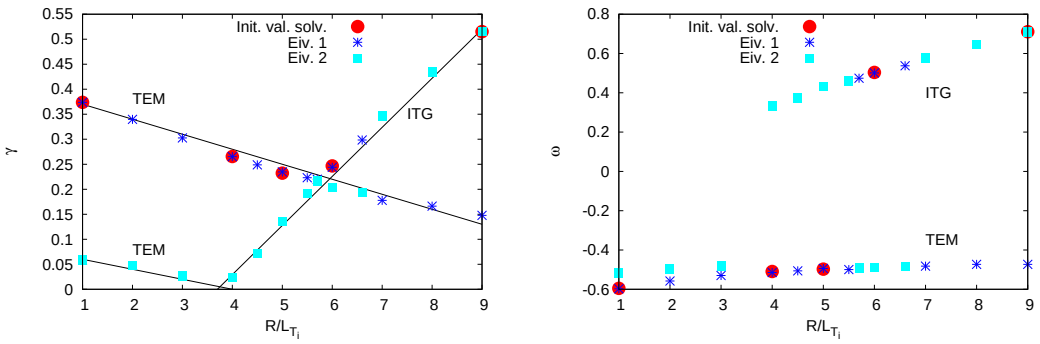

Figure 3.3: Scan over ion gradient length R/L_{T_i} with the eigenvalues solver. Shown are growth rate (left) and the real frequency (right). The result of the initial value solver is also given ('Init. val. solv.'). The lines in the figure for the growth rate are to guide the eye and represent the different branches.

possible to follow the sub dominant mode, but the first eigenvalue is not necessarily the one with the highest growth rate. This is related to the settings of the eigenvalue solver, as the mode that is closest to the target growth rate is found first.
For low ion temperature gradient there are two TEMs, while for higher values a TEM and an ITG is found. Thus in the whole region there are at least two unstable modes.
This test shows already one important point. Namely that the modes are not necessarily found ordered according to the growth rate. One reason is that a growth rate closest to the target value is sought for. The transformation between growth rate and frequency ($\gamma + i\omega = \lambda_{GKW}$) on one hand and the eigenvalue

Table 3.1: Modes found in the advanced test at base parameters

#	γ	ω	mode
1	1.085	-1.158	TEM
2	0.956	-1.114	MTM
3	0.423	1.262	ITG
4	0.178	1.222	MTM/ITG behaviour
5	0.150	1.368	ITG
6	0.111	2.141	MTM/ITG behaviour

found by SLEPc (λ_{SLEPc}) on the other hand can be another reason. This transformation is nonlinear ($\lambda_{GKW} = \log(\lambda_{SLEPc})/\Delta t_{diagnostic}$) and while $\omega_{1,SLPEc} > \omega_{2,SLPEc} \rightarrow \omega_{1,GKW} > \omega_{2,GKW}$ and $\gamma_{1,SLPEc} > \gamma_{2,SLPEc} \rightarrow \gamma_{1,GKW} > \gamma_{2,GKW}$ usually holds, this need not to be the case for distances (i.e. $|\lambda_{1,SLEPc} - \lambda_{2,SLEPc}| > |\lambda_{3,SLEPc} - \lambda_{4,SLEPc}|$ and $|\lambda_{1,GKW} - \lambda_{2,GKW}| < |\lambda_{3,GKW} - \lambda_{4,GKW}|$ is possible). One should keep this in mind in every setting that requires one or both target values.
A second point to keep in mind should be mentioned here. To obtain the desired eigenvalues one must sometimes increase the number of eigenvalues requested.

3.3.2 Results

As the eigenvalue solver is useful for finding multiple modes, it has been used to shed more light on the modes present under experimental conditions in NSTX. The used parameter set is based on the momentum and particle transport case, from chapter 6 for $k_\theta \rho = 0.6$. Size and resolution in s-direction have been a bit decreased, to allow for faster computation. The plasma rotation is neglected and the geometry is approximated by circular surfaces. The simulations remain full electromagnetic with pitch angle collisions. Tungsten, present in chapter 6 as a trace species, has been removed since trace species do not affect growth rate and frequency. The reader is referred to Tab. 6.1 and 6.3 for the parameter values.
Under these conditions the most unstable mode is a trapped electron mode (TEM), as found by the initial value solver. Its growth rate is about five times higher than those of the micro tearing mode (MTM) found at the same $k_\theta \rho$ in the simulations of chapter 6.
The eigenvalue solver was then set up to find the eigenvalues with the largest magnitude, using the default Krylov-Schur solver, but with harmonic extraction (instead of Ritz). The target, needed by the harmonic extraction, was set to $(0.4, 0.0)$ (growth rate and frequency, respectively). Six eigenvalues have been obtained. See Tab. 3.1 for growth rate, frequency and type, and Fig. 3.4 for a plot of ϕ, $A_\parallel$ and $B_\parallel$ of the modes. It should be noted that the eigenvalue solver needed only $\sim 45\%$ ($\sim 35,000$s vs. $\sim 84,800$s with 8 processors) of the time

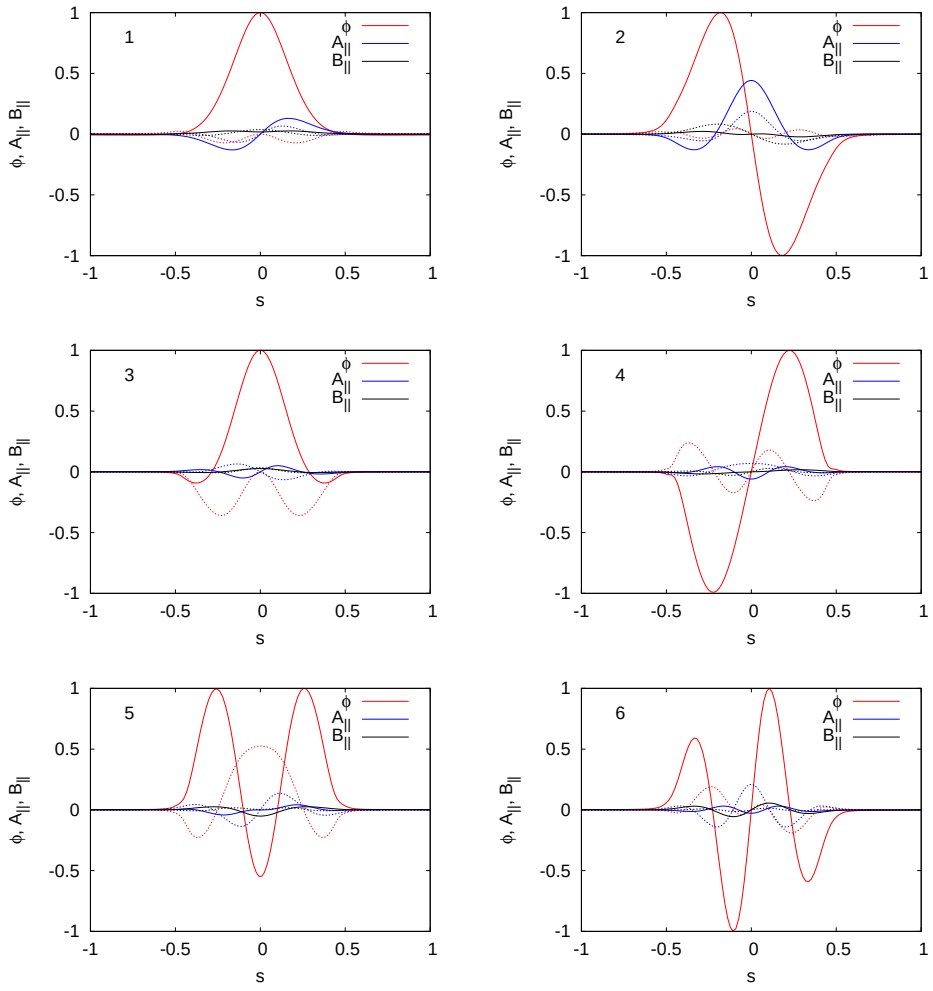

Figure 3.4: Modes found by the eigenvalue solver for the default case in the advanced test. Solid lines are the real parts, dashed lines the negative part. The number correspond to the mode number in Tab. 3.1.

of the explicit time integration scheme, despite finding six eigenvalues instead of one. Here the method is particularly fast, probably because the growth rates of the two fastest growing modes do not differ by much.
This parameter set has multiple eigenvalues, thus it has been used as a basis for parameter scans. This was done for two reasons, first of course, to prove one can trace the modes, but also to give better reasoning for the type of the instability. The first mode shows the typical patterns of a TEM (electron direction, symmetric potential, antisymmetric parallel magnetic potential) and as will be shown below, the mode also behaves like a TEM. Mode 4 and 6 on the other hand look like much like a MTM (antisymmetric electrostatic potential, symmetric, in-phase, parallel magnetic potential), but they move in the wrong direction (sign

of ω) and the magnetic parallel potential is out-of-phase. Furthermore it will be shown below, with the help of parameterscans, that the modes do not behave like a MTM, but more like an ITG, which is the reason why they are labelled as "MTM/ITG behaviour".
Five scans have been performed. In each of these scans only one parameter has been varied, namely the temperature gradient length of the ions, those of the electrons, the density gradient length of the ions (those of the electrons are changed too, to preserve charge-neutrality), β_{ref} and $k_\theta\rho$, respectively. Plots of growth rate and frequency can be found in Fig. 3.5-3.9, with the base value of the parameter marked via a vertical line. The figures 3.5-3.9 show, that multiple

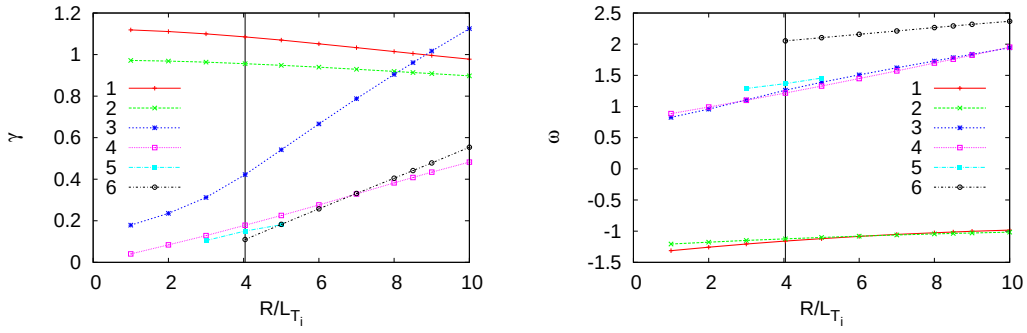

Figure 3.5: Growth rate and real frequency plotted against the ion temperature gradient length for the different modes. The number correspond to the mode number in Tab. 3.1.

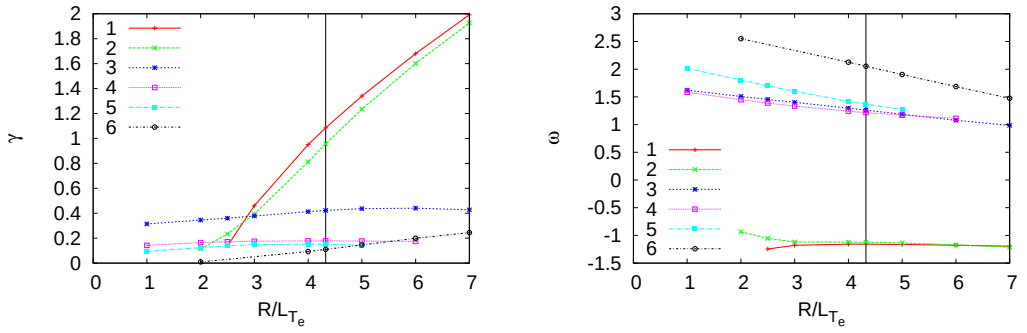

Figure 3.6: Growth rate and real frequency plotted against the electron temperature gradient length for the different modes. The number correspond to the mode number in Tab. 3.1.

unstable modes can be found in a rather large part of the considered parameter space. Only in a narrow region of parameterspace less than three modes were found. What can also be observed is, that the two most unstable modes have

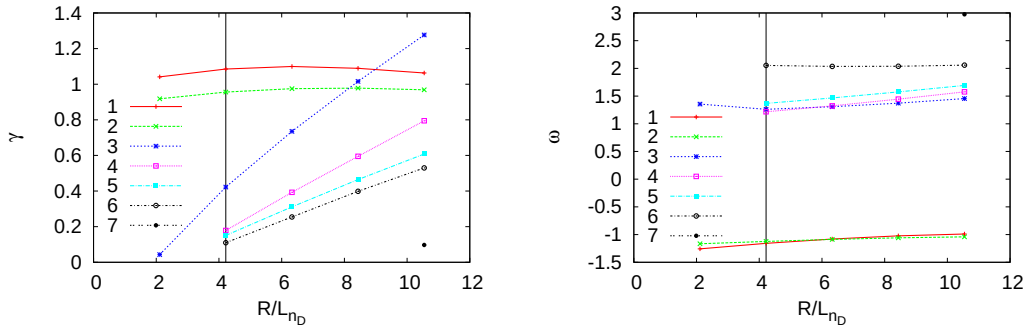

Figure 3.7: Growth rate and real frequency plotted against R/L_{n_D} (other density changed accordingly, to fulfil quasi neutrality) for the different modes. The number correspond to the mode number in Tab. 3.1. The additional mode (nr. 7) has only been found in this scan.

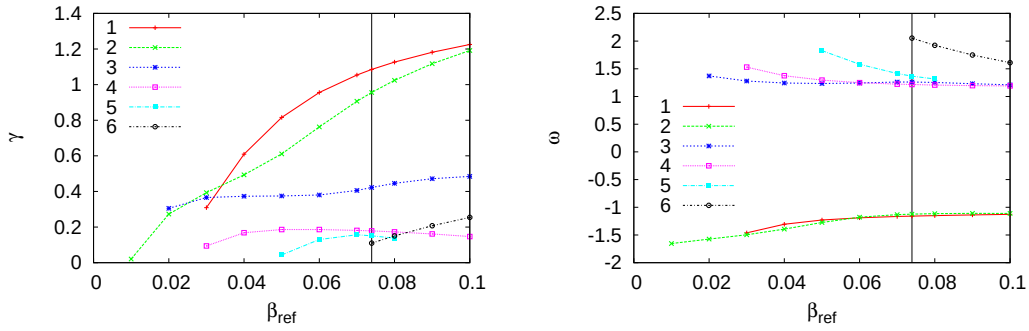

Figure 3.8: Growth rate and real frequency plotted against β_{ref} for the different modes. The number correspond to the mode number in Tab. 3.1.

comparable growth rates over a large part of parameterspace. This suggests, that the explicit time integration scheme might have been slower than the eigenvalue solver, as was the case for the base parameters. The time needed by the eigenvalue solver varies between 60% and 200% compared with the base case.
It has been argued before, that the first mode is a TEM, and the scans support this. Growth rate depends on the temperature gradient of the electrons, but not on the ion temperature gradient, and it reacts strongly to a decrease of β_{ref}.
The type of mode 4 and 6 was not clear from the plot of the perturbed potentials, and the behaviour in the scans make the situation not easier. Both modes react to the ion temperature gradient and to the density gradient, but not to the electron temperature gradient. While mode 6 might have a small dependence on β_{ref}, mode 4 is seemingly unaffected. Thus there are modes that look similar to a MTM, while moving in ion diamagnetic direction and behave like an ITG. The latter, is the reason why they are labelled as "MTM/ITG behaviour" in Tab. 3.1.

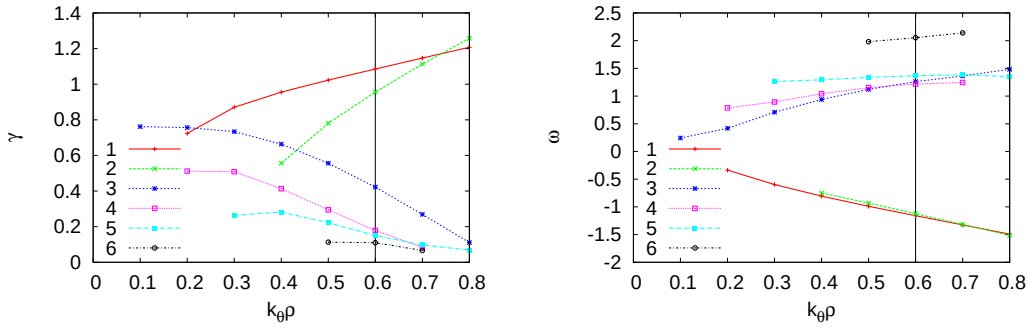

Figure 3.9: Growth rate and real frequency plotted against $k_\theta\rho$ for the different modes. The number correspond to the mode number in Tab. 3.1.

The modes, i.e. ITG, TEM and MTM, have been derived in reduced models, which are probably incomplete when compared with the solution of the complete linear gyrokinetic equation. Thus it is not unexpected, that the classical mode labels (e.g. ITG, TEM, MTM, KBM) are not sufficient here.
One should keep in mind, that the eigenvalue solver might not be in all cases helpful. In some cases it was not possible to determine the eigenmodes. Of course, not the whole solver-parameter space has been searched, as these is to big. Other target values, sizes of the reduced problem or targets might have helped. If not, switching to another solver could have been done, to get an eigenvalue.
The scan over $k_\theta\rho$, Fig. 3.9 is a good example for the problems that can occur. The default value was $k_\theta\rho = 0.6$. At lower values the resolution in s was for some modes not sufficient and it had to be increased, which also increases the time needed for the computation. At the same time also the needed number of iterations increased, due to a worse separation of the modes, with respect to the eigenvalues. For $k_\theta\rho = 0.7$ on the other hand, looking for the biggest eigenvalue, did find only non-physical modes, i.e. very high or low growth rate and frequency. Switching to largest real part solved this, but at $k_\theta\rho = 0.8$ the problem reappeared.
In other cases [54] the spectrum that has been found consisted of some eigenvalues with small absolute frequency, which includes the fastest growing mode and a band of stable modes. This band is located at growth rates whose absolute value is small. Assuming that this structure is also present in our simulations, it sheds some light on one reason why the eigenvalue solver fails, e.g. in the case mentioned above. It seems reasonable to assume that the projection method will not work, if the wanted part of the spectrum is hard to separate from the rest of the spectrum. If the growth rate of the eigenvalues are small, then these are closer to the band of eigenvalues. Thus they should be harder to separate from these, and the eigenvalue solver fails in finding these modes, or at least needs more iterations.

3.4 Other use cases

The eigenvalue solver has been used in simulations for the chapters of profile shearing (chapter 4) and momentum transport in NSTX (chapter 6) in a support function. In the former case a scan over ρ_* in linear, global simulations is performed. In the latter case the simulations are made for a flux tube, while adding physics (finite β_{ref}, collisions, rotation). Unfortunately, the eigenvalue solver was not always successful in this case. One case where it was successful is the example from the motivation. The eigenvalue solver was a factor $5 - 10$ faster compared to the explicit time integration, but still required $\sim 50h$.
The eigenvalue solver has also been used by Casson and coworkers [55] to investigate the influence of sub-dominant modes on electron transport.

3.5 Conclusions

The possibility to use an eigenvalue solver has been made available in GKW by creating an interface to an existing library.
This method allows to find multiple eigenmodes, compared to only the fastest growing mode when an initial value problem is integrated. It is also possible to trace these modes in parameter scans, which can help to identify modes. In the case that there are two modes with approximately equal growth rate the eigenvalue solver is faster than the explicit scheme.
Different settings (local/global, collisions, rotation) and parameters are possible. Disadvantage is, that it is often hard to tell what the parameters of the eigenvalue solver have to be, to find the mode(s) one is looking for.
From the experience gained so far, it seems that the eigenvalue solver works well, as long as the wanted eigenmodes are well separated from the rest. To explain this see Fig. 3.8 and assume you are looking for the two fastest growing modes. These should be obtained easily and fast for high values of β_{ref}. At lower values the separation of the two fastest growing modes to the third (forth, etc.) mode gets smaller and thus it should take longer and may require the options to be closer to the "optimum".
To conclude, what for the eigenvalue solver is missed so far, is a rather clear idea of when to choose which options/parameters, to make the use more reliable.

Chapter 4

Toroidal momentum transport

This chapter has been published as a paper [56].

4.1 Introduction

In a toroidally symmetric tokamak, the toroidal angular momentum is conserved. The radial toroidal rotation profile is then determined by the torque on the plasma in combination with the radial momentum transport generated by small scale turbulence. The gradient of the toroidal rotation has been observed to be significant, and can both add to the drive of the turbulence, as well as have a stabilizing effect through ExB shearing [27, 57, 58]. In the latter case, energy and particle confinement are improved with increasing plasma rotation.
In recent years, it has been observed that the flux of toroidal momentum has non-diagonal contributions [41, 42, 59, 43, 60, 61, 62, 63, 64, 65, 66, 67]. The non-diffusive momentum flux generates a rotation gradient, even in the absence of a torque on the plasma and can, therefore, lead to improved confinement. This is of particular interest to a reactor, where the external torque is expected to be small.
A recent overview of toroidal momentum transport theory can be found in Ref. [46]. Toroidal momentum transport is generated by a symmetry breaking [44, 45]. To lowest order in the normalized Larmor radius $\rho_* = \rho/R$ (here ρ is the ion Larmor radius and R the major radius of the magnetic axis), a finite momentum flux is generated by a gradient in the rotation [68], the Coriolis pinch [69, 70], or an up down asymmetry in the equilibrium [71, 72]. At next order, finite Larmor radius effects enter, with several mechanisms proposed in the literature: the effect of the neo-classical equilibrium flows [73], ExB shear [74, 75, 76, 77, 78], the radial gradient of the turbulence intensity [79], profile shearing [30, 80], and higher order ρ_* parallel derivatives [81]. While the finite Larmor radius effects are generally smaller compared with the lowest order, they can be expected to dominate in

the plasma edge, where the gradients are large, as well as in the core for slowly rotating plasmas [46].
This chapter concentrates on the effect of profile shearing, studied previously in linear theory in Ref. [30] and through non-linear simulations in Ref. [80], and more recently also through full-f simulations [82]. This effect is predicted to be sizeable, and has been invoked to explain some of the experiments on ASDEX Upgrade [83]. The chapter addresses several of the outstanding questions. First the scaling of the effect with the normalized Larmor radius ρ_*. A linear model, developed in Ref. [30] predicts a weak scaling $\rho_*^{1/3}$, which is favourable for a reactor since it means that the momentum flux remains sizeable even at small values of ρ_*. Numerical simulations of Ref. [80], using a local model that has been extended to account for the second derivatives of the profile, however, find that for sufficiently small values of these second derivatives the momentum flux is linear in these derivatives (e.g. Fig. 2 of Ref. [80]). Since the profile shear rate through the second derivatives is proportional to ρ_* these results are consistent with a ρ_*^1 scaling, at sufficiently small ρ_*. The latter result is in agreement with simple scaling arguments presented in Ref. [46]. The second question that is addressed is whether the momentum flux is largely due to the second derivatives of the profile (as in Ref. [80]), or whether it is more linked to the first derivative (as in Ref. [30]). The final question addressed here is whether the momentum flux can alternatively be expressed as a gradient in the turbulence intensity [79].

4.2 Simulation set-up

Calculations have been performed with the gyrokinetic code GKW [21]. The model equation for the evolution of the perturbed distribution function $f = f(v_\parallel, \mu, \psi, \zeta, s)$ can be written in the form

$$\begin{aligned} \frac{\partial f}{\partial t} + \boldsymbol{v}_E \cdot \nabla f + (v_{||}\boldsymbol{b} + \boldsymbol{v}_D)\nabla f & \\ -\frac{\mu B}{m}\frac{\boldsymbol{B}\cdot\nabla B}{B^2}\frac{\partial f}{\partial v_{||}} &= S \end{aligned} \tag{4.1}$$

with the source term S

$$\begin{aligned} S &= -\boldsymbol{v}_E \cdot \left[\frac{\nabla n}{n} + \left(\frac{v_{||}^2}{v_{th}^2} + \frac{\mu B}{T} - \frac{3}{2}\right)\frac{\nabla T}{T}\right] F_M \\ &\quad -\frac{Ze}{T}\left[v_{||}\boldsymbol{b} + \boldsymbol{v}_D\right]\cdot\nabla\left\langle\phi\right\rangle F_M, \end{aligned} \tag{4.2}$$

In the equations above $\boldsymbol{v}_E = \boldsymbol{b}\times\nabla\langle\phi\rangle/B$ is the ExB velocity, $v_\parallel$ the parallel velocity, μ the magnetic moment, $\boldsymbol{v}_D$ the drift due to the magnetic field inhomogeneity, Z the charge number, T (n) the temperature (density), e the elementary

charge, $\mathbf{b}$ the unit vector along the magnetic field $\boldsymbol{B}$, v_{th} the thermal velocity, F_M the local Maxwellian, and ϕ the electro-static potential.
Note that all the terms in the source are proportional to both the Maxwellian as well as the electrostatic potential. The convection term $\boldsymbol{v}_D \cdot \nabla F_M$, responsible for the neo-classical perturbation is neglected here. Furthermore, a local Maxwellian (using the local value of density and temperature) is used on each of the flux surfaces. Without potential perturbation (ϕ) this local Maxwellian then is an equilibrium solution and no perturbation f develops. Consequently, neo-classical physics effects as discussed in Refs. [73, 84] are not included in our model. Furthermore, we neglect the parallel velocity nonlinearity, and also the finite ρ_* parallel derivatives described in Ref. [81], as well as other higher order ρ_* corrections (see for instance Ref. [82]), are not included in this study. In this chapter we will solely investigate the effect of profile shearing on turbulent dynamics.
GKW uses straight field line Hamada coordinates (ψ, ζ, s) [21]. In the global model these coordinates are constructed for each of the flux surfaces using a circular concentric flux surface model (keeping all orders in the inverse aspect ratio [37]). The drifts due to the field inhomogeneity, as well as the parallel and ExB convection are expressed in the coordinates in Ref. [21] and therefore, here, include the radial dependence due to the geometry. Because of the introduced radial dependence, the turbulence is no longer homogeneous in this direction, and the radial spectral representation used in the original version of the code (see Ref. [21]) is impractical and has been replaced by finite differences.
The potential perturbation is calculated using the Poisson equation

$$\sum_{sp} \left(Z_{sp} e \int \langle f \rangle^\dagger \, \mathrm{d}^3\mathbf{v} + \frac{Z_{sp}^2 e^2}{T_{sp}} \int (\langle\langle \phi \rangle\rangle^\dagger - \phi) F_{M,sp}(\mathbf{v}) \, \mathrm{d}^3\mathbf{v} \right) = 0, \quad (4.3)$$

where the sum is over all species (sp). The first term represents the charge density connected with the perturbed distribution function, and the second term the polarization density. Note that the latter is calculated using the local Maxwellian only, i.e. finite ρ_* effects due to polarization effects connected with the perturbed distribution are neglected. When the adiabatic electron approximation is used, which is the case in this chapter, the electron contribution in the equation above is replaced by

$$\frac{e n_e}{T_e} (\phi - \{\phi\}) \quad (4.4)$$

where the brackets $\{\}$ represent the flux surface average.
The angle brackets $\langle\rangle$ in the equation above represent the gyroaverage, which is calculated as a numerical average over a ring with a fixed radius equal to the local Larmor radius

$$\langle G \rangle(\mathbf{X}) = \frac{1}{2\pi} \oint \mathrm{d}\alpha \, G(\mathbf{X} + \boldsymbol{\rho}), \quad (4.5)$$

where α is the gyroangle. The same gyroaverage is used in both the evolution equation of the distribution function, as well as in the Poisson equation. The dagger on the brackets denotes the conjugate gyroaverage operator.
Stationary simulations are obtained using a modified Krook operator

$$\left.\frac{\partial f(v_\parallel,\mu)}{\partial t}\right|_K = -\gamma_K\left[\frac{1}{2}[f(v_\parallel,\mu)+f(-v_\parallel,\mu)]-\tilde{n}F_M(v_\parallel,\mu)\right]. \quad (4.6)$$

where

$$\tilde{n} = \int f\,\mathrm{d}^3\mathbf{x}, \quad (4.7)$$

and the Maxwell distribution (F_M) is defined such that it satisfies

$$\int F_M\,\mathrm{d}^3\mathbf{v}=1 \qquad \int\frac{1}{2}mv^2F_M\,\mathrm{d}^3\mathbf{v}=\frac{3}{2}T_0 \quad (4.8)$$

The Krook operator conserves density and parallel momentum, but not energy. It allows for stationary turbulence simulations in which the profile relaxation is 'damped' by the Krook operator. The damping rate of the Krook operator is an input parameter and chosen to be $\gamma_k = 0.02[v_{thref}/R_{ref}]$.
The radial size of the computational domain is $\psi = [0.01 - 0.358]$ for linear and $\psi = [0.03 - 0.358]$ for non-linear runs, where $\psi = r/R_0$ with r the minor and R_0 the major radius of the magnetic axis. The safety-factor profile is chosen parabolic

$$q(\psi) = 0.854 + 17.037\psi^2, \quad (4.9)$$

and is shown in Fig. 4.1 (bottom) together with the corresponding magnetic shear (s).
Density and temperature profiles have the same shape as those of Ref. [30]:

$$X = X_0\exp\left[\frac{w_\psi}{L_X}\tanh\left(\frac{\psi-\psi_0}{w_\psi}\right)\right], \quad (4.10)$$

where X_0 is the value of the considered quantity at $\psi_0 = r_0/R_0$, w_ψ is the width of the profile (in $\psi = r/R_0$), and L_X is the gradient length of the profile normalized with the major radius (R_0). The parameters used in this chapter are $\psi_0 = 0.179$, $w_\psi = 0.1074$, $R/L_T = 6.92, 10.0$ (in linear/nonlinear simulations, respectively), and $R/L_N = 2.22$. Profiles of the gradient length are shown in Fig. 4.1.

All simulations are electro-static and use the adiabatic electron approximation. The relevant instability is, therefore, the ion temperature gradient (ITG) mode. The grid sizes are as follows: The number of grid points along the magnetic field is $N_s = 32$ for linear and $N_s = 16$ for non-linear runs. The number of grid points in the magnetic moment (μ) direction is $N_\mu = 32$. The number of grid points in

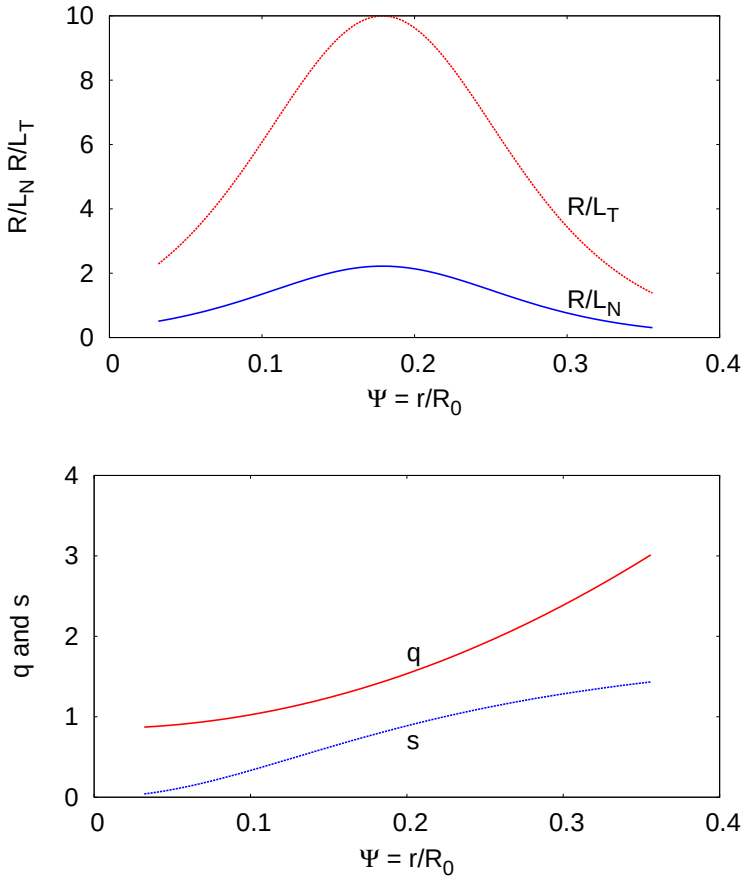

Figure 4.1: Top: normalized gradient lengths of temperature (R/L_T) and density (R/L_N) as a function of the radius $\psi = r/R_0$. Bottom: safety factor (q) and magnetic shear (s) as a function of the radius (ψ).

the parallel velocity direction is $N_{v_\parallel} = 64$. The maximum μ value on the grid is 9 times the μ value of an ion with a perpendicular velocity equal to the thermal velocity ($\sqrt{2T_i/m_i}$) at $\psi = \psi_0$, and the maximum parallel velocity represented on the grid is 4.2 times the thermal velocity of an ion at $\psi = \psi_0$. A scan in $\rho_* = \rho/R$ is performed and the grid sizes perpendicular to the field are scaled accordingly in order to have the same resolution relative to the Larmor radius perpendicular to the field. For $\rho_* = 2 \cdot 10^{-3}$ the number of radial grid points is $N_x = 320$, and 28 toroidal modes are used with a spacing in toroidal mode number of $\delta n = 2$. Non-linear simulations are run for roughly 2000 R_0/v_{th} time units (the time domain has been extended to 4400 for the $\rho_* = 10^{-3}$ case), and when time averaged quantities are given, these have been averaged over roughly the last 800 R_0/v_{th}.
Nonlinear simulations are started with a local Maxwellian without any rotation. Conservation of angular momentum then demands that the total angular

momentum of the plasma remains zero. This is true, but for the boundary conditions. The Dirichelet boundary conditions applied at both radial ends of the domain allow a flow of momentum across the boundary and therefore a spin up of the plasma in the computational domain. The profiles though are chosen such that the gradients close to the boundaries are small and turbulence is reduced close to the boundaries. One, therefore, expects angular momentum to be approximately conserved in the computational domain. The numerical accuracy of the simulations can be checked by calculating the toroidal angular momentum

$$\delta p_\phi \quad = \quad \frac{\int\int \frac{RB_t}{B} v_\parallel f \, \mathrm{d}^3\mathbf{v}\mathrm{d}^3\mathbf{X}}{\int \frac{RB_t}{B} | \int v_\parallel f \, \mathrm{d}^3\mathbf{v} | \mathrm{d}^3\mathbf{X}} \tag{4.11}$$

Using the time averaged (over the last 800 time steps) distribution, we have found $p_\phi < 0.1$ suggesting an accuracy of (better than) 10% .

4.3 Linear theory

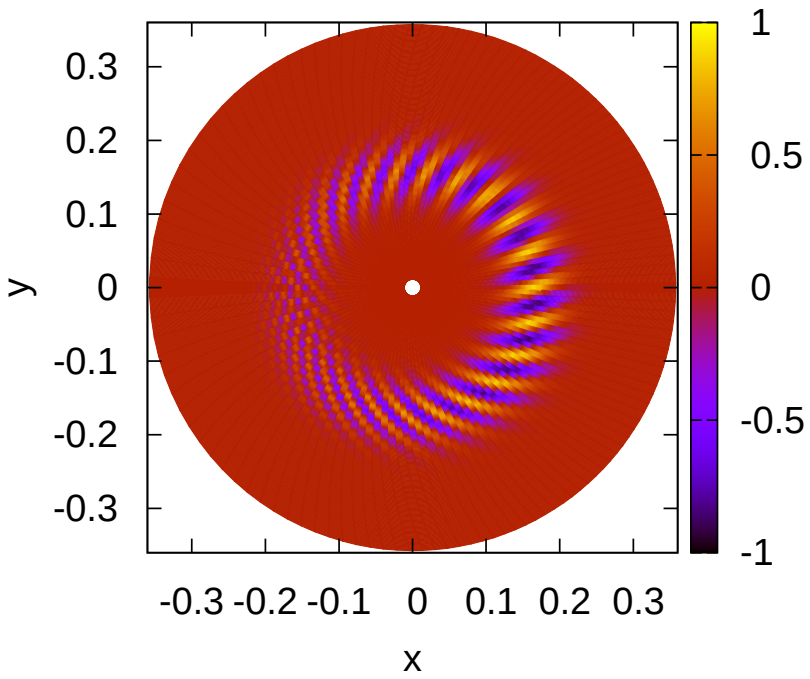

Figure 4.2: Contour plot of the potential perturbation of the $n = 19$ toroidal mode in the poloidal plane.

A radial dependence of the plasma and geometry parameters, referred to below as profile shearing, leads to a poloidal tilt of the eigenmode and a finite radial

wave vector (k_r) at the low field side, as shown in Fig. 4.2 (this particular simulation has been done with $N_s = 128$). The poloidal tilting angle is predicted to be proportional to $(d\omega_r/dr)^{1/3}$ [85], where $d\omega_r/dr$ is the radial derivative of the local frequency, which for the ion temperature gradient mode is related to the shear in the drift frequency $\omega_D \approx k_\theta T/ZeBR$ [30]. The breaking of the symmetry leads to the transport of toroidal momentum, with the analytic model developed in Ref. [30], predicting a $(\rho_* R/L_T)^{1/3}$ dependence for the most unstable mode. The flux tube simulations of Ref. [80], investigate the influence of the second derivatives of the profiles in simulations that have otherwise plasma and geometry parameters that are not a function of the radius. These simulations predict a toroidal momentum flux proportional to the second derivatives of the background profiles.
Besides the formulation of the momentum flux as function of the background profiles, an alternative description, for which the momentum flux is proportional to the gradient in the turbulence intensity, has also been proposed [79]. In Ref. [79] the effect of the intensity gradient is explained as follows: Modes with different toroidal and poloidal mode number are centred around the magnetic surface on which they are resonant. On this rational surface the parallel wave vector is zero, but it increases away from the surface, being, for instance, positive for larger radii and negative for smaller radii. At a specific radial position different modes overlap. The modes that have their resonant surface further inwards generate a positive parallel wave vector, whereas the modes that are resonant further out generate a negative wave number. In the presence of a radial intensity gradient, the modes that are resonant at different radial positions will have a different amplitude and, a net parallel wave vector results. The two effects, profile shearing and turbulence intensity gradient drive, are to some extent related. For instance, a gradient in R/L_T, i.e. a profile shearing effect, will lead to a gradient in the turbulence intensity. However, it is not expected, neither is it claimed, that all effects of profile shearing can be described in terms of a turbulence intensity gradient. Below we investigate to which extent the simulations results of this chapter can be described in terms of the intensity gradient model.

From the description above it is clear that the effect of the intensity gradient on the momentum transport is observable in linear theory, since a mode with a single toroidal mode number (n) consists of many modes with different poloidal mode numbers (m), which have different amplitudes and are resonant at different radial positions in the plasma. Fig. 4.3 shows the radial profile of the ion heat and toroidal momentum flux calculated for the parameters used above, and for a toroidal mode number $n = 24$. The ion heat flux, which is proportional to $|\phi|^2$ is, more or less, a bell shaped curve. Consequently, a momentum flux that is proportional to the intensity gradient would change sign as a function of radius. In contrast the calculated momentum flux is negative over the entire radial domain. In order to understand this result the potential perturbation decomposed

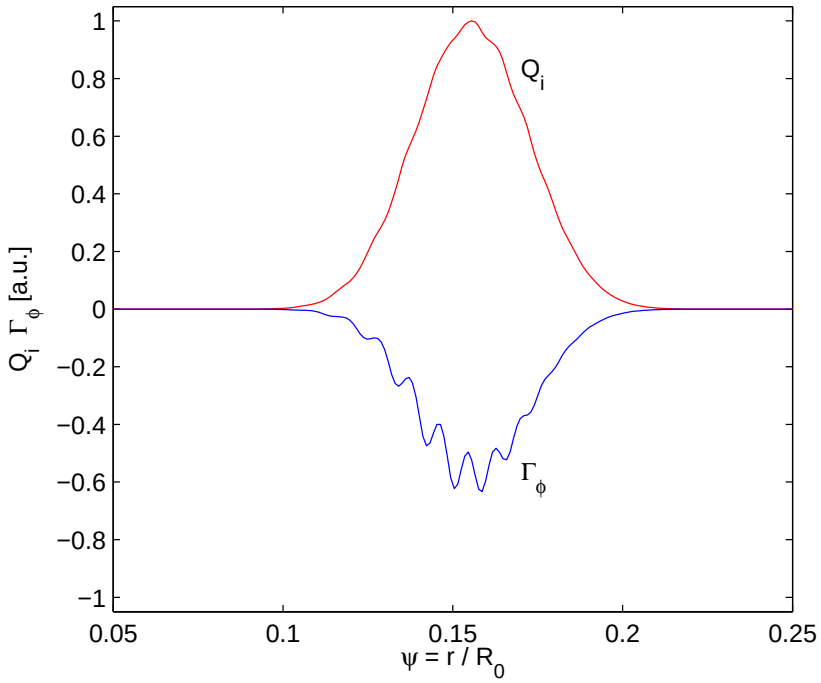

Figure 4.3: Ion heat flux and toroidal momentum flux as a function of $\psi = r/R_0$ for the toroidal mode $n = 24$.

in poloidal harmonics is shown in Fig. 4.4. In this figure also the rational surfaces on which these modes are resonant are indicated by black vertical lines. We note that the modes are neither symmetric around these rational surfaces, nor does their maximum coincide with the rational surface. Each of the poloidal modes therefore has a net finite parallel wave vector when averaged over the radial domain. It follows that, at least for the parameters studied here, the additional physics effects not captured in the description that considers the intensity gradient only, dominate over the intensity gradient drive. For this reason we prefer to discuss the physics of the momentum transport in terms of the profile gradients. To investigate the influence of the profile gradients, a series of linear runs with different profiles shapes (constant, linear, quadratic, the profile of Eq. (4.10). Examples shown in Fig. 4.5) were undertaken. Parameters of each of the profile functions were varied to obtain a total of 51 cases. Each of these had $\rho_* = 3 \cdot 10^{-3}$ with toroidal mode number $n = 19$. The dimensionless ratio of momentum flux to ion heat flux

$$\frac{\Gamma v_{thi}}{Q} = a_1 x_1 + a_2 x_2 + a_3 x_3 + a_4 x_4, \tag{4.12}$$

where v_{thi} is the ion thermal velocity at $\psi = \psi_0$, is studied. Γ and Q are the momentum and heat flux, respectively, averaged over the flux surface. It is invest-

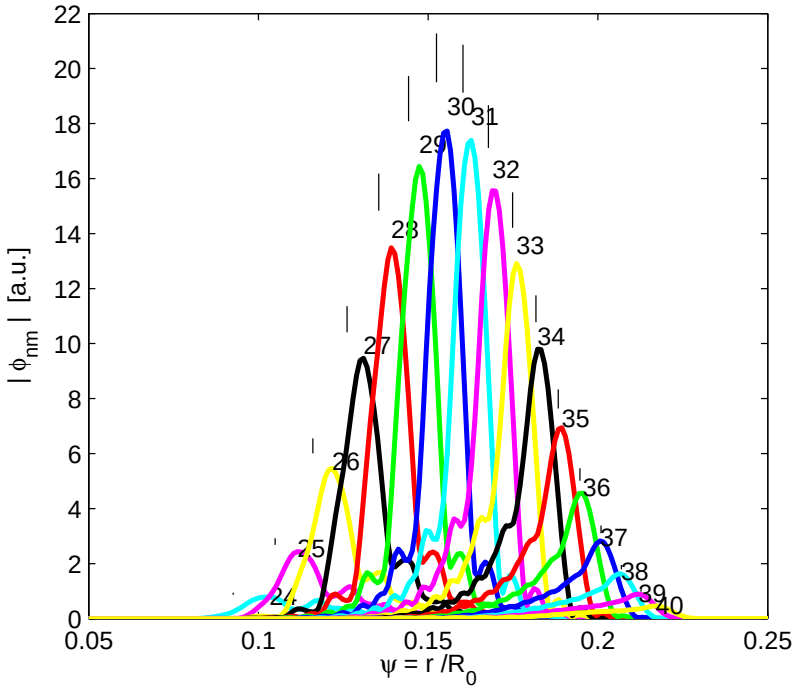

Figure 4.4: Amplitude of the various poloidal modes of the $n = 24$ toroidal mode as a function of $\psi = r/R_0$. Poloidal mode numbers are given in the figure. Vertical black lines indicate the rational surfaces on which these modes are resonant.

igated whether this flux can be written as a linear combination of the gradients and its derivatives. It was found that the radial location for which the mode reaches its maximum amplitude depends on the chosen profile and, consequently, profile parameters taken at a fixed position cannot describe the momentum flux accurately. Profile parameters (x_1 to x_4) have, therefore, been defined as weighted averages over the mode amplitude

$$x_1 = \frac{\int \{|\phi(\psi)|\} \frac{R}{L_T}(\psi) d\psi}{\int \{|\phi(r)|\} d\psi} \tag{4.13}$$

$$x_2 = \frac{\int \{|\phi(\psi)|\} \frac{\partial}{\partial\psi}\frac{R}{L_T}(\psi) d\psi}{\int \{|\phi(\psi)|\} d\psi} \tag{4.14}$$

$$x_3 = \frac{\int \{|\phi(\psi)|\} \frac{R}{L_n}(\psi) d\psi}{\int \{|\phi(r)|\} d\psi} \tag{4.15}$$

$$x_4 = \frac{\int \{|\phi(\psi)|\} \frac{\partial}{\partial\psi}\frac{R}{L_n}(\psi) d\psi}{\int \{|\phi(\psi)|\} d\psi}, \tag{4.16}$$

The curly brackets denote the average over poloidal (s) direction. The coefficients

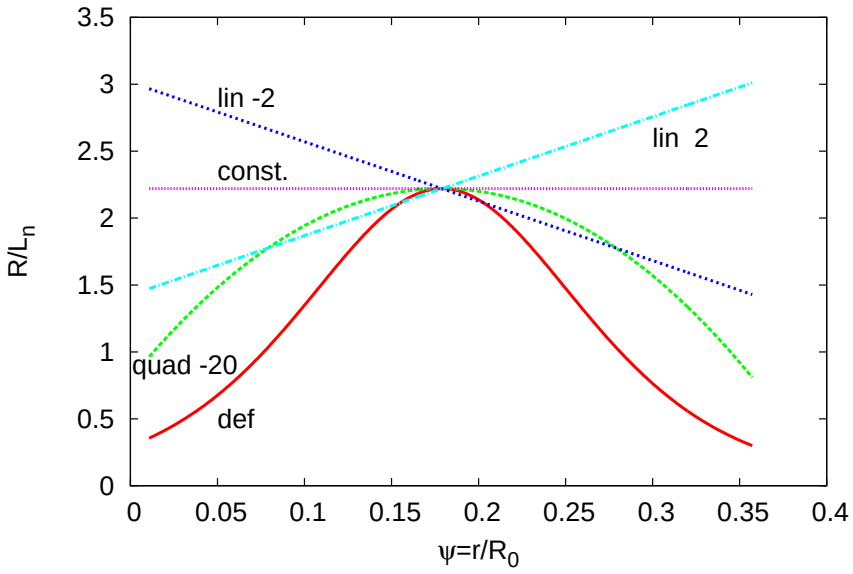

Figure 4.5: Profile shapes used in the investigation of influence of first and second derivatives on momentum transport. "def" refers to eq. (4.10).

a_m are then determined by a fit. For the profiles used here we have obtained

$$\frac{\Gamma v_{thi}}{Q} = 0.01\,(-3.9x_1 + 0.62x_2 + 2.9x_3 - 0.37x_4) \tag{4.17}$$

The data set used here is limited, and the influence of the radial variation of geometry parameters has not been investigated. Furthermore, the quality of the fit is poor, and the result above should not be considered as an accurate parametrization of the momentum flux. Nevertheless, the relative importance of first and second derivatives of the profile can be established. Although the coefficients connected with the second derivative (i.e. a_2 and a_4) are smaller than the ones connected with the first derivative (a_1 and a_3), the profiles parameters can be estimated as $x_1 \approx R/L_T$, $x_2 \approx (R/L_T)^2$, $x_3 \approx R/L_N$, and $x_4 \approx (R/L_N)^2$. It follows, that both first and second derivatives of the profile contribute to the momentum flux in roughly equal magnitude.
Finally, the ρ_* dependency has been studied in linear theory. The ratio of the momentum flux to the ion heat flux is calculated for different ρ_*, without changing density and temperature profiles as well as geometry parameters. Furthermore, a constant normalized poloidal wave vector (i.e. constant $k_\theta\rho$) was used. To satisfy the latter condition, the toroidal mode number is scaled $n \propto 1/\rho_*$, with $n = 32$ at $\rho_* = 1.8556 \cdot 10^{-3}$. Fig. 4.6 shows the ratio $\Gamma v_{thi}/Q_i$ as a function of ρ_*. In the studied case the normalized momentum flux is roughly constant, rather than decreasing with decreasing ρ_*. Although different from the predicted dependency ($\rho_*^{1/3}$) of Ref. [30] the dependence on ρ_* in linear theory is weak, in contrast with

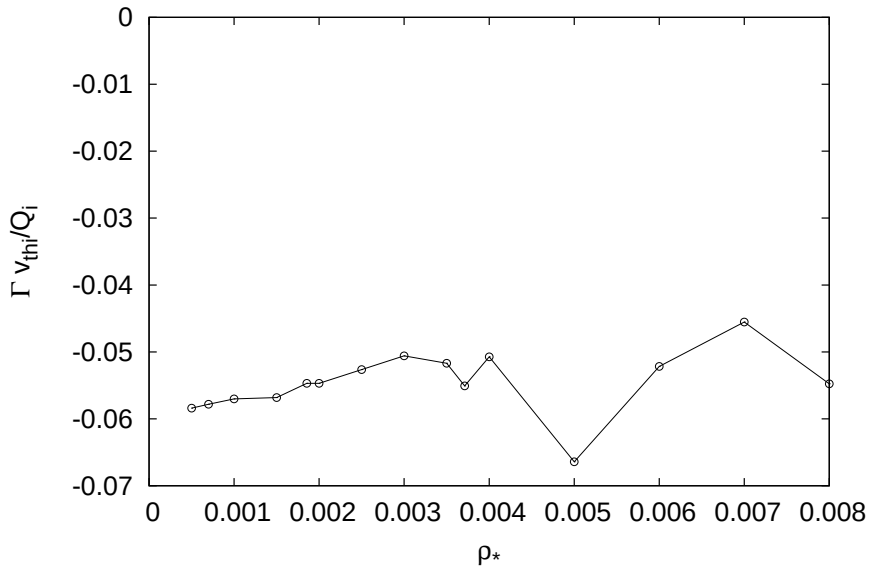

Figure 4.6: Ratio $\Gamma v_{thi}/Q_i$ obtained from linear simulations at constant $k_\theta \rho$ as a function of ρ_*. (Γ and Q_i here refer to values averaged over the flux surface.)

the ρ_* scaling argument presented in Ref. [46].

4.4 Non-linear simulations

Fig. 4.7 (top) shows the ion heat conduction coefficient $\chi_i = \langle Q_i \rangle_\psi / (R/L_T)$ as a function of normalized time ($t_N = t v_{vthi}/R_0$) for different values of the normalized Larmor radius ρ_*. It is given in gyro-Bohm unites ($\rho_i^2 v_{thi}/R_0$ with ρ_i and v_{thi} calculated at $\psi = \psi_0$), the brackets $\langle \rangle_\psi$ denote the average over the radial domain $\psi = [0.1 - 0.2]$. As the relaxation rate depends on ρ_*, it has been verified, by extending the the simulation to twice the time, that even the simulation with the smallest ρ_* value ($1 \cdot 10^{-3}$), is not far from steady state at $t = 2000R/v_{th}$. Fig. 4.8 shows the fluxes averaged over the last 800 R_0/v_{th} as a function of $\psi = r/R_0$. The radial profile of the fluxes has a bell shaped curve in agreement with the drive of the temperature gradient (e.g. Fig 4.1). The ion heat conduction coefficient is given in gyro-Bohm units, and increases with decreasing normalized Larmor radius, in disagreement with the gyro-Bohm scaling. These results are not inconsistent with previous results [86, 87, 88] in which divergence from Gyro-Bohm scaling is found at large ρ_*. When comparing the results one has to bear in mind though that the definition of ρ_* is different ($\rho_*^{GKW} = \rho_i/R_0 = (a\sqrt{2}/R_0)(\rho_s/a)$) and that, furthermore, the temperature gradient profile used here is different from the one used in some of the references.

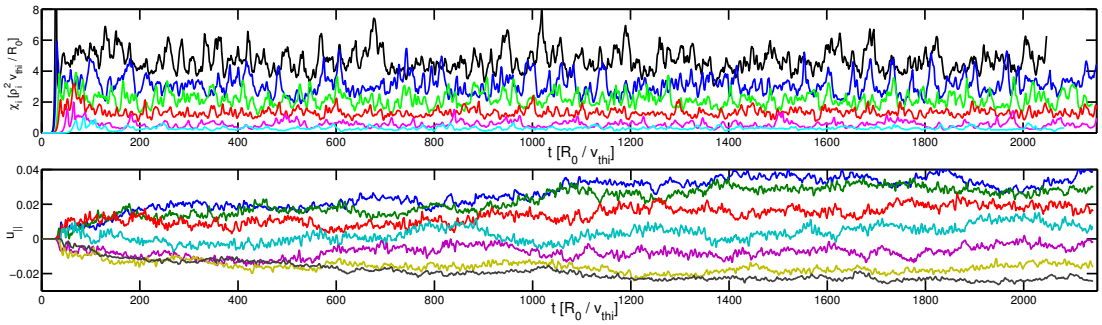

Figure 4.7: Top: Ion heat flux as a function of time for various values of ρ_*. The smaller ρ_* the higher the heat flux. The different curves are calculated, from top to bottom, for $\rho_* = 1 \cdot 10^{-3}$ (black), $2 \cdot 10^{-3}$ (blue), $3 \cdot 10^{-3}$ (green), $4 \cdot 10^{-3}$ (red), $6 \cdot 10^{-3}$ (magenta) and $8 \cdot 10^{-3}$ (cyan). Bottom: the mean parallel velocity $u_{||}$ as a function of time for $\rho_* = 3 \cdot 10^{-3}$ and different radial positions $\psi = [0.110, 0.133, 0.156, 0.180, 0.203, 0.226, 0.249]$.

The simulations are run without background rotation. Profile shear then generates a momentum flux that builds up a rotation gradient in the perturbed distribution. This process continues until the diffusive flux connected with the rotation gradient balances the flux due to profile shearing. The simulations have been run long enough for the parallel velocity profile in the confinement region to reach steady state as is shown for $\rho_* = 3 \cdot 10^{-3}$ in Fig. 4.7. Stationary profiles of the mean parallel velocity $u_{||}$ are given in Fig. 4.10. The stationary rotation gradient that is generated is then determined at the location where $u_{||}$ goes through zero (or more precisely by determining the averaged gradient in the radial domain $\psi = [0.16 - 0.23]$). At this location the influence of any Coriolis effect is minimal. Fig. 4.11 shows the equilibrium gradient as a function of ρ_*. For sufficiently small normalized Larmor radius ($\rho_* < 4 \cdot 10^{-3}$) a linear scaling of the equilibrium gradient with ρ_* is observed, in contrast with the linear theory model [30], but in agreement with the result of Ref. [80].
The difference in the ρ_* dependence between linear and non-linear theory is striking. Although quasi-linear theory is in general reasonably successful in the prediction of transport properties, it fails to predict the correct ρ_* dependence of the momentum transport due to profile shearing. One may speculate that a small radial symmetry breaking leads to a small difference in growth rate between modes that drive momentum inward compared with the modes that drive momentum outward. The linear initial value calculations presented here, then select the most unstable mode, with its according momentum flux. This calculation gives no information on possible other unstable modes that generate a momentum flux of the opposite sign, even if the growth rate of the latter modes is only slightly smaller. In non-linear simulations, on the other hand, all modes can be expected to be excited. Therefore, one can speculate that the proper ρ_* scaling may only

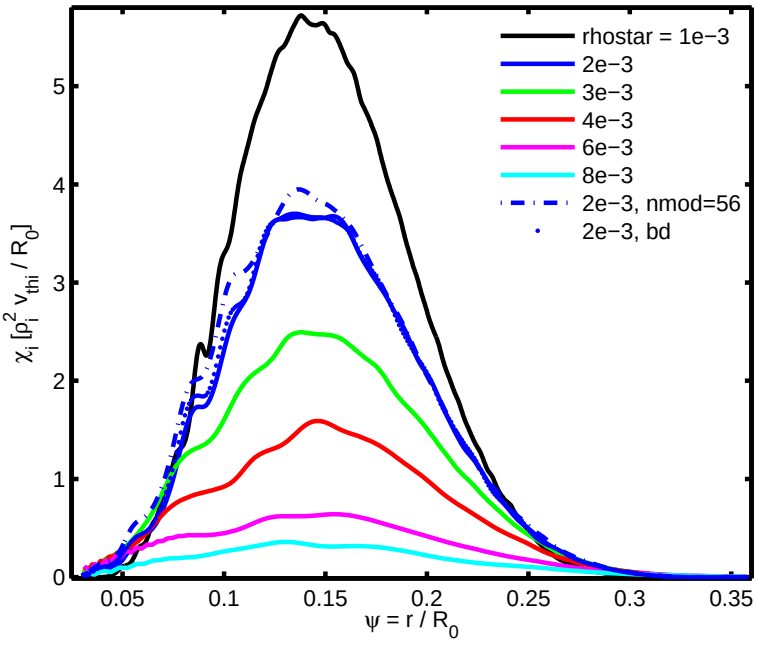

Figure 4.8: Ion heat flux averaged over time as a function of radius from non-linear simulations

be obtained if one considers a proper average over all the modes.

4.5 Conclusions

The effect of profile shearing on momentum transport has been studied in global gyrokinetic simulations. The momentum flux has contributions both due to the gradients of the profile as well as due to the second derivatives of the profile, with the fit of Eq. (4.17) indicating that first and second derivatives are equally important. In physics terms this means that not only the radial variation in the driving gradients of the mode are important, but also the radial dependence of plasma parameters play an important role. The latter effect includes, for instance, the radial dependence of the drift frequency, which can be expected to influence the frequency of the mode.
Linear simulations at a constant toroidal mode number reveal a weak dependence of momentum transport on the normalized Larmor radius, whereas non-linear simulations yield a momentum flux that is linear in the normalized Larmor radius provided the latter is sufficiently small. In nonlinear simulations a linear scaling with ρ_* is obtained for $\rho_* < 4 \cdot 10^{-3}$, i.e. many of the current experiments are in this regime. The obtained equilibrium gradients are of the same order as current

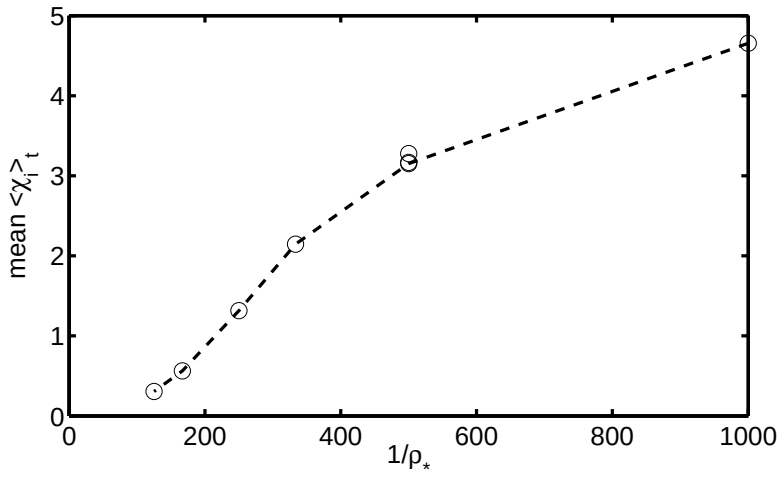

Figure 4.9: Ion heat flux as a function of $1/\rho_*$

experiments. However, due to the small ρ_* in a reactor plasma, profile shearing can be expected to generate only a small rotation. A rough estimate of the rotation that can be found in an ITER like device, can be obtained from the ρ_* scaling. Using a linear fit on the rotational gradients obtained from the nonlinear simulations (as seen in Fig. 4.11, using only the values up to $\rho_* = 4 \times 10^{-3}$) one finds

$$u'_{||} \quad = \quad -176.3 \cdot \rho_*. \tag{4.18}$$

Which makes a gradient of $u'_{||,ITER} \approx -0.1$ for the ITER value $\rho_{*,ITER} = 5.6 \times 10^{-4}$. Assuming no edge rotation and a constant rotation gradient one then obtains for the rotation in the core of ITER

$$u_{||,ic} \quad \approx \quad 0.036. \tag{4.19}$$

One should keep in mind that this is a rather rough estimate. Not only because of the model, as the simulations did not include effects that are probably important (e.g. collisions or finite β), but also because of the used assumption of a constant rotation gradient. Nevertheless, it indicates that the mechanism will not likely be important for a reactor.

4.6 Acknowledgments

A part of this work was carried out using the HELIOS supercomputer system at Computational Simulation Centre of International Fusion Energy Research Centre (IFERC-CSC), Aomori, Japan, under the Broader Approach collaboration between Euratom and Japan, implemented by Fusion for Energy and JAEA.

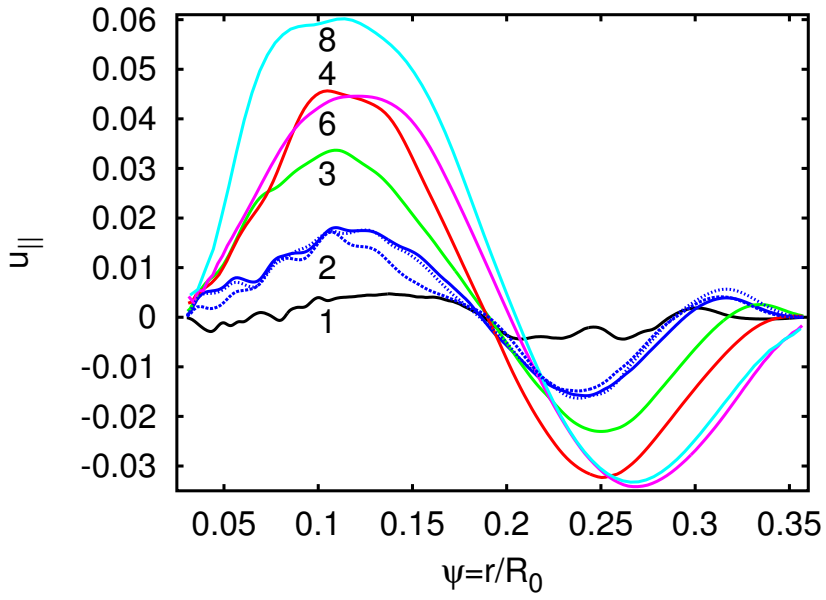

Figure 4.10: $u_{||}$ averaged over time as a function of radius. The numbers indicate the ρ_* value ($\times 10^{-3}$) for the corresponding curve.

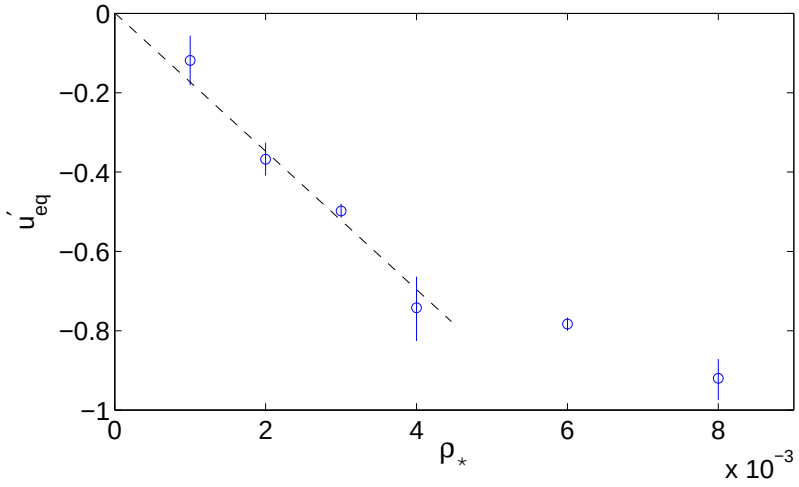

Figure 4.11: Scaling of u'_{eq} with ρ_*.

Chapter 5

Velocity nonlinearity

5.1 Motivation

As mentioned in Sec. 2.6, momentum transport in a tokamak can be related to symmetry breaking [44, 46] in the model equations. One term that breaks the symmetry (see Eq (2.104)) is the so called velocity nonlinearity. As such it can drive momentum transport and thus drive intrinsic rotation.
The neglection of the velocity nonlinearity breaks the energy conservation. Thus including the velocity nonlinearity has the additional advantage that energy is conserved in the model equations. It will be shown however, that for numerical reasons (a cancellation problem) energy conservation is hard to obtain. In the rest of this chapter details of the implementation are given, as well as first results.

5.2 Theory

As stated in chapter 2, the basic equation for the distribution function is ($d\mu/dt = 0$)

$$\frac{\mathrm{d}f}{\mathrm{d}t} = \frac{\partial f}{\partial t} + \frac{\mathrm{d}\underline{X}}{\mathrm{d}t}\frac{\partial f}{\partial \underline{X}} + \frac{\mathrm{d}v_\parallel}{\mathrm{d}t}\frac{\partial f}{\partial v_\parallel}. \tag{5.1}$$

The velocity nonlinearity is part of the third term, the acceleration. The time derivative of the parallel velocity (multiplied by $mv_\parallel$) is

$$mv_\parallel \frac{\mathrm{d}v_\parallel}{\mathrm{d}t} = -\frac{\mathrm{d}\underline{X}}{\mathrm{d}t} \cdot \left[Ze\nabla\langle\phi\rangle + \mu\nabla B + \nabla\mathcal{E}_\Omega\right], \tag{5.2}$$

with

$$\frac{\mathrm{d}\underline{X}}{\mathrm{d}t} = v_\parallel\hat{\underline{b}} + \underline{v}_\chi + \underline{v}_D. \tag{5.3}$$

The drift velocities are

$$\underline{v}_\chi = \frac{\hat{\underline{b}} \times \nabla\langle\phi\rangle}{B} \tag{5.4}$$

$$\underline{v}_D = \underbrace{\frac{mv_\parallel^2}{ZeB}\frac{\underline{B}\times\nabla B}{B^2}}_{=:v_\parallel^2 \underline{v}_{\hat{\underline{b}}\times\nabla B}} + \frac{\mu}{Ze}\frac{\underline{B}\times\nabla B}{B^2} + \underbrace{\frac{mv_\parallel^2}{2ZeB}\beta'\hat{\underline{b}}\times\nabla\psi}_{=:v_\parallel^2\hat{\underline{b}}\times\nabla\psi} + \underbrace{\frac{2mv_\parallel}{ZeB}\underline{\Omega}_\perp}_{=:v_\parallel \underline{v}_{\underline{\Omega}_\perp}} + \frac{1}{ZeB}\hat{\underline{b}}\times\nabla\mathcal{E}_\Omega. \tag{5.5}$$

Here electromagnetic effects are neglected, but centrifugal effects described by the potential

$$\mathcal{E}_\Omega = Ze\nabla\Phi - \frac{1}{2}m\Omega^2(R^2 - R_0^2) \tag{5.6}$$

are kept. The last term in Eq. (5.1) contains terms proportional to both the perturbed field ϕ and the perturbed distribution f. Usually these terms, referred to as velocity nonlinearity, are neglected in the δf formalism, as they are an order ρ_* smaller compared with the leading terms. The linear terms that are already included in GKW, will not be considered in the following derivation.
The last term from Eq. (5.1) adds a term in the form

$$\frac{\partial f}{\partial t} \stackrel{+}{=} \frac{1}{mv_\parallel}[v_\parallel\hat{\underline{b}} + \underline{v}_D + \underline{v}_\chi]\cdot[Ze\nabla\langle\phi\rangle + \mu\nabla B + \nabla\mathcal{E}_\Omega]\frac{\partial f}{\partial v_\parallel}. \tag{5.7}$$

Concentrating on the factor in front of the parallel velocity derivative

$$\begin{aligned} -mv_\parallel\frac{\mathrm{d}v_\parallel}{\mathrm{d}t} = {} & Zev_\parallel\hat{\underline{b}}\cdot\nabla\langle\phi\rangle + Ze\underline{v}_D\cdot\nabla\langle\phi\rangle + \underline{v}_\chi\cdot\mu\nabla B + \underline{v}_\chi\cdot\nabla\mathcal{E}_\Omega \\ & + \underbrace{v_\parallel\hat{\underline{b}}\cdot\mu\nabla B + v_\parallel\hat{\underline{b}}\cdot\nabla\mathcal{E}_\Omega}_{\text{linear terms already contained in GKW}} \\ & + \underline{v}_D\cdot\mu\nabla B + \underline{v}_D\cdot\nabla\mathcal{E}_\Omega \end{aligned} \tag{5.8}$$

The terms in the first row will lead to the velocity nonlinearity. The terms in the last row will lead to linear terms, which are so far not included into GKW.
Inserting the drift velocities into Eq. (5.8)

$$\begin{aligned} -mv_\parallel\frac{\mathrm{d}v_\parallel}{\mathrm{d}t} \stackrel{+}{=} {} & Zev_\parallel\hat{\underline{b}}\cdot\nabla\langle\phi\rangle + Ze\left(v_\parallel^2\underline{v}_{\hat{\underline{b}}\times\nabla B} + v_\parallel^2\underline{v}_{\hat{\underline{b}}\times\nabla\psi} + v_\parallel\underline{v}_{\underline{\Omega}_\perp}\right)\cdot\nabla\langle\phi\rangle \\ & + \left(v_\parallel^2\underline{v}_{\hat{\underline{b}}\times\nabla\psi} + v_\parallel\underline{v}_{\underline{\Omega}_\perp}\right)\cdot\mu\nabla B + \left(v_\parallel^2\underline{v}_{\hat{\underline{b}}\times\nabla B} + v_\parallel^2\underline{v}_{\hat{\underline{b}}\times\nabla\psi} + v_\parallel\underline{v}_{\underline{\Omega}_\perp}\right)\cdot\nabla\mathcal{E}_\Omega. \end{aligned} \tag{5.9}$$

Inserting this, using the geometry tensors (2.66)-(2.75) and normalizing results in

$$\begin{aligned}\frac{\partial f_N}{\partial t_N} \stackrel{+}{=} & \frac{\rho_*}{2}\frac{1}{v_{GN}}\frac{Z}{m_N}\mathcal{F}_N\frac{\partial\langle\phi_N\rangle}{\partial s}\frac{\partial f_N}{\partial v_{\parallel N}} - \frac{\rho_*}{2}m_N v_{GN}\frac{v_{\parallel N}\mu_N B_N}{Z}\beta'_N\mathcal{D}^{\psi}_N\frac{\partial f_N}{\partial v_{\parallel N}} \\ & -\rho_* s_B m_N v_{GN}\frac{4\Omega_N}{Z}\mathcal{H}^{\beta}_N\mu_N\frac{\partial B_N}{\partial x_{\beta N}}\frac{\partial f_N}{\partial v_{\parallel N}} \\ & +\frac{\rho_*}{2}\frac{1}{v_{GN}}\left(\frac{2T_{GN}}{v_{GN}}\frac{v_{\parallel N}}{Zm_N}\mathcal{D}^{\beta}_N\right. \\ & \left.+v_{GN}\frac{v_{\parallel N}}{Z}\beta'_N\mathcal{E}^{\psi\beta}_N - s_B\frac{4\Omega_N}{Z}\mathcal{H}^{\beta}_N\right)\frac{\partial\mathcal{E}_{\Omega N}}{\partial x_{\beta N}}\frac{\partial f_N}{\partial v_{\parallel N}} \\ & +\frac{\rho_*^2}{2}\left(v_{\parallel N}\mathcal{D}^{\beta}_N + v_{\parallel N}\beta'_N\mathcal{E}^{\psi\beta}_N - \frac{4s_B}{v_{GN}}\Omega_N\mathcal{H}^{\beta}_N\right)\frac{\partial\langle\phi_N\rangle}{\partial x_{\beta N}}\frac{\partial f_N}{\partial v_{\parallel N}}. \end{aligned} \tag{5.10}$$

Nonlinear in the perturbed quantities are only the first term and the terms in the last row. Note also that all the terms are formally of the same order in ρ_*.
Not all the terms break the symmetry Eq. (2.104) (see also the definition of the geometry tensors Eq. (2.66)-(2.75)). The first term of the last bracket, for example breaks the symmetry, the second not.
See Appendix A for the equations in the electromagnetic case with rotation.

5.2.1 Local limit

The equations above are derived in the global model (see Sec. 2.7), while in this chapter the momentum transport due to the velocity nonlinearity is studied using the local limit flux tube approximation. This approximation affects the form in which the velocity nonlinearity must be implemented, as shown below. In essence care must be taken to ensure particle number conservation. This requires

$$0 = \int d^5\underline{x} J_v \frac{\partial f}{\partial t} \tag{5.11}$$

$$= \int d^5\underline{x} J_v \frac{\mathrm{d}\underline{X}}{\mathrm{d}t}\cdot\nabla f + \int d^5\underline{x} J_v \frac{\mathrm{d}v_\parallel}{\mathrm{d}t}\frac{\partial f}{\partial v_\parallel}, \tag{5.12}$$

where J_v is the velocity space Jacobian and $\int d^5\underline{x}$ represents an integration over the five dimensional phase space. Using the relation

$$0 = \frac{1}{J_v}\frac{\partial J_v}{\partial t} + \frac{1}{J_v}\nabla\cdot\left[J_v\frac{\mathrm{d}\underline{X}}{\mathrm{d}t}\right] + \frac{1}{J_v}\frac{\partial}{\partial v_\parallel}\left[J_v\frac{\mathrm{d}v_\parallel}{\mathrm{d}t}\right]. \tag{5.13}$$

density conservation can be derived. However, the local limit implies approximations in $d\underline{X}/dt$ and therefore, particle conservation can be violated. Since $J_v \propto B$ and since for the local limit it can be shown that

$$0 = \frac{1}{B}\nabla\cdot\left[J_v\frac{\mathrm{d}\underline{X}}{\mathrm{d}t}\right] \tag{5.14}$$

it follows that for the local limit

$$\int d^5\underline{x} J_v \frac{\mathrm{d}\underline{X}}{\mathrm{d}t} \cdot \nabla f \;=\; \int d^5\underline{x} \nabla \cdot \left[J_v \frac{\mathrm{d}\underline{X}}{\mathrm{d}t} f \right] = 0. \tag{5.15}$$

Therefore, the following condition must apply

$$0 \;=\; \int d^5\underline{x} J_v \frac{\mathrm{d}v_\parallel}{\mathrm{d}t} \frac{\partial f}{\partial v_\parallel}, \tag{5.16}$$

which can be achieved by not implementing the velocity nonlinearity as

$$\frac{\partial f}{\partial v_\parallel} \;\stackrel{+}{=}\; \frac{\mathrm{d}v_\parallel}{\mathrm{d}t} \frac{\partial f}{\partial v_\parallel}, \tag{5.17}$$

but rather as

$$\frac{\partial f}{\partial v_\parallel} \;\stackrel{+}{=}\; \frac{\partial}{\partial v_\parallel} \left[\frac{\mathrm{d}v_\parallel}{\mathrm{d}t} f \right]. \tag{5.18}$$

Compared with the equations in the previous section this leads to additional terms

$$\begin{aligned} \frac{\partial f_N}{\partial t_N} \;\stackrel{+}{=}\; & \frac{\rho_*^2}{2} \left(\mathcal{D}_N^\beta \frac{\partial \langle \phi_N \rangle}{\partial x_{N\beta}} + \mathcal{D}_N^\beta \frac{\partial \Phi_N}{\partial x_{N\beta}} + \beta'_N \mathcal{E}_N^{\psi\beta} \frac{\partial \langle \phi_N \rangle}{\partial x_{N\beta}} + \beta'_N \mathcal{E}_N^{\psi\beta} \frac{\partial \Phi_N}{\partial x_{N\beta}} \right) f_N \\ & + \rho_* \left(-m_N v_{NG}^2 \frac{\mu_N B_N}{2Z} \beta'_N \mathcal{D}_N^\psi - \frac{m_N}{2Z} \mathcal{D}_N^\beta \Omega_N^2 \frac{\partial R_N^2}{\partial x_{N\beta}} + \frac{m_N}{2Z} \mathcal{D}_N^\beta \Omega_N^2 \frac{\partial R_{N0}^2}{\partial x_{N\beta}} \right. \\ & \left. - \frac{s_B}{2Z} \beta'_N m_N \Omega_N^2 \mathcal{I}_N^\psi + \frac{m_N}{2Z} \beta'_N \mathcal{E}_N^{\psi\beta} \Omega_N^2 \frac{\partial R_{N0}^2}{\partial x_{N\beta}} \right) f_N. \end{aligned} \tag{5.19}$$

5.3 Energy conservation

Energy conservation is an important concept in numerical simulations. This chapter will thus prove that the equations that have been derived and implemented in GKW do conserve energy in the electrostatic case without rotation. This can also be seen as a check if the derivation of the additional terms is correct.

As reminder

$$\frac{\mathrm{d}\underline{X}}{\mathrm{d}t} \;=\; v_\parallel \hat{\underline{b}} + \underline{v}_\chi + \underline{v}_D \tag{5.20}$$

$$m v_\parallel \frac{\mathrm{d}v_\parallel}{\mathrm{d}t} \;=\; -\frac{\mathrm{d}\underline{X}}{\mathrm{d}t} \cdot (Ze\nabla\langle\phi\rangle + \mu\nabla B) \tag{5.21}$$

Starting point is the equation solved in GKW

$$\begin{aligned} 0 &= \frac{\partial f}{\partial t} + (v_\parallel \hat{\underline{b}} + \underline{v}_D + \underline{v}_\chi)\cdot\nabla f - \frac{\hat{\underline{b}}}{m}\cdot\mu\nabla B\frac{\partial f}{\partial v_\parallel} \\ &\quad -\frac{Ze}{mv_\parallel}v_\parallel\hat{\underline{b}}\cdot\nabla\langle\phi\rangle\frac{\partial f}{\partial v_\parallel} - \frac{Ze}{mv_\parallel}\underline{v}_{D-}\cdot\nabla\langle\phi\rangle\frac{\partial f}{\partial v_\parallel} \\ &\quad +\underline{v}_\chi\cdot\nabla F_M + \underline{v}_D\cdot\nabla F_M + \frac{Ze}{T}v_\parallel\hat{\underline{b}}\cdot\nabla\langle\phi\rangle F_M \\ &\quad +\frac{1}{T}\underline{v}_\chi\cdot(\mu\nabla B)F_M + \frac{Ze}{T}\underline{v}_D\cdot\nabla\langle\phi\rangle F_M. \end{aligned} \tag{5.22}$$

Note that it might seem at first, that the term proportional to $\underline{v}_\chi\cdot(\nabla B)F_M$ is missing in GKW, but this is not the case. This term cancels with the term proportional to ∇B from $\underline{v}_\chi\cdot\nabla F_M$. These are included here to make the derivation below more explicit.
It can be shown that

$$-\frac{\hat{\underline{b}}}{m}\cdot\mu\nabla B\frac{\partial f}{\partial v_\parallel} - \frac{Ze}{mv_\parallel}v_\parallel\hat{\underline{b}}\cdot\nabla\langle\phi\rangle\frac{\partial f}{\partial v_\parallel} - \frac{Ze}{mv_\parallel}\underline{v}_{D-}\cdot\nabla\langle\phi\rangle\frac{\partial f}{\partial v_\parallel} = \frac{\mathrm{d}v_\parallel}{\mathrm{d}t}\frac{\partial f}{\partial v_\parallel} \tag{5.23}$$

For the Maxwell background using

$$0 = v_\parallel\hat{\underline{b}}\cdot\nabla F_M - \frac{1}{m}\hat{\underline{b}}\cdot\mu\nabla B\frac{\partial F_M}{\partial v_\parallel} \tag{5.24}$$

$$0 = \frac{\partial F_M}{\partial t} \tag{5.25}$$

one can show

$$\begin{aligned} &\underline{v}_\chi\cdot\nabla F_M + \underline{v}_D\cdot\nabla F_M \\ &+\frac{Ze}{T}v_\parallel\hat{\underline{b}}\cdot\nabla\langle\phi\rangle F_M + \frac{Ze}{T}\underline{v}_D\cdot\nabla\langle\phi\rangle F_M - \frac{1}{mv_\parallel}\underline{v}_\chi\cdot\mu\nabla B\frac{\partial F_M}{\partial v_\parallel} \\ =\ &\frac{\mathrm{d}\underline{X}}{\mathrm{d}t}\cdot\nabla F_M + \frac{\mathrm{d}v_\parallel}{\mathrm{d}t}\frac{\partial F_M}{\partial v_\parallel}. \end{aligned} \tag{5.26}$$

Therefore, the equation for the evolution of the distribution can be written in the form

$$0 = \frac{\partial}{\partial t}(f+F_M) + \frac{\mathrm{d}\underline{X}}{\mathrm{d}t}\cdot\nabla(f+F_M) + \frac{\mathrm{d}v_\parallel}{\mathrm{d}t}\frac{\partial}{\partial v_\parallel}(f+F_M), \tag{5.27}$$

which is the equation for the full distribution $F = f + F_M$. This result is not surprising as the step above are reverting the steps done in the δf approximation. The equation

$$\frac{1}{J_v}\frac{\partial J_v}{\partial t} + \frac{1}{J_v}\nabla\cdot\left[J_v\frac{\mathrm{d}\underline{X}}{\mathrm{d}t}\right] + \frac{1}{J_v}\frac{\partial}{\partial v_\parallel}\left[J_v\frac{\mathrm{d}v_\parallel}{\mathrm{d}t}\right] = 0 \tag{5.28}$$

can be used to write the evolution equation in conservative form

$$\frac{\partial f + F_M}{\partial t} + \frac{1}{J_v}\nabla \cdot \left[J_v \frac{\mathrm{d}\underline{X}}{\mathrm{d}t}(f + F_M) \right] + \frac{1}{J_v}\frac{\partial}{\partial v_\parallel}\left[J_v \frac{\mathrm{d}v_\parallel}{\mathrm{d}t}(f + F_M) \right] = 0 \quad (5.29)$$

The Jacobian of the velocity integration (J_v) used in the model equations is time independent. Using this, and Eq. (5.21) to get

$$\begin{aligned} \frac{\partial E_{kin}}{\partial t} &= \frac{\partial}{\partial t}\int d^3\underline{X}\int d^3\underline{v}\left(\frac{1}{2}mv_\parallel^2 + \mu B\right) f \quad (5.30) \\ &= -\sum_{sp}\int d^3\underline{X}\int d^3\underline{v}\frac{\mathrm{d}\underline{X}}{\mathrm{d}t} Ze\nabla\langle\phi\rangle(f + F_M) \end{aligned}$$

for the time derivative of the kinetic energy. The term on the right hand side is the current in the electric field, which is the energy transfer to the electromagnetic field.

The equation for the field energy can be derived from the Poisson equation

$$\sum_{sp} Z_{sp}e\int d^3\underline{v}\langle f\rangle^\dagger = \sum_{sp}\frac{Z_{sp}^2e^2}{T_{sp}}\int d^3\underline{v}\left[\phi - \langle\langle\phi\rangle\rangle^\dagger\right] F_M. \quad (5.31)$$

Take the time derivative

$$\sum_{sp} Z_{sp}e\int d^3\underline{v}\frac{\partial\langle f\rangle^\dagger}{\partial t} = \sum_{sp}\frac{Z_{sp}^2e^2}{T_{sp}}\int d^3\underline{v}\left[\frac{\partial\phi}{\partial t} - \frac{\partial\langle\langle\phi\rangle\rangle^\dagger}{\partial t}\right] F_M, \quad (5.32)$$

multiply with the perturbed potential ϕ and integrate over space to obtain

$$\sum_{sp} Z_{sp}e\int d^3\underline{X}\int d^3\underline{v}\langle\phi\rangle\frac{\partial f}{\partial t} = \frac{\partial}{\partial t}\sum_{sp}\frac{Z_{sp}^2e^2}{2T_{sp}}\int d^3\underline{X}\int d^3\underline{v}\left[\phi^2 - \langle\phi\rangle^2\right] F_M \quad (5.33)$$

The sum on the right hand side is the electrostatic field energy. The time derivative of the field energy is thus

$$\frac{\partial E_{field}}{\partial t} = \sum_{sp} Z_{sp}e\int d^3\underline{X}\int d^3\underline{v}\langle\phi\rangle\frac{\partial}{\partial t}(f + F_M) \quad (5.34)$$

and inserting the time derivative of the distribution function leads to

$$\frac{\partial E_{field}}{\partial t} = \sum_{sp} Z_{sp}e\int d^3\underline{X}\int d^3\underline{v}\nabla\langle\phi\rangle\cdot\frac{\mathrm{d}\underline{X}}{\mathrm{d}t}(f + F_M). \quad (5.35)$$

The time derivative of field plus kinetic energy is

$$\begin{aligned} \frac{\partial E_{field}}{\partial t} + \frac{\partial E_{kin}}{\partial t} &= +\sum_{sp} Z_{sp}e\int d^3\underline{X}\int d^3\underline{v}\nabla\langle\phi\rangle\cdot\frac{\mathrm{d}\underline{X}}{\mathrm{d}t}(f + F_M) \\ &\quad -\sum_{sp}\int d^3\underline{X}\int d^3\underline{v}\frac{\mathrm{d}\underline{X}}{\mathrm{d}t} Ze\nabla\langle\phi\rangle(f + F_M) \quad (5.36) \\ &= 0, \quad (5.37) \end{aligned}$$

i.e. the energy is conserved.

5.4 Momentum transport generated by the velocity nonlinearity

The velocity nonlinearity breaks the symmetry transformation given in Eq. (2.104). As this is only a sufficient condition for momentum transport, it has to be checked if the velocity nonlinearity does drive a momentum flux. This is done in this section using numerical simulations.
For the numerical simulations the parameters of the Waltz standard case have been used. The geometry parameters where: inverse aspect ratio $\epsilon = 0.16667$, safety factor $q = 2.0$ and shear $\hat{s} = 1.0$. The simulation was electrostatic with kinetic electrons and with $m_i/m_e \approx 3600$. Density gradient length ($R/L_n = 3.0$) and temperature gradient length ($R/L_T = 9.0$) where the same for electrons and ions. Rotation and collisions have been neglected. The time step was $\Delta t = 1{\cdot}10^{-3}$. The simulation grid consisted of $N_x = 160$ points in radial direction, $N_s = 16$ points in parallel direction, $N_\mu = 8$ points for the magnetic moment and $N_{v_\parallel} = 16$ for the parallel velocity. The number of toroidal modes has been set to $N_{mode} = 21$ with $k_{\theta max}\rho = 1.41$. The radial direction has been treated non-spectral with a box size of $l_x/R_{ref} = 85\rho_*$.
Figure 5.1 compares the results for the ion heat flux of a simulation with (green) and without (black) the velocity nonlinearity. The averaged (over the time

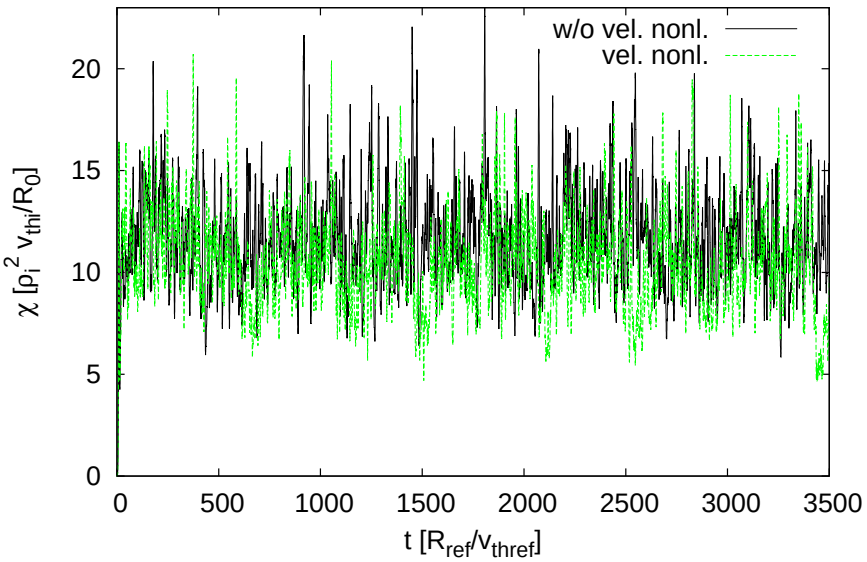

Figure 5.1: The ion heat flux over time with and without velocity nonlinearity.

interval from $1000R_{ref}/v_{thref}$ to $3500R_{ref}/v_{thref}$) ion heat flux decreases from $(11.7 \pm 0.2)\rho_i^2 v_{thi}/R_0$ without velocity nonlinearity to $(10.3 \pm 0.2)\rho_i^2 v_{thi}/R_0$ with

velocity nonlinearity, thus by about 10%. The value without velocity nonlinearity agrees with the value of $11.6 \pm 2\rho_i^2 v_{thi}/R_0$ obtained by GYRO [89]. The effect of the velocity nonlinearity found here is bigger than those found by Candy et. al. [90] who did not find a measurable effect at the GA standard parameters, using ρ_* in the range $[3.5 \cdot 10^{-4}, 5.7 \cdot 10^{-3}]$. The difference might be due to the different treatment of the electrons. While we used kinetic electrons, Candy et. al. used adiabatic electrons. Lin et. al. [91] found a decrease in the heat flux for standard Cyclone parameters and $\rho_* = 3.8 \cdot 10^{-3}$ (converted GKW units), but also with adiabatic electrons. The heat flux decreased from $\approx 0.5\rho_i^2 v_{thi}/R_0$ without, to $\approx 0.25\rho_i^2 v_{thi}/R_0$ with velocity nonlinearity.
The result for the momentum flux is shown in Fig. 5.2. Here the mean changes

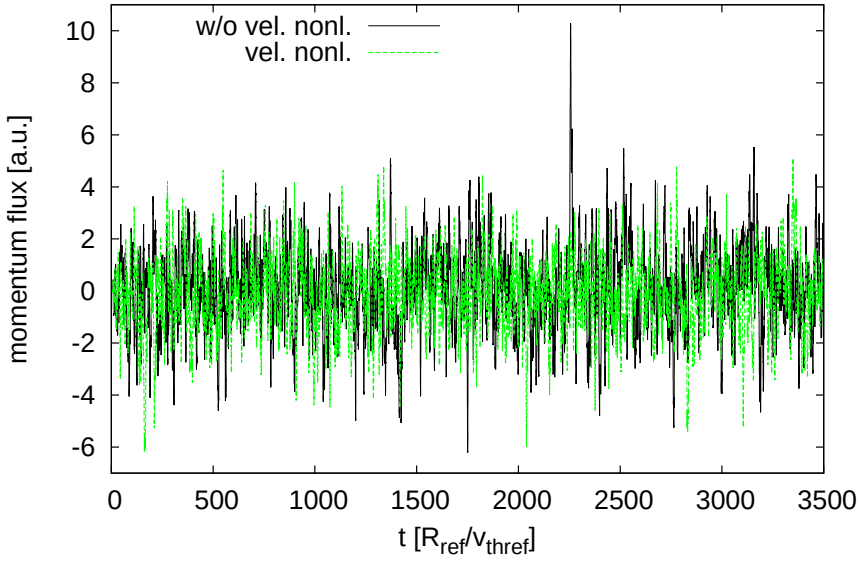

Figure 5.2: The momentum flux over time with and without velocity nonlinearity.

from $\langle \Pi_s^\psi \rangle_t / \langle Q_s^\psi \rangle_t = (1 \pm 1) \cdot 10^{-3}$ without velocity nonlinearity, to $\langle \Pi_s^\psi \rangle_t / \langle Q_s^\psi \rangle_t = (-1 \pm 1) \cdot 10^{-3}$ with velocity nonlinearity. Thus a momentum flux is found that is zero within the error bars. This is expected for the case without velocity nonlinearity.
A simulation (with velocity nonlinearity) with twice the number of points for μ and $v_\parallel$ has been done to verify, that the result is not due to poor resolution of the velocity space. The simulation is run for a smaller time interval (up to $935 R_{ref}/v_{thref}$) due to the increased computation cost. Averaging from $500 R_{ref}/v_{thref}$ to $935 R_{ref}/v_{thref}$ results in $(11 \pm 1)\rho_i^2 v_{thi}/R_0$ for the heat flux and $\langle \Pi_s^\psi \rangle_t / \langle Q_s^\psi \rangle_t = (-4 \pm 3) \cdot 10^{-4}$ for the momentum flux. Both values are, within the error bars, equal to the values gained from the simulations with smaller resolution, thus indicating that the resolution was sufficient.

To conclude, no effect of the velocity nonlinearity on the momentum flux could be found. There might still be interactions with other effects, e.g. rotation or collisions, but so far there is no hint for this. Therefore it can be argued that the velocity nonlinearity is negligible for momentum transport.

5.5 Energy conservation in simulations

In Sec. 5.3 the energy conservation for GKW has been derived. This section discusses the energy conservation in the simulations shown in the previous section. Energy conservation could not be achieved. The kinetic energy is about three orders of magnitude larger than the field energy. A simulation with twice the velocity space resolution improves the ratio of the terms, but only by a factor of about two, Mostly due to a decrease of the kinetic energy.
The result is less surprising ats it may seem at first. Since $f \propto \rho_*$ and $\phi \propto \rho_*$, the ordering of the energies is $E_{kin} \propto \rho_*$ and $E_{field} \propto \rho_*^2$. Therefore, the energy balance demands that the leading term of the kinetic energy integrates to zero. Small deviations of the leading term from the exact solution are sufficient to destroy the energy balance. The most probable source for such a deviation is the dissipation that is implemented in eulerian codes to obtain numerical stable simulations. GKW has dissipation implemented for the different directions (space and parallel velocity). While the dissipation in the parallel velocity direction does not break energy conservation, this does not hold for the dissipation in space. For example, the dissipation in the parallel (s) direction changes the total energy according to

$$\frac{\partial E_{tot}}{\partial t} \stackrel{+}{=} \sum_{sp} \int d^3\underline{X} \int d^3\underline{v} \left(\frac{1}{2} m v_\parallel^2 + \mu B + Ze\langle\phi\rangle \right) D_s (\Delta s)^3 v_\parallel \frac{\partial^4 f}{\partial s^4} \quad (5.38)$$

$$\stackrel{+}{=} \sum_{sp} \int d^3\underline{X} \int d^3\underline{v} \left(\mu B + Ze\langle\phi\rangle \right) D_s (\Delta s)^3 v_\parallel \frac{\partial^4 f}{\partial s^4}, \quad (5.39)$$

this will in general be nonzero. The use of $D_s(\Delta s)^3$ in the equation is a choice made, to have D_s of order one.

Chapter 6

Influence of centrifugal effects on particle and momentum transport in NSTX

This chapter has been published as a paper [92].

6.1 Introduction

Flow shear in tokamaks has been predicted to contribute to a number of effects in turbulent transport. For example, sheared perpendicular $E \times B$ flows can suppress turbulence [77], while sheared parallel flow can drive diffusive momentum transport [74] and destabilize Kelvin-Helmholtz instabilities [93]. Work in recent years has demonstrated that toroidal rotation (in absence of shear) can also have significant influence on particle, heat and momentum transport from microturbulence due to many physical mechanisms. For example, finite toroidal flow allows for a momentum pinch through the Coriolis effect [25], which can also influence particle and impurity transport through roto-diffusion (a flux proportional to the gradient of the rotation velocity) [83, 94]. For increasingly large Mach numbers, centrifugal effects influence momentum and impurity transport and growth rates of the underlying instabilities. This occurs due to changes in both perpendicular particle drifts as well as particle trapping through the variation of the equilibrium potential around a flux surface [67, 94]. Heavier impurities are expected to be more influenced due to their higher mass, smaller thermal velocities, and correspondingly higher Mach number. Furthermore, it was found that effects due to rotation can depend not just on toroidal flow, but also on the product of toroidal flow and flow shear [94].
In this chapter, we investigate the influence of centrifugal effects on particle and momentum transport in National Spherical Torus Experiment (NSTX) [20] H-

mode plasmas. As a spherical tokamak (ST) [95, 96], NSTX provides an unique test of microstability theory as it operates at lower aspect ratio ($R/a \sim 1.5$) and relatively large beta

$$\beta_{ref} = \frac{2\mu_0 n_{ref} T_{ref}}{B_{ref}^2}, \tag{6.1}$$

compared to conventional aspect ratio tokamaks. Because of the reduced aspect ratio and corresponding lower moment of inertia, STs can rotate rapidly due to the momentum injected via neutral beam heating. Furthermore, due to the high beta, strong surface shaping, and large perpendicular $E \times B$ flow shear, electrostatic microinstabilities, such as ion temperature gradient (ITG) and the trapped electron mode (TEM), are often predicted to be suppressed [97] or stable entirely (in the absence of $E \times B$ shear) so that other instabilities must be considered [98]. The fact that ion thermal transport in H-modes is typically found to be close to neoclassical predictions is consistent with this interpretation.
Fig. 6.1 shows the normalized toroidal rotation ($Mach = u = R\Omega/c_s$, here $c_s = \sqrt{T_{ref}/m_{ref}}$) and toroidal rotation shear ($u' = -R^2\nabla\Omega/c_s$) for various NSTX H-modes at three radii (r/a=0.6,0.7,0.8).

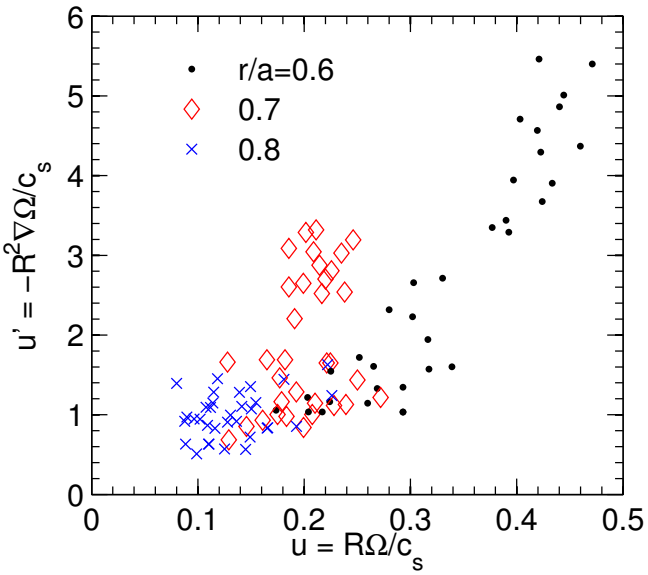

Figure 6.1: Plot of rotational gradient vs. rotation velocity of different shots of NSTX, at three different radial positions (GYRO units). A trend to higher rotation velocities closer to the axis is also observable. Figure courtesy of W. Guttenfelder.

As expected, towards the core the rotation velocities are usually higher, and there is a significant variation in the rotation velocity at $r/a = 0.7$ depending on the plasma parameters. In the region of interest ($r/a = 0.6 - 0.8$) the Mach number

of deuterium is significantly below one but, of course, the Mach number of the impurity species is larger compared to that of deuterium ($M_Z = M_D\sqrt{m_Z/m_D}$). For comparison, results for the rotation velocity and gradients of AUG H-modes have been presented in Ref. [99]. They found values of u_B up to 0.5 and u'_B up to 1.9 for boron (values are scaled to the units used in Fig. 6.1 and to deuterium) at $r/a = 0.5$.

The present study is motivated by recent observations of impurity transport in NSTX H-modes [100]. In earlier experiments, impurity transport in NSTX was found to be described by neoclassical theory, especially for perturbative measurements using injected trace impurities such as neon [101, 102, 103]. This was also found to be the case for the intrinsic carbon impurity (NSTX walls were covered with graphite tiles) in ELMy H-modes. The fact that impurity transport seems to be governed by neoclassical theory suggests turbulence is too weak to contribute, which is consistent with the ion thermal transport also being close to neoclassical predictions.

However, in discharges where lithium has been applied to the divertor region, confinement improves with an increase in temperature, and the structure of the H-mode pedestal changes in a way that the discharges become ELM-free [104]. As a result, carbon begins to accumulate, leading to plasmas with $Z_{eff} = 2-4$. However, detailed analysis shows that the carbon profiles in these ELM-free discharges are inconsistent with neoclassical theory outside the mid-radius ($r/a > 0.6$) [100]. In particular, neoclassical theory predicts there should be a strong pinch (and therefore peaked carbon profile, or $R/L_{n,c} > 0$ where $R/L_n = -R/n\nabla n$) at $r/a = 0.7$ while experimentally a hollow profile is measured ($R/L_{n,c} < 0$). In addition, the ion thermal transport in these lithiated, high temperature (lower collisionality) plasmas appears to begin departing from neoclassical predictions [105]. It is therefore of interest to investigate the microstability properties of these plasmas and the corresponding predicted impurity transport.

Linear gyrokinetic analysis for similar lithiated discharges at low collisionality find that in this radial region the microtearing mode (MTM) and kinetic ballooning mode (KBM) are the only unstable instabilities [105, 98]. It is important to note that these instabilities are fundamentally electromagnetic in nature, both depending on shear magnetic perturbations, while the KBM for these high beta conditions also depends on compressional magnetic perturbations. Linear and nonlinear simulations of the MTM predict that it only transports electron heat flux and its contributions to particle and momentum fluxes are negligible [106, 107, 108, 109]. Therefore we focus on linear analysis of the KBM and corresponding quasilinear predictions of the particle transport, assuming it influences transport even in the presence of a stronger microtearing instability. Nonlinear simulations have been left for future investigations.

The structure of this chapter is as follows. In Sec. 6.2 the parameters for the simulations are given. The results of a benchmark between GKW and GYRO will be presented in the following section. The nature of the unstable modes present

in the simulations is discussed in Sec. 6.3, followed by the results for the particle and momentum transport in Sec. 6.4 and 6.5, respectively. The conclusions are then drawn in Sec. 6.6.

6.2 Numerical setup & benchmark

A short overview of the simulation setup (parameters and grid size) is given below. Two different NSTX shots have been considered, shot number 129064 and 129061. The shots are lithium-conditioned, edge localized mode (ELM)-free, H-mode discharges with NBI (neutral beam injection)-heating. The former has been used for a benchmark between the two gyrokinetic codes GYRO [110] and GKW [21], while the second has been used in the investigation of the effects of plasma rotation. Tab. 6.1 lists the base simulation parameters for the two cases, and Tab. 6.2 and 6.3 the species parameters. Two different cases have been used for the benchmark. The first considers only electrostatic effects and no collisions, while the second includes collisions as well as electromagnetic effects. Due to the different definitions of the wave vector $k_\theta\rho$ in GKW

$$\begin{aligned} (k_\theta\rho_{ref})^2 &= g^{\zeta\zeta}k_\zeta^2 \qquad (6.2)\\ g^{\zeta\zeta} &= \left(\frac{\partial\zeta}{\partial r}\right)^2 g^{rr} + \left(\frac{\partial\zeta}{\partial\theta}\right)^2 g^{\theta\theta} \\ &\quad +2\frac{\partial\zeta}{\partial r}\frac{\partial\zeta}{\partial\theta}g^{r\theta} + \frac{1}{4\pi^2}g^{\phi\phi} \qquad (6.3)\end{aligned}$$

($\rho_{ref} = m_{ref}v_{thref}/eB_{ref}$ and g is the metric tensor) and GYRO, a conversion is necessary. The conversion factor is

$$\frac{(k_\theta\rho_{s,unit})_{gyro}}{(k_\theta\rho_{ref})_{gkw}} = \frac{\sqrt{2}\mathcal{E}^{\psi\zeta}}{s_j\sqrt{g^{\zeta\zeta}}}, \qquad (6.4)$$

with $s_j = \mathrm{sign}(\underline{j}\cdot\nabla\phi)$ and with the tensor element $\mathcal{E}^{\psi\zeta} = \frac{s_j}{4\pi}\frac{\partial\psi}{\partial\Psi}$ (Ψ is the normalized poloidal flux).
The results of the comparison can be seen in Fig. 6.2 (this as well as the following figures use values normalized as in GKW). The agreement between the two codes is good, in the simplified as well as in the elaborate case. In the simplified version an ITG mode is found. The second benchmark has a MTM at small $k_\theta\rho$, while at higher wave numbers there is a KBM. For the KBM there are some small differences in growth rate. However, for the critical wave-number $k_\theta\rho$ where the transition between dominant mode occurs, agreement between the two codes is achieved.

Table 6.1: Base parameters for the simulations.

property	#129064	#129061
$t_{\text{shot}}(s)$		0.45
ϵ	0.436	0.434
r/a	0.7	0.7
q	3.50	3.49
$\hat{s}$	1.45	1.47
κ	2.26	2.27
δ	0.249	0.250
ζ	-0.0170	-0.0160
R_{mil}	1.0	1.0
Z_{mil}	-0.0175	-0.0178
$d\kappa/d\psi$	0.0122	0.0152
$d\delta/d\psi$	0.330	0.323
$d\zeta/d\psi$	0.128	0.107
$dR_{\text{mil}}/d\psi$	-0.358	-0.360
$dZ_{\text{mil}}/d\psi$	-0.0286	-0.0408
$B_{ref}(T)$	1.150	1.150
β_{ref}	7.13e-2	7.39e-2
β'_{ref}	-9.95e-1	-6.22e-1
$R_{\text{ref}}(m)$	0.950	0.948
$T_{\text{ref}} = T_e(keV)$	0.704	0.634
$n_{\text{ref}} = n_e(10^{19}m^{-3})$	3.87	4.52
$Z_{\text{eff}}(1)$	1.0	1.0
u	0.0	0.136
u'	0.0	0.910

Table 6.2: Species parameters of shot 129064. Note that these are rounded values and small adjustments for density and density gradient length might be necessary for quasi-neutrality.

property	deuterium	carbon	electrons
$m_{\text{i}}/m_{\text{ref}}$	1.0	5.97	2.72e-4
Z_{i}	1	6	-1
$T_{\text{i}}/T_{\text{ref}}$	0.985	0.985	1.0
$n_{\text{i}}/n_{\text{ref}}$	0.494	0.0843	1.0
R/L_{T}	3.47	3.47	5.78
R/L_{n}	7.52	-2.00	2.70

Table 6.3: Species parameters of shot 129061. Note that these are rounded values and small adjustments for density and density gradient length might be necessary for quasi-neutrality.

property	deuterium	carbon	electrons	tungsten
$m_\mathrm{i}/m_\mathrm{ref}$	1.0	5.97	2.72e-4	91.3
Z_i	1	6	-1	39
$T_\mathrm{i}/T_\mathrm{ref}$	0.859	0.859	1.0	0.859
$n_\mathrm{i}/n_\mathrm{ref}$	0.511	0.0814	1.0	0.0
R/L_T	4.04	4.04	4.33	4.04
R/L_n	4.22	-3.54	0.426	0.0

The various geometry parameters in Tab. 6.1 refer to the Miller geometry [38], which has been chosen as a trade-off between effort and accuracy. In Miller geometry the cross section is described by

$$R = R_{mil} + \psi \cos(\theta + \arcsin \delta \sin \theta) \tag{6.5}$$

$$Z = Z_{mil} + \psi \kappa \sin(\theta + \zeta \sin 2\theta), \tag{6.6}$$

Z_{mil} and R_{mil} are offsets of the centre of the surface, with respect to the magnetic axis and normalized to R_{ref}. The parameters κ, *delta* and ζ describe the elongation, triangularity and squareness of the surface, respectively. Note that the radial coordinate, ψ, in GKW is scaled with the reference radius

$$\psi = \frac{r}{R_{ref}}. \tag{6.7}$$

Electro-magnetic effects, including the effect of compressibility, as well as collisions (pitch angle scattering only) have been taken into account. The β value has already been defined in Eq. (6.1). Its derivative is defined as

$$\beta'_{ref} = -\beta_{ref} \sum_s n_{N,s} T_{N,s} \left(\frac{R}{L_{n_s}} + \frac{R}{L_{T_s}} \right) \tag{6.8}$$

(sum over species, n_N/T_N is normalized to reference density/temperature) and the reference collision frequency is

$$\nu_{ref} = 6.5141 \cdot 10^{-5} R_{ref} n_{ref}^{19} \frac{\ln \Lambda^{i/i}}{T_{ref}^2}. \tag{6.9}$$

The gyrokinetic equations, formulated in a rotating frame, used by GKW can be found in Ref. [21, 25], the changes to include rotational effects have been described in [94]. The rotation velocity is defined by

$$u = \frac{R_{ref} \Omega_\phi}{v_{thref}} = \Omega_N, \tag{6.10}$$

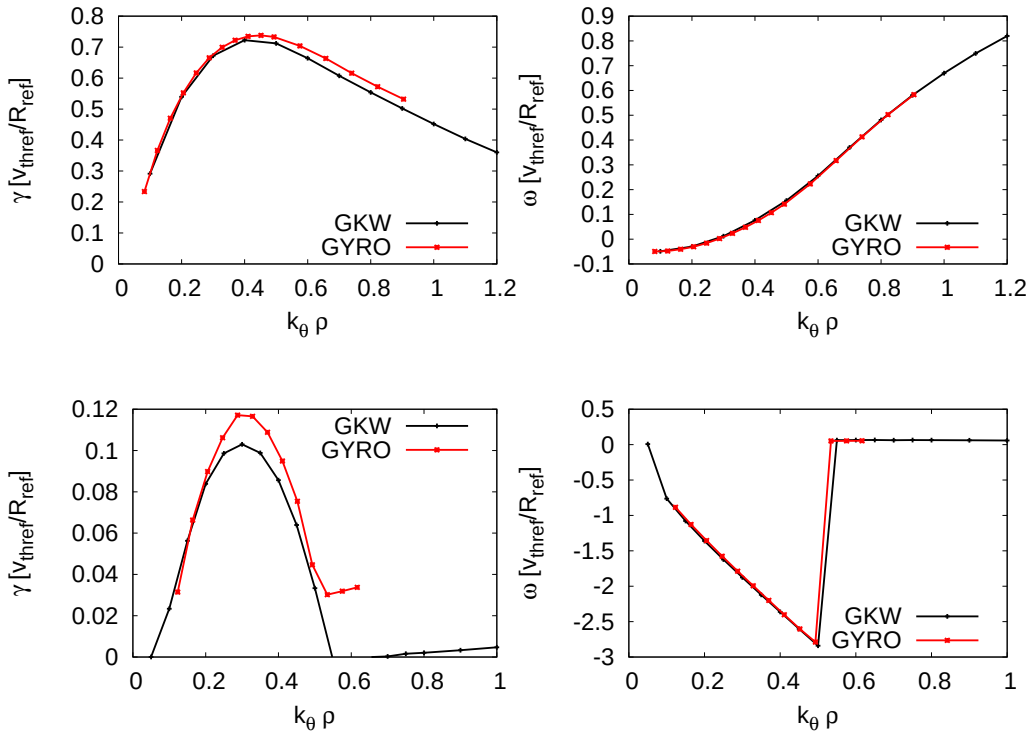

Figure 6.2: Comparison of the results from GYRO and GKW. Upper row is for a simplified case without electromagnetic effects, collisions or compressional effects, while the lower includes these effects. As can bee seen, the agreement of the codes is good.

at the rotational gradient

$$u' = -\frac{R_{ref}}{v_{thref}}\frac{\partial \Omega_\phi}{\partial \psi} = -\frac{\partial \Omega_N}{\partial \psi}, \tag{6.11}$$

with the reference thermal velocity.

$$v_{thref} = \sqrt{\frac{2T}{m}}. \tag{6.12}$$

The rotation adds terms to the drift of the particles

$$\frac{d\mathbf{X}}{dt} = \ldots + \frac{2mv_{||}}{ZeB}\mathbf{\Omega}_\perp - \frac{m\Omega^2 R}{ZeB}\mathbf{b}\times\nabla R \tag{6.13}$$

where the terms left out are the same as in Ref. [94] and Ω depicts the rotation frequency of the reference frame. The two terms are Coriolis and centrifugal drift, respectively. These have also been added in Ref. [94]. Second, rotation causes a

change of the background potential Φ. These is found using the quasi-neutrality condition

$$\begin{aligned} 0 &= \sum_{sp} Z_{sp} n_{R_0,sp} \exp\left(\frac{-Z_{sp}\langle\Phi\rangle}{T_{R,sp}}\right) \\ &\quad \cdot \exp\left(\frac{m_{sp}\Omega^2(R^2-R_0^2)}{T_{R,sp}}\right). \end{aligned} \tag{6.14}$$

Third, the rotation modifies the trapping condition. With rotation, particles are trapped if

$$v_\perp^2 = \frac{v_{||}^2 - \frac{2}{m}(\mathcal{E}_H - \mathcal{E}_L)}{\frac{B_H}{B_L} - 1}, \tag{6.15}$$

where H and L stand for the high and low field side, respectively and the species dependent centrifugal energy is defined as

$$\mathcal{E}(\theta) = Ze\Phi - \frac{1}{2} m_s \Omega^2 (R^2 - R_0^2). \tag{6.16}$$

Finally also the source term of the gyrokinetic equation changes. The terms due to rotation are

$$\begin{aligned} S &= \ldots - v_E \left[-\frac{m\Omega^2}{T} R_0 \left.\frac{\partial R_0}{\partial \psi}\right|_\theta \nabla\psi + \frac{\mu B + \mathcal{E}}{T}\frac{\nabla T}{T} \right. \\ &\quad \left. + \left(\frac{m v_{||} R B_t}{BT} + \frac{m\Omega}{T}[R^2 - R_0^2]\right)\nabla\omega_\phi \right] F_M. \end{aligned} \tag{6.17}$$

Here ω_ϕ is the rotation frequency of the plasma. As it is assumed that the rotation frequency of the frame and that of the plasma match at the chosen simulation, this means that the second term in the second line contains the product of rotation velocity and its gradient.

The simulations make also use of compressional effects, there inclusion is described in [32].

As the density varies around the flux surface, the densities and density gradients $R/L_{n,s}$ given in Tab. 6.2 and 6.3 are defined using density profiles at the low field side (LFS), $n_s(r, \theta = 0)$. Due to the centrifugal effects for the experimental rotation velocity, at the inboard side of the tokamak ($\theta = \pi$) the densities drop to 0.992, 0.956, and 0.975 relative to the outboard side ($\theta = 0$), for deuterium, carbon and electrons, respectively. The corresponding values for the density gradients are 0.983, 0.893 and 0.604.

The grid size in velocity space was $N_\mu = 16$ points for the magnetic moment, μ, and $N_{v_{||}} = 64$ for the parallel velocity. The number of points along the field lines differed for the two shots. Discharge 129064 was simulated with $N_s = 2208$ points

divided over 23 rotations of the field line (except for $k_\theta\rho = 0.3$, where this resolution had to be increased), while for discharge 129061 19 rotations of the field line are covered with $N_s = 1512$ points for low $k_\theta\rho$ and $N_s = 1008$ for higher values (≥ 0.6). Three species have been included in both discharges: deuterium, carbon and electrons. In the second discharge partially ionized tungsten ($Z = 39$) has been added as a trace species to investigate centrifugal effects on high-Z impurity transport. The actual experiments had no plasma facing components containing tungsten. Using high Z tiles in some parts is planned, which is an additional motivation for studying a tungsten trace. The time step was $5 \cdot 10^{-4}[v_{thref}/R_{ref}]$. The lithium in the second discharge has been neglected, as the contribution to the effective charge is small (i.e. $n_{Li}Z_{Li}^2/n_e \ll 1$) [111]. A check if the solution is sufficiently converged has been performed for the first shot at $k_\theta\rho = 0.2$. The resolution of each "direction" (μ, $v_{||}$, s, t, n_{period}) was doubled in individual runs. The maximum deviation from the values of the default grid size for growth rate, frequency and the ratio of heat to momentum flux (individually and sum) is 3%. Thus good convergence of the calculated values is reached in the simulations.
Since rotation velocities vary in the experiment, as seen in Fig. 6.1, simulations are performed not only for the experimental value of the rotation velocity as given in tab. 6.1, but also for twice this value. This helps to have a rough upper bound.

6.3 Modes in shot 129061

In this section the second shot (129061) is considered. First the nature of the instabilities and the impact of rotation are investigated.
Fig. 6.3 shows the growth rate (top) and the real frequency (bottom) as a function of $k_\theta\rho$. A negative frequency denotes a rotation in the electron diamagnetic direction. As can be seen from the figure that shows the frequency, two different modes are found in the $k_\theta\rho$ scan. The mode at higher $k_\theta\rho$ can be identified as a MTM, from its mode structure, parity and sign of the frequency. For the same reasons the second mode, at first, might appear to be a KBM, but scans over β_e (Fig. 6.4), R/L_{T_e} (Fig. 6.5) and ν_{ref} (Fig. 6.6) indicate that the situation is more complex. The mode shows no clear onset at a finite β_e as expected for a KBM. Instead, the growth rate remains finite, even for small values of β_e. On the other hand the β_e dependence gets stronger for values bigger than the experimental one. Due to this we refine our identification of this mode to a hybrid ITG-KBM as discussed in [112, 98].
The MTM mode shows a strong dependence upon β_e [108]. If β_e is reduced to approximately half the experimental value, then a transition to an ITG occurs.
Scans over the electron temperature gradient length R/L_{T_e} and the collision frequency are shown in Fig. 6.5 and 6.6, respectively. There is a strong increase of the MTM growth rate with R/L_{T_e} in NSTX [113]. Furthermore, as the core

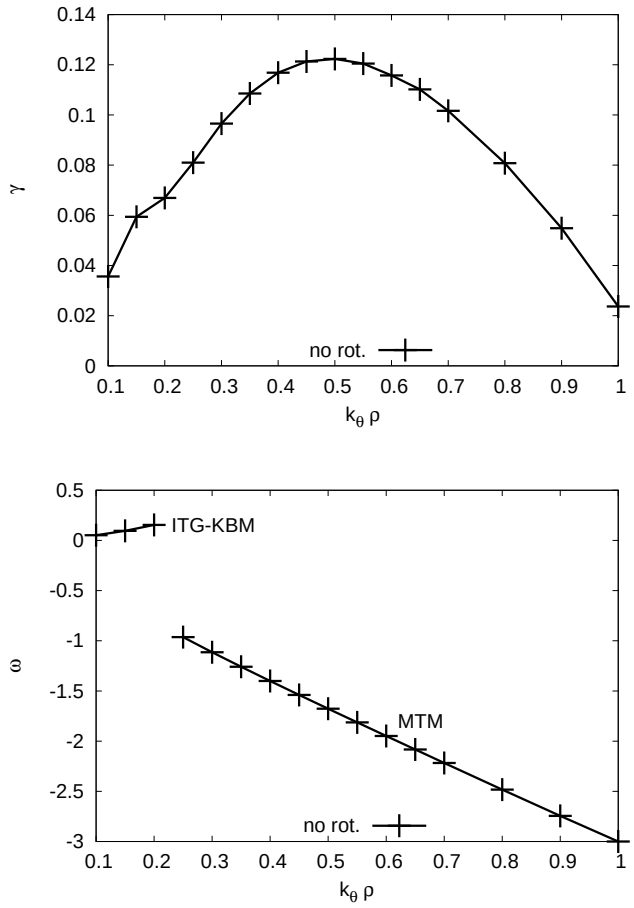

Figure 6.3: Growth rate (top) and real frequency (bottom) vs. $k_\theta\rho$.

MTM is destabilized by collisions, a switch to another mode at lower collisionality is found. This seems to be an ITG mode. Interestingly, also higher values of the collisionality stabilize the MTM.
Having identified the modes, we now turn to investigating the influence of various rotation effects on the strength of the instabilities. Figure 6.7 shows the same data as Fig. 6.3, plus lines for the case with rotation while taking only Coriolis effects into account. The labels u, u' and $u' + u$ mean that a finite rotation velocity u, a rotational gradient u' and both have been included in the simulations, respectively. It can be seen immediately that there is little difference in the real frequencies or growth rates of each mode, regardless of u or u'. Consequently, the value of $k_\theta\rho$ where the switch between the hybrid ITG-KBM and the MTM occurs, does not depend significantly on rotation.
This picture changes when full rotational effects (Coriolis and all centrifugal effects) are considered, as can be seen in Fig. 6.8. Values of the MTM growth rate increase about 10% for the experimental rotation values, while also the position

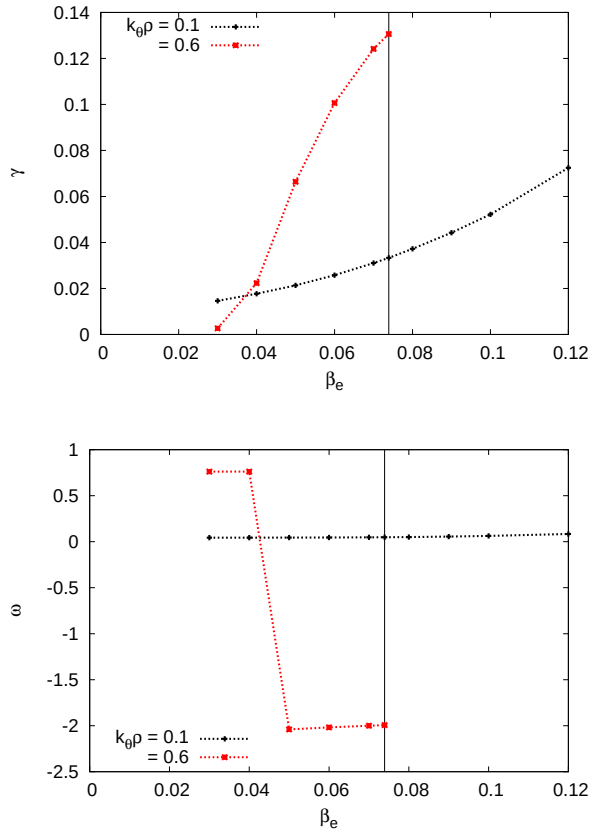

Figure 6.4: Growth rate (top) and real frequency (bottom) vs. β_e for two different wave vectors. The vertical line shows the default β_e (given in Tab. 6.1). The default case corresponds to the line for $u' + u$ (dashed, i.e. full rotational effects) of Fig. 6.8

of the maximum growth rate shifts to higher wave numbers. The effect on the frequency is less pronounced. The hybrid ITG-KBM on the other hand is slightly stabilized. As a result, the wavenumber where mode dominance changes is shifted to lower $k_\theta\rho$ when the rotation velocity is increased. In the limit of twice the experimental rotation velocity ($u' + 2u$), the ITG-KBM is only apparent in the lowest $k_\theta\rho$ simulated.

To isolate the influence of the inertial terms on the growth rates, additional simulations were run artificially including or excluding terms associated with the various centrifugal effects. For example, Figs. 6.9 shows the response of the ITG-KBM mode ($k_\theta\rho = 0.1$) to rotation when including only the Coriolis drift ('co'), only centrifugal drift ('cd'), or a case the includes the modification in trapping, poloidal asymmetry of density, and source terms ('tr') as discussed in Sec. II (Eqs. 13-17). In this case, the dominant effect (albeit relatively small) appears to be due to the stabilization associated with the centrifugal drift, while the Cori-

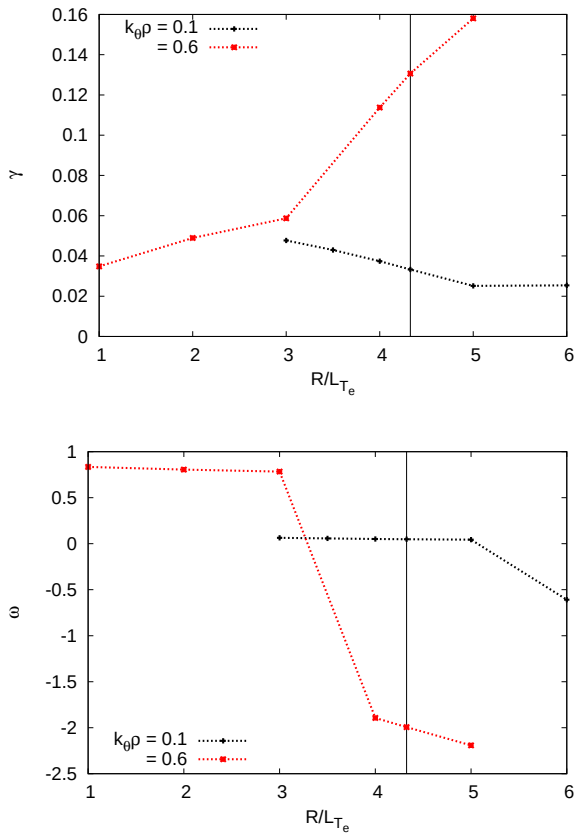

Figure 6.5: Growth rate (top) and real frequency (bottom) vs. R/L_{T_e} for two different wave vectors. Please note that for this scan β'_e was not fixed. The vertical line shows the default R/L_{T_e} (given in Tab. 6.3). The default case corresponds to the line for $u' + u$ (dashed, i.e. full rotational effects) of Fig. 6.8

olis drift and trapping effects have even smaller effect. We note that a decrease in growth rate with increasing rotation velocity was also found previously for electrostatic ITG modes Ref. [94]. In that case, the stabilization appeared to be due to both Coriolis and centrifugal drift terms, whereas the change in particle trapping and poloidal density variation was strongly destabilizing for similar rotation speeds ($u < 0.3$). Figure 6.10 shows the same for the microtearing mode ($k_\theta \rho = 0.7$). In this case, the growth rate is increased with rotation due to the changes associated with the particle trapping, poloidal density asymmetry and source terms.

To conclude, analysis of the shot number 129061 shows the presence of a hybrid ITG-KBM and a MTM. Centrifugal effects were shown to change the growth rate on the order of ten percent. In this case the effect is relatively small since the Mach number of deuterium is not large, and the modes are largely supported by the main species. Impurity transport, due to the higher Mach number of the

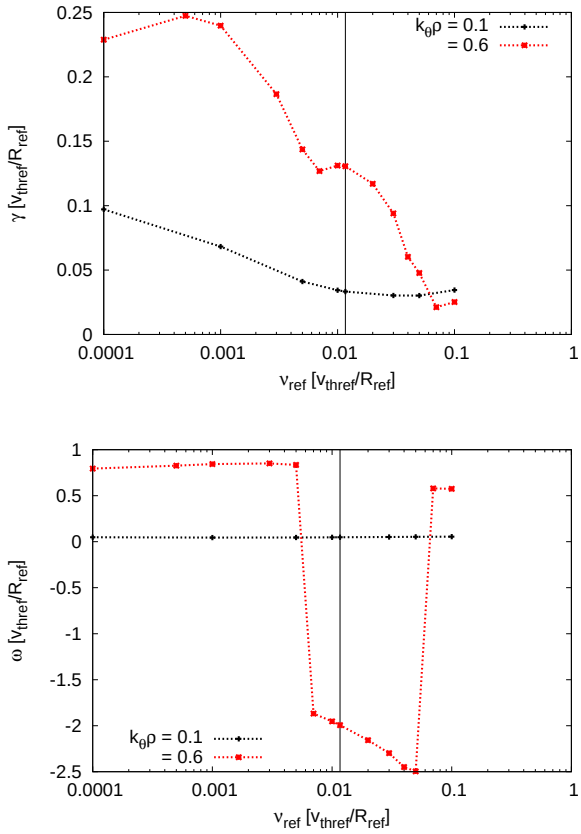

Figure 6.6: Growth rate (top) and real frequency (bottom) vs. ν_{ref} for two different wave vectors. The vertical line shows the default ν_{ref} (from parameters given in Tab. 6.1 and 6.3, see Appendix B for the computation). The default case corresponds to the line for $u' + u$ (dashed, i.e. full rotational effects) of Fig. 6.8

impurity species, as well as momentum transport react more strongly as we will see in the next two sections.

6.4 Particle transport

As MTM only contributes to electron heat flux, in this section the particle transport due to the hybrid ITG-KBM is investigated, which is shown to change strongly for the trace species, even if the growth rate and/or frequency do not. As electrons and deuterium have already been studied [24, 114], the focus will be on the intrinsic carbon impurity. We also consider a high-Z trace impurity which in this study we have chosen to be tungsten since it is being considered as a possible plasma facing component in fusion reactors [115]). Also we assume that the ITG-KBM will influence the particle and momentum transport, despite

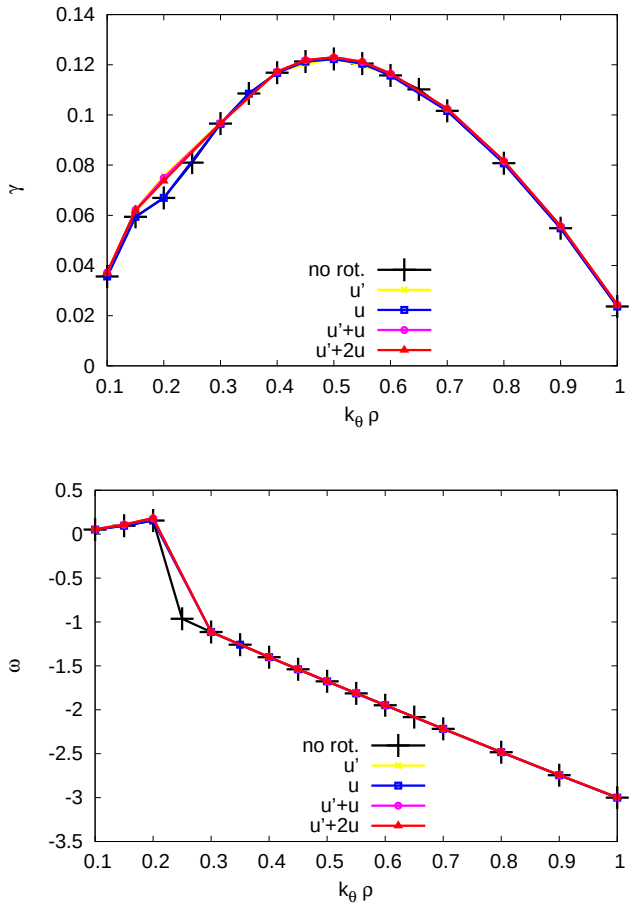

Figure 6.7: Growth rate (top) and real frequency (bottom) vs. $k_\theta\rho$ for different combinations of rotations and rotational gradients ($u = 0.1362$ and $u' = 0.9099$). Only Coriolis effects have been included.

the lower growth rates compared to the microtearing mode.
The particle fluxes of carbon and tungsten (normalized to the electron heat flux) are shown in Fig. 6.11 for the hybrid ITG-KBM. For the case with no rotation, both carbon and tungsten fluxes are inward directed (negative). For carbon this corresponds to down the gradient as it is locally hollow (see R/L_n in Tab. 6.3), consistent with a strong diffusive component. As there is no tungsten density gradient, the finite tungsten particle flux is dominated by the curvature + $E \times B$ compression pinch, which is proportional to impurity mass [94]. When including only the Coriolis drift, a finite rotation velocity has very little effect on the particle fluxes. However, a finite rotational gradient does drive an outward flux, an effect referred to as roto-diffusion. For tungsten this drive is strong enough to change the flux direction from inward to outward, while for carbon it makes the fluxes less negative. Including centrifugal effects in the simulations makes

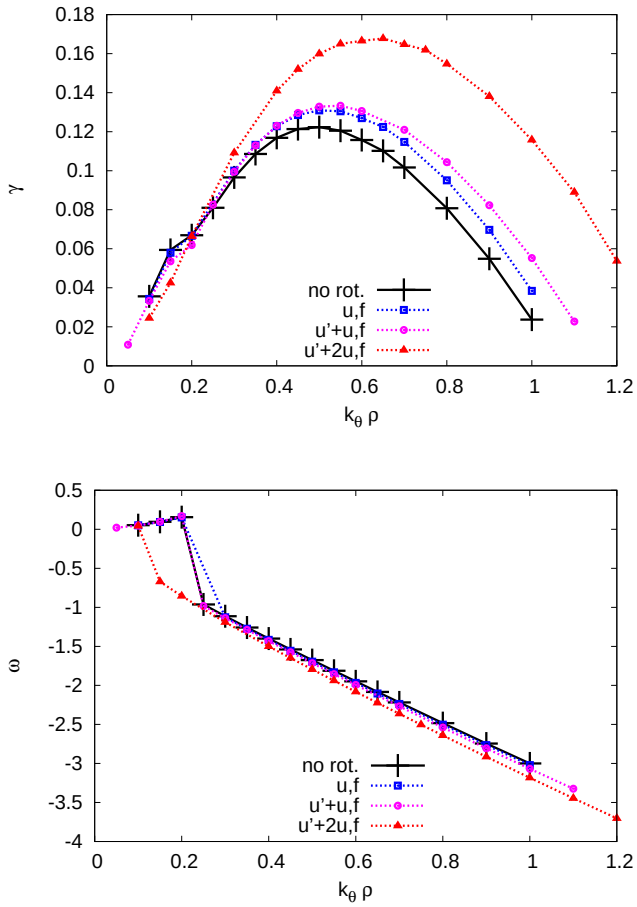

Figure 6.8: Growth rate (top) and real frequency (bottom) vs. $k_\theta\rho$ for different combinations of rotations and rotational gradients ($u = 0.1362$ and $u' = 0.9099$). All the rotational effects have been included.

little change to the carbon fluxes beyond the Coriolis and roto-diffusion effects, regardless of rotation or rotation shear. However, there is a much stronger influence on tungsten, as seen in Fig. 6.12. Centrifugal effects, when including only finite rotation (without shear), lead to a strong outward tungsten particle flux. With the addition of rotation shear the tungsten particle fluxes exhibits a non-monotonic dependence, first decreasing and becoming strongly negative for experimental values of flow shear, then increasing and returning to approximately zero for twice the experimental flow shear. Similar dependencies are found when varying rotation while keeping rotation shear fixed at the experimental value. This can be seen in Fig. 6.13 where the particle flux of both carbon and tungsten as a function of the rotation velocity is shown for $k_\theta\rho = 0.1$. The scan shows that the carbon flux is relatively insensitive to changes in rotation. Tungsten on the other hand shows a clear nonlinear dependence with rotation velocity. For small

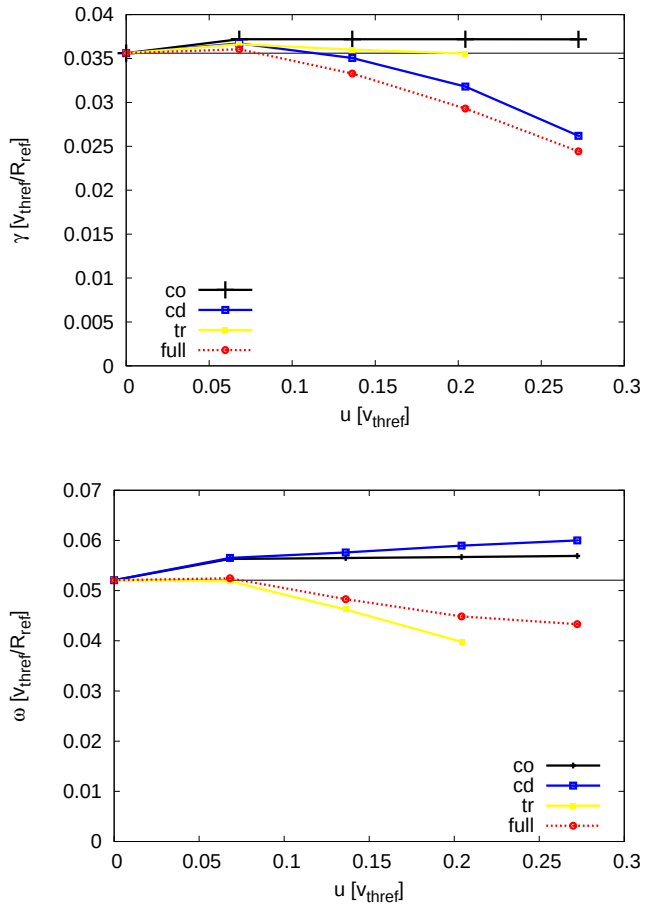

Figure 6.9: Growth rate (top) and real frequency (bottom) vs. rotation velocity u for the ITG-KBM mode at $k_\theta \rho = 0.1$. The horizontal lines highlight the values for no rotation. The meaning of the labels is as follows: 'co' Coriolis drift, 'cd' centrifugal drift, 'tr' centrifugal trapping and change in potential, 'full' all three.

rotation velocities ($u < 0.03$) an inward pinch increases nearly linearly. However, as rotation is increased further the inward particle flux is eventually weakened, approaching zero for twice the experimental rotation. This might be explained by the behaviour of the variation in strength of convective and the rotodiffusive transport coefficient as rotation velocity is increased [94]. Comparing Fig. 6.11 and Fig. 6.12 one can also see that the centrifugal effects proportional to u cause a strong outward tungsten flux. That the flux is inward with rotation and rotational gradient, suggests that effects proportional to $u \cdot u'$ are important.
The small flux without rotation means that the logarithmic density gradient $L_{n,W}$ needed to satisfy zero tungsten particle flux in the source-free core ($\Gamma_W = 0$) is almost zero, as can be seen in Tab. 6.4. With the experimental values for the rotation, the inward flux is stronger and thus a peaked density profile would be

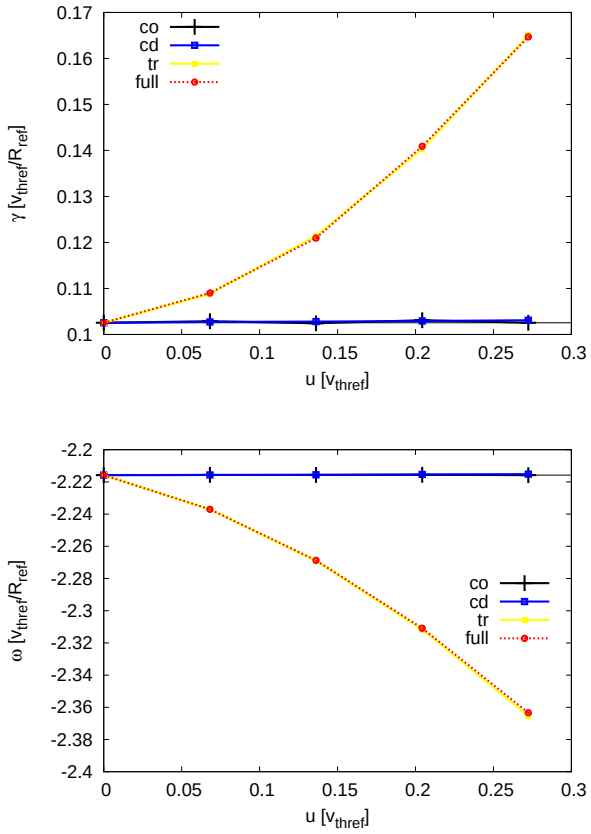

Figure 6.10: Growth rate (top) and real frequency (bottom) vs. rotation velocity u for the MTM mode at $k_\theta\rho = 0.7$ (not 0.6). The horizontal lines highlight the values for no rotation. The meaning of the labels is as follows: 'co' Coriolis drift, 'cd' centrifugal drift, 'tr' centrifugal trapping and change in potential, 'full' all three.

predicted. This is clearly unfavourable as the accumulation of high-Z impurities in the core can increase radiation losses and thus reduce confinement. However, given the complicated interplay between rotation and rotation gradient (which is similar to that found in Ref. [94] for ITG modes), this effect may very well be alleviated with a variation in rotation profiles, e.g. increasing the rotation velocity can reduce this problem.
Analogous to Tab. 6.4, the density gradient length, $R/L_{n,c}$, needed to satisfy zero carbon particle flux ($\Gamma_c = 0$ in the source-free core region) has been calculated from simulations using additional trace carbon species with different values of density ($R/L_{n,c} = \pm 5, 0$). Assuming a linear dependence of the flux on $R/L_{n,c}$, the offset and the declination can be computed, and from both the density gradient at which the flux is zero. The resulting $R/L_{n,c}$ should be an acceptable approximation assuming the transport can be approximated by a linear func-

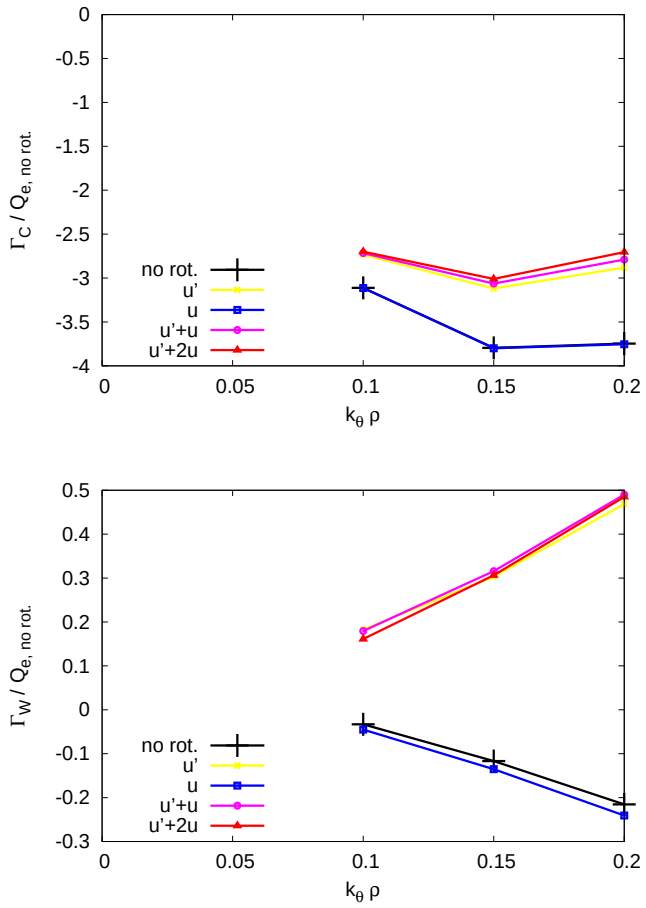

Figure 6.11: Particle flux for carbon (top) and tungsten (bottom) as a function of $k_\theta \rho$. Only Coriolis effects have been included.

tion of $R/L_{n,c}$. This has been verified by calculating $R/L_{n,c}$ using an additional simulation where the density gradients of the bulk species have been halved. The resulting $R/L_{n,c} = -3.5$ is within 20% of the value obtained using the first method ($R/L_{n,c} = -2.8$).
Fig. 6.14 shows the calculated density gradient length, $R/L_{n,c}$, needed for zero carbon particle flux for various values of rotation and rotation shear. In the absence of a rotation gradient ($u' = 0$, top panel) the simulations predict a peaked carbon profile, regardless of rotation and inclusion of centrifugal effects. This is consistent with the inward (negative) carbon fluxes found in Figs. 6.11 and 6.12 for $u' = 0$.
The picture changes significantly if also the rotation gradient is included (bottom panel). In this case roto-diffusion provides a strong outward particle flux. Therefore, a locally hollow profile ($R/L_{n,c} < 0$) is needed to obtain zero particle flux. If centrifugal effects are neglected (Coriolis only), the predicted gradient is

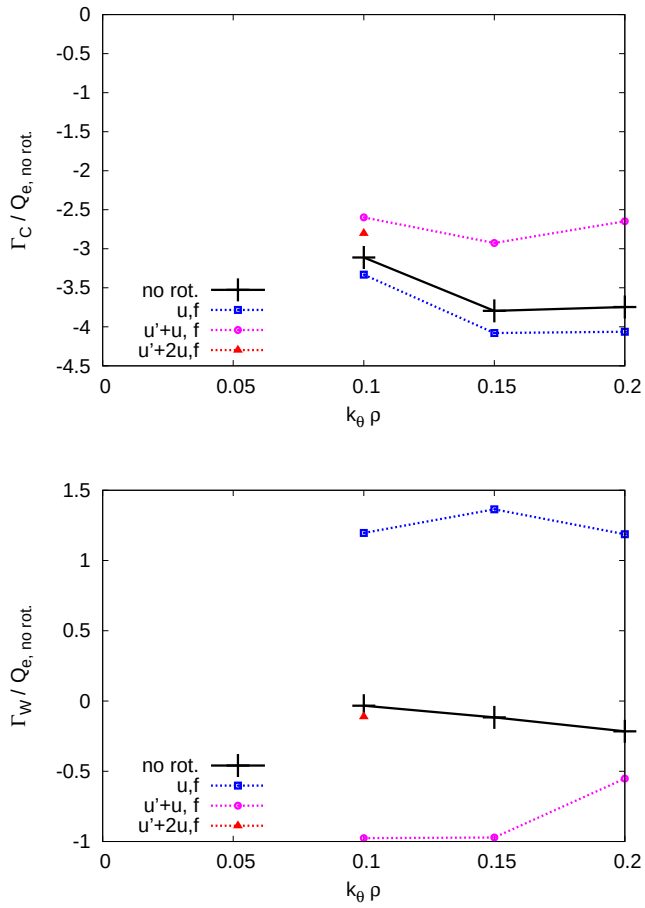

Figure 6.12: Particle flux for carbon (top) and tungsten (bottom) as a function of $k_\theta \rho$. All rotational effects have been included. The case $u' + 2u$ has only one point as for higher $k_\theta \rho$ the mode switches.

$R/L_{n,c} \approx -0.85$ and is largely independent of rotation (u). Including centrifugal effects leads to an enhancement in the hollowing that increases with toroidal rotation. For the experimental rotation $u_{exp} = 0.14$, $R/L_{n,c} \approx -2.8$ is nearly three times bigger. This value of the density gradient is notably similar to the experimental value $R/L_{n,c-exp} = -3.5$. If this effect is manifested in nonlinear simulations, it suggests that the locally inverted carbon profile (in this source-free region) is a due to a balance between diffusive effects and the strong outward transport from both roto-diffusion and centrifugal effects for the ITG-KBM instability.

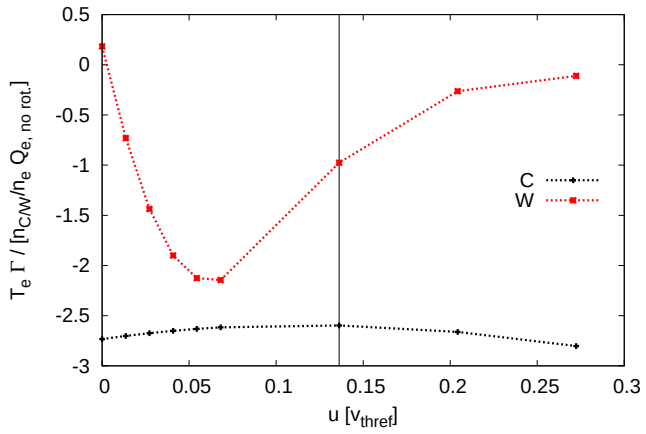

Figure 6.13: Particle flux for carbon and tungsten as a function of rotation velocity u. The scan has been done with Coriolis and centrifugal effects at $k_\theta\rho = 0.1$.

Table 6.4: Density gradients for zero tungsten particle flux at $k_\theta\rho = 0.1$. If the simulation included rotation then all effects have been activated.

rotation	$R/L_{n,W}\vert_{\Gamma_W=0}$
no	0.008
yes	1.112

6.5 Momentum transport

In this section will be presented the results for the momentum flux of the hybrid ITG-KBM.
Fig. 6.15 shows the momentum flux normalized to the ion (deuterium+carbon) heat flux for carbon and deuterium over $k_\theta\rho$ with only Coriolis effects. Without rotational gradient the fluxes are small but finite, indicative of a residual stress. Both species show a similar response to rotation and rotation gradient, which is not unexpected due to the coupling through charge neutrality. Specifically, with a finite rotational gradient there is an outwards directed diffusive flux of momentum ($\Pi \sim \chi_\phi u'$). The momentum fluxes change very little when including finite rotation, indicating that any momentum pinch ($\Pi \sim V_{pinch} u$) due to the Coriolis drift is very small. When including centrifugal effects (Fig. 6.16), there is also little change observed, except for the case of double rotation ($u' + 2u$). In this case the flux is lower compared to the case with just the experimental rotation. This is not the case for carbon, the flux is almost unaffected.
To better quantify the above effects, the momentum flux has been decomposed

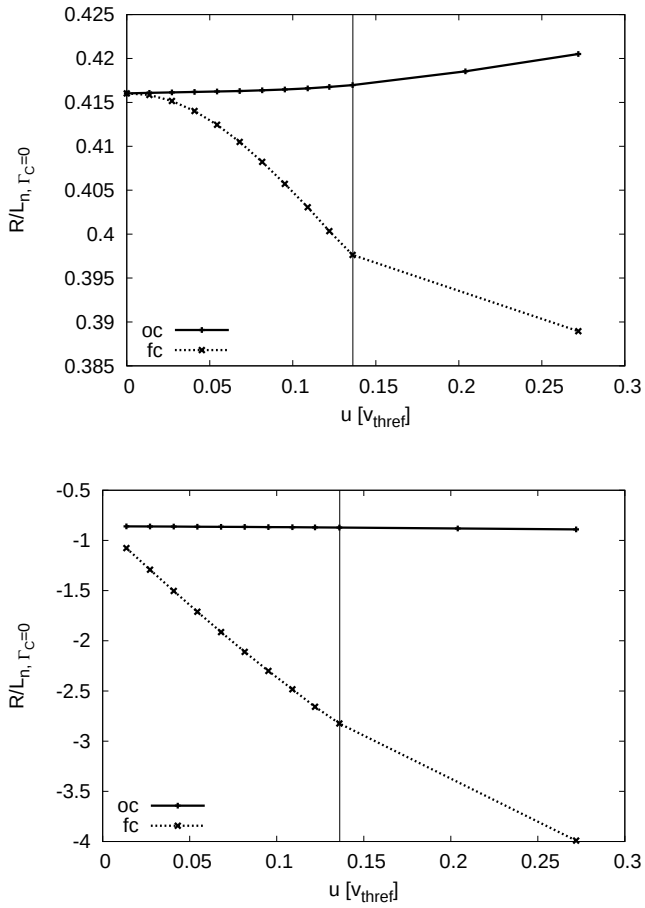

Figure 6.14: Density gradient length for zero carbon particle flux. With $u' = 0$ (top) and the experimental value $u' = 0.9099$ (bottom), for the case with only the Coriolis effects (oc) and all the rotational effects (fc).

according to the model

$$\frac{\Pi_\phi^l}{Q_i^l}\frac{v_{thref}}{R_0} = \frac{2}{R/L_{T_i}}\frac{\chi_\phi}{\chi_i}\left[u' + \frac{R_0 V_{co}}{\chi_\phi}u + \frac{C^*}{\chi_\phi} + cuu'\right]. \tag{6.18}$$

Here $Pr = \chi_\phi/\chi_i$ is the Prandtl number, $R_0 V_{co}/\chi_\phi$ the pinch coefficient and C^*/χ_ϕ the residual stress. The last term $c = c^*/\chi_\phi$ has been added (compared to [30]) as a check if the effects related to both the rotation and rotation gradient might be important, as noted in [94]. Π_ϕ^l and Q_i^l here refer to the sum of the deuterium and carbon momentum and heat fluxes, respectively. These have been calculated from simulations using all combinations of zero or experimental rotation and rotation gradient. Thus we obtain a linear system with the transport coefficients as unknowns that can be solved for.
The resulting transport coefficients are shown in Fig. 6.17. The Prandtl number

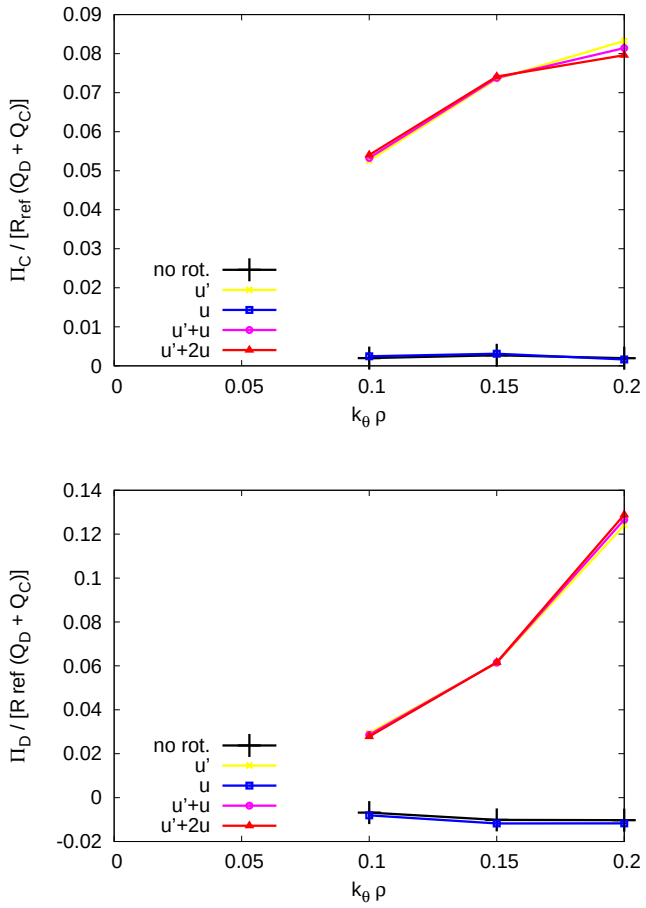

Figure 6.15: Momentum flux normalized to ion (deuterium+carbon) heat flux for carbon (top) and deuterium (bottom). Only Coriolis effects have been included.

for the ITG-KBM mode is predicted to be very small, $Pr \sim 0.1 - 0.2$, which is much smaller than values ($Pr \sim 0.7 - 1.0$) typical for electrostatic ITG, TEM or KBM instabilities (see e.g. [116]). The predicted Coriolis pinch without centrifugal effects is also small $R_0 V_{co}/\chi_\phi \sim -0.1$, but this has been predicted previously for KBM instability at higher aspect ratio [117]. The strength of the Coriolis pinch is roughly doubled when including centrifugal effects (blue dashed line). The overall small pinch from ITG-KBM apparently can not explain the larger momentum pinches measured in similar NSTX H-mode plasmas ($R_0 V_\phi/\chi_\phi \sim (-1) - (-7)$) [97]. Therefore we look at the other possible contributions in Eq. (6.18).
There is a finite residual stress predicted, although it's relative magnitude is no larger than the pinch contribution. This residual stress is due to an up-down asymmetry introduced by the finite derivative of the vertical position Z_0 with respect to radial coordinate (dZ_{mil}) in the geometry description. This has been

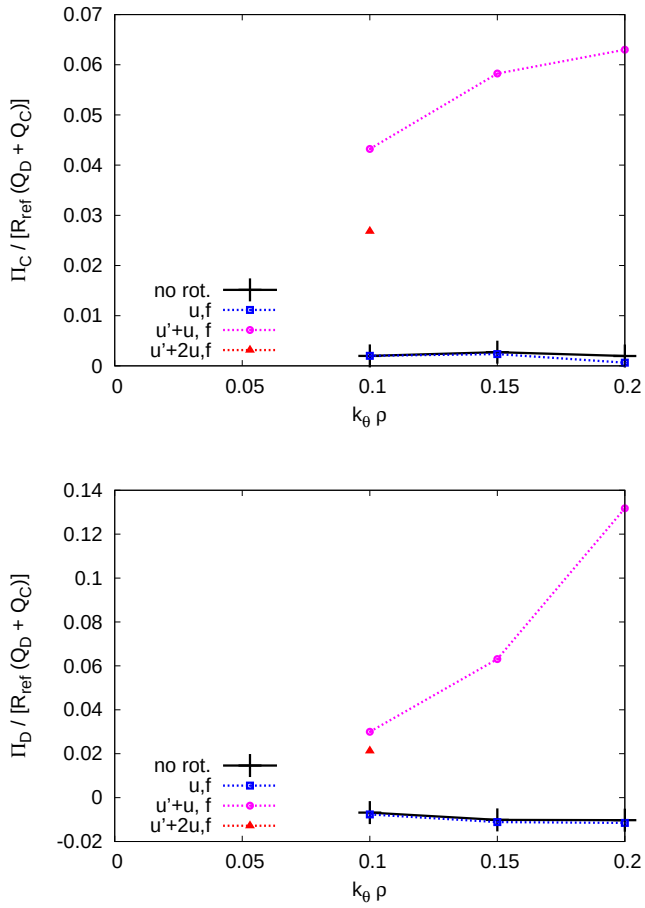

Figure 6.16: Momentum flux normalized to ion (deuterium+carbon) heat flux for carbon (top) and deuterium (bottom). All rotational effects have been included.

verified by additional simulations that show the the residual stress is reduced by four orders of magnitude if dZ_{mil} is reduced to zero.
The residual stress should not change when including centrifugal effects, as this describes the flux without rotation. The Prandtl number also does not change. Thus those two have not been computed again with full rotational effects.
The strongest contribution to the momentum fluxes appears to come from the $u \cdot u'$ coefficient when including centrifugal effects. In the absence of centrifugal effects this term is very small, and should be identically zero in the limit that the various terms in Eq. (6.18) can be decomposed exactly as linear contributions. However, with centrifugal effects included, this term provides an inward flux contribution that is ~ 3 times larger than the Coriolis pinch contribution. This additional centrifugal effect will be explored more carefully in future work to determine whether it can provide a possible explanation of the observed momentum

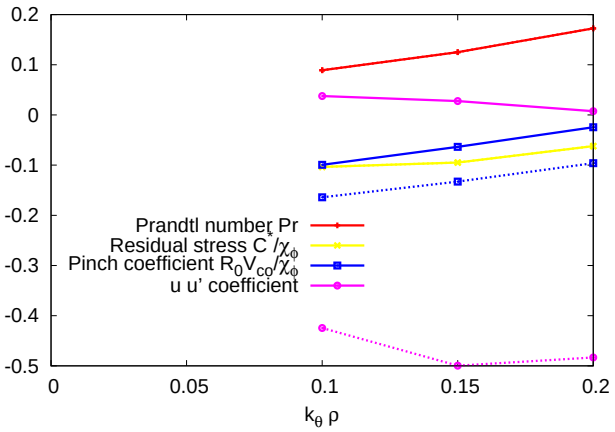

Figure 6.17: The transport coefficients vs. $k_\theta\rho$ in the hybrid KBM range. Full lines refer to only Coriolis effects while dashed line includes also centrifugal effects. Prandtl number and residual stress have not been computed with centrifugal effects.

pinches in NSTX H-modes.

6.6 Conclusions

The influence of centrifugal effects on microstability (including centrifugal drifts, change of background potential, change of trapping condition and change of source term in the gyrokinetic equation) has been investigated using the GKW code for relatively high-beta NSTX H-mode plasmas. The linear, flux-tube simulations predict the presence of both MTM and hybrid ITG-KBM electromagnetic instabilities in the outer core (r/a=0.7), inferred from mode structure and parameter scans. Both instabilities respond weakly to changes in rotation and rotation shear for the experimental parameters investigated, although the MTM growth rates appear to be strengthened for values of rotation increased beyond the local values ($u > 0.1$), specifically due to centrifugal effects.
Quasi-linear fluxes have been calculated for the ITG-KBM modes to estimate what effect they might have on impurity and rotation profiles. The assumption has been made that the ITG-KBM effects are present even though in this case the growth rates are weaker than the microtearing mode (which contributes only to electron heat flux). This assumption will be tested in future nonlinear simulations. The carbon density gradient predicted in the absence of a source ($\Gamma_c \approx 0$, appropriate for these core conditions) is found to be locally hollow ($R/L_{nc,C} < 0$). This prediction is dependent on including finite rotation shear ($u' > 0$), and is strengthened when centrifugal effects are included. These results provide a pos-

sible explanation for the inverted carbon profile measured at this location [100], which could not be explained by neoclassical theory (as is usually the case). In contrast, if only Coriolis effects are included ($u' = 0$), an inward pinch and peaked carbon profile ($R/L_{nc,C} > 0$) is calculated, inconsistent with experimental results. For a trace high-Z impurity (assumed here to be tungsten), the influence of rotation when including centrifugal effects is strongly non-monotonic. For the experimental values of this investigation, a strong inward pinch is predicted. However, this high-Z impurity flux can be reduced considerably for either weaker or stronger rotation. This effect was predicted previously for simpler geometry [94], and has been extended here to realistic low aspect ratio geometry, assuming the presence of a trace tungsten species. High-Z impurity transport and its sensitivity to rotation will be investigated in future NSTX-Upgrade [118] experiments.
When including all rotation effects, the simulated momentum flux is outward, consistent with the central torque deposition from NBI heating. However, the diffusive and Coriolis pinch contributions predicted from the ITG-KBM simulations are relatively small, with $Pr \sim 0.1 - 0.2$ and $R_0 V_{co}/\chi_\phi \approx 0.1 - 0.2$. We note in the present investigation that the strength of the pinch is enhanced when centrifugal effects are included, although they remain much smaller than experimental observations in similar NSTX H-mode plasmas [97]. However, there is an additional contribution to the inward momentum flux from a term proportional to the product of uu', which is ~ 3 times bigger than the Coriolis pinch contribution. This additional mechanism may provide a possible explanation for the experimental observations and will be explored in future work.
Within this chapter the rational gradient has not been changed, only switched on/off for some of the scans. At least in the inside of the plasma there seems to be a relation of rotation and its gradient in NSTX. It would thus be desirable to check how transport is affected, when both are changed according to this relation. We leave this for a future investigation.

6.7 Acknowledgments

We would like to thank R.E. Bell and B.P. LeBlanc for providing the experimental fits for the discharges analysed in this chapter and F. Scotti for the TRANSP runs, from which the profiles for the simulations have been used. We thank F. Scotti also for helpful comments.

Chapter 7

Summary

In this thesis, the gyrokinetic-Vlasov code GKW is used to study turbulent transport, with a focus on radial transport of toroidal momentum. To support the studies on turbulent transport an eigenvalue solver has been implemented into GKW. This allows to find, not only the most unstable mode, but also subdominant modes. Furthermore, it is possible to follow the modes in parameter scans. Finding multiple modes can give insight into nonlinear simulations. In nonlinear systems also subdominant and even stable modes can influence the plasma. The eigenvalue solver has already been used by others to determine the influence of subdominant modes on electron transport in an ITER scenario [55].
The transport of momentum can cause intrinsic rotation, i.e. rotation that develops without external torque. Two fundamental mechanisms that can generate an intrinsic rotation have been investigated: profile shearing and the velocity nonlinearity.
The toroidal momentum transport in a tokamak due to profile shearing has been investigated. The study shows that the momentum flux can not be accurately described by the gradient in the turbulent intensity. Consequently a description using the profile variation is used. A linear model has been developed that is able to reproduce the variations in the momentum flux as the profiles of density and temperature vary, reasonably well. It uses not only the gradient length of density and temperature profile, but also their derivative, i.e. the second derivative of the logarithm of the temperature and the density profile. It is shown that both first as well as second derivatives contribute to the generation of a momentum flux. A difference between the linear and nonlinear simulations has been found with respect to the behaviour of the momentum flux. In linear simulations the momentum flux is independent of ρ_*, while in nonlinear simulations the momentum flux scales linear with ρ_* for sufficiently small ρ_* ($\leq 4 \cdot 10^{-3}$). Nonlinear simulations reveal that the profile shearing can generate an intrinsic rotation comparable to that of current experiments. Under reactor conditions, however, the intrinsic rotation from the profile shearing is expected to be small

due to the small normalized Larmor radius $\rho_* \lesssim 5 \cdot 10^{-4}$.
The velocity nonlinearity has been derived and the implementation in GKW has been tested. Simulations at $\rho_* = 10^{-3}$, and parameters of the Waltz standard case, did not show a significant momentum transport, contrary to what would be expected due to the breaking of symmetry. A possible explanation is, that the turbulence causes a random-like transport with zero mean.
Finally, the influence of rotation on particle and momentum transport has been studied, with a focus on the effects caused by the centrifugal force at parameters that represent experiments in NSTX. While the growth rates and frequencies are not strongly affected by the centrifugal effects, they have a strong influence on the particle and momentum flux. For the carbon impurity a hollow density profile has been observed in NSTX. This observation can be explained if centrifugal effects are kept in the description of the unstable modes. In the modelling of the toroidal momentum transport it has, furthermore, been shown that a "nonlinear term" $\propto u \cdot u'$ can be of importance for the result, as it will generate an inward flux of toroidal momentum. Future investigations may take into account a relation between rotation and rotational gradient. Another interesting point is, how the rotation affects the transport in nonlinear simulations

Appendix A

Velocity nonlinearity in the electromagnetic case with rotation

The time derivative of the parallel velocity (multiplied by $mv_\parallel$) is

$$mv_\parallel \frac{\mathrm{d}v_\parallel}{\mathrm{d}t} = -\frac{\mathrm{d}\underline{X}}{\mathrm{d}t} \cdot \nabla H - Ze\frac{\mathrm{d}\underline{X}}{\mathrm{d}t} \cdot \frac{\partial \underline{A}^*}{\partial t}. \tag{A.1}$$

The third term in the gyrokinetic equation therefore adds terms in the form

$$\frac{\partial f}{\partial t} \stackrel{+}{=} \frac{1}{mv_\parallel}\left[\frac{\mathrm{d}\underline{X}}{\mathrm{d}t} \cdot \nabla H + Ze\frac{\mathrm{d}\underline{X}}{\mathrm{d}t} \cdot \frac{\partial \underline{A}^*}{\partial t}\right]\frac{\partial f}{\partial v_\parallel}. \tag{A.2}$$

Inserting H and $\underline{A}$, neglect the linear terms that are already contained in GKW, use the geometry tensors (2.66)-(2.75) and normalize the terms to get

$$\begin{aligned}
\frac{\partial f_N}{\partial t_N} \stackrel{+}{=} & \rho_* \frac{\mathcal{F}_\mathcal{N}}{m_N v_{GN}} \left(m_N v_{GN}^2 \mu_N \frac{\partial \langle B_{1\parallel N} \rangle}{\partial s_N} + \frac{Z}{2} \frac{\partial \langle \phi_N \rangle}{\partial s_N} \right) \frac{\partial f_N}{\partial v_{\parallel N}} + \rho_* \frac{Z}{m_N v_{GN}} \frac{\partial \langle A_{\parallel N} \rangle}{\partial t_N} \frac{\partial f_N}{\partial v_{\parallel N}} \\
& - \rho_* \frac{2 s_B \Omega_N}{v_G} \left(\frac{v_{GN}^2 \mu_N}{Z} \frac{\partial B_N}{\partial x_N^\beta} + \rho_* \frac{v_{GN}^2 \mu_N}{Z} \frac{\partial \langle B_{1\parallel N} \rangle}{\partial x_N^\beta} \right. \\
& \left. + \rho_* \frac{\partial \langle \phi_N \rangle}{\partial x_{\beta N}} + \frac{1}{2} \frac{\partial \Phi_N}{\partial x_N^\beta} - \frac{m_N \Omega_N^2}{2Z} \frac{\partial R_N^2}{\partial x_N^\beta} \right) \mathcal{H}_N^\beta \frac{\partial f_N}{\partial v_{\parallel N}} \\
& + \rho_* v_{\parallel N} \left(- \frac{m_N v_{GN}^2 \mu_N B_N}{2Z} \beta'_N \mathcal{D}_N^\psi + \rho_* \frac{m_{ref} v_{GN}^2 \mu_N}{Z} \frac{\partial \langle B_{1\parallel N} \rangle}{\partial x_{N^\beta}} \mathcal{D}_N^\beta \right. \\
& + \rho_* \frac{m_N v_{GN}^2 \mu_N}{Z} \beta'_N \frac{\partial \langle B_{1\parallel N} \rangle}{\partial x_N^\beta} \mathcal{E}_N^{\psi\beta} + \rho_* \frac{1}{2} \beta'_N \frac{\partial \langle \phi_N \rangle}{\partial x_N^\beta} \mathcal{E}_N^{\psi\beta} + \frac{1}{2} \frac{\partial \Phi_N}{\partial x_{N^\beta}} \mathcal{D}_N^\beta + \frac{\beta'_N}{2} \frac{\partial \Phi_N}{\partial x_N^\beta} \mathcal{E}_N^{\psi\beta} \\
& \left. - \frac{m_N \Omega_N^2}{2Z} \frac{\partial R_N^2}{\partial x_N^\beta} \mathcal{D}_N^\beta - \frac{m_N \Omega_N^2}{2Z} \beta'_N \frac{\partial R_N^2}{\partial x_N^\beta} \mathcal{E}_N^{\psi\beta} \right) \frac{\partial f_N}{\partial v_{\parallel N}} \\
& + \rho_*^2 \frac{2}{m_N v_{GN}} \left(m_N v_{GN}^2 \mu_N \frac{\partial B_N}{\partial x_N^\beta} + \rho_* m_N v_{GN}^2 \mu_N \frac{\partial \langle B_{1\parallel N} \rangle}{\partial x_N^\beta} + \rho_* \frac{Z}{2} \frac{\partial \langle \phi_N \rangle}{\partial x_N^\beta} \right. \\
& \left. + \frac{Z}{2} \frac{\partial \Phi_N}{\partial x_N^\beta} - \frac{m_N \Omega_N^2}{2} \frac{\partial R_N^2}{\partial x_N^\beta} \right) \mathcal{E}_N^{\alpha\beta} \frac{\partial \langle A_{\parallel N} \rangle}{\partial x_N^\alpha} \frac{\partial f_N}{\partial v_{\parallel N}}. \qquad \text{(A.3)}
\end{aligned}$$

It should be noted that two of the terms are of second order in ρ_* (compared to the leading order terms), namely the two nonlinear terms in the last bracket, that involve a triple product of three perturbed quantities. All the other terms are of first order. The appearance of the $\partial \langle A_\parallel \rangle / \partial t$ term makes an implementation not straight-forward. Without the velocity nonlinearity one has also the time derivative of the perturbed parallel potential. In that case it can be dealt with by introducing the distribution function $g = f + Zev_\parallel \langle A_\parallel \rangle F_M$. For the velocity nonlinearity this does not work, as the term added here is nonlinear.

Appendix B

Computation of collisionality for discharge #129061 of NSTX

Here for reference the collisionality for the base parameters of the second shot is computed.
The Coulomb logarithm can be calculated as [31]

$$\begin{aligned} \ln \Lambda^{i_1/i_2} &= 17.3 - \ln\left[\frac{Z_1 Z_2 (m_1+m_2)}{m_1 T_{R2} T_{ref}^k + m_2 T_{R1} T_{ref}^k}\right] - \frac{1}{2}\ln\left[0.1\frac{n_{ref}^{19}}{T_{ref}^k}\right] \\ &\quad -\frac{1}{2}\ln\left[\frac{n_{R1} Z_1^2}{T_{R1}} + \frac{n_{R2} Z_2^2}{T_{R2}}\right]. \end{aligned} \tag{B.1}$$

Here $m_{1/2}$ is the relative mass (or absolute, does not matter as the absolute part will cancel), $Z_{1/2}$ is the charge, T_{ref}^k is the reference temperature (in keV), n_{ref}^{19} is the reference density (in $10^{19} m^{-3}$), $T_{R1/2}$ and $n_{R1/2}$ are the relative temperature and density, respectively.
The Coulomb logarithm is needed for the reference collision frequency

$$\nu_{ref} = 6.5141 \cdot 10^{-5} R_{ref} n_{ref}^{19} \frac{\ln \Lambda^{i/i}}{(T_{ref}^k)^2}. \tag{B.2}$$

Inserting the values results in

$$\ln \Lambda^{i_1/i_2} = 16.774 \tag{B.3}$$

$$\nu_{ref} = 1.1661 \cdot 10^{-2} \tag{B.4}$$

Appendix C

Glossary

Alfven wave Waves that are derived from MHD equations, that appear due to restoring force of the magnetic field, when the field is bend or compressed.

ballooning mode/instabilities Ideal MHD modes with large torroidal mode number. Ballooning instabilities are driven by pressure gradients, and are localized in regions with unfavourable magnetic-field-line curvature [119].
See also KBM.

bootstrap current Current driven by internal effects. Two parts: "Banana current", analogue of diamagnetic current, here just with banana orbits. This is the minor part. Other part is due to passing particles. An asymmetry in the distribution function is created from coupling of trapped and passing particles by collisions [120]. Reason for bootstrap current is anisotropy in electron pressure tensor [8].

compressional effects Name for effects that enter due to perpendicular parts $\underline{A}_\perp = \underline{A} - (\underline{A} \cdot \hat{\underline{b}})\hat{\underline{b}}$ of the perturbed vector potential $\underline{A}$.

Debye length The length

$$\lambda_D = \left(\frac{\epsilon_0 T}{ne^2}\right)^{1/2} \tag{C.1}$$

over which a charge separation could occur in a plasma.

Debye shielding Describes the shielding of the potential of a particle in a plasma due to a reordering of other particles. The potential therefore goes not as $1/r$ but gets an additional factor that decays exponentially.

Diamagnetic current Current $\underline{j}_\perp$ that reduces the external magnetic field.[2]

$E \times B$ **velocity** Particle drift due to the combined effect of the electric and magnetic field.

f**,** δf The perturbed distribution function.

flux function Functions that are constant on a magnetic surface, i.e. on the surface of constant poloidal flux.

Grad-Shafranov equation Equation for the poloidal flux in cylindrical coordinates for an axisymmetric system, that is in an equilibrium, i.e. $\underline{J} \times \underline{B} = \nabla p$.

$$0 = L(\psi) + \mu_0 r^2 \frac{\partial p(\psi)}{\partial \psi} + \frac{\mu_0^2}{8\pi^2} \frac{\partial I^2(\psi)}{\partial \psi} \tag{C.2}$$

$$L(\psi) = \left(r \frac{\partial}{\partial r} \frac{1}{r} \frac{\partial}{\partial r} + \frac{\partial^2}{\partial z^2} \right) \psi \tag{C.3}$$

gyrocentre coordinates Gyroaveraged guiding-centre coordinates, i.e. via averaging over the fast gyromotion, the dependence from the gyroangle is removed.

Hamada-coordinates Coordinates chosen such, that the contra-variant components of the magnetic field are flux functions. Hamada coordinates are not necessarily orthonormal.

H-mode In 1982 an unusual high confinement was found [12], that was labelled H-mode, or high confinement mode.

intrinsic rotation The rotation that develops without external torque.

ITG mode Ion temperature gradient mode.

KBM Short for kinetic ballooning mode. Model: analogue to oscillating guitar string, magnetic fields provides tension, plasma the inertia. Background potential and fluctuations are perpendicular. Driven by pressure Gradient in bad curvature region. [121]
For a KBM in GKW real and imaginary part of the perturbed parallel magnetic potential are out of phase and the frequency is in ion diamagnetic direction.

Landau damping Collisionless damping mechanism for plasma waves. Assume a wave with a certain phase velocity. Electrons with slightly lower velocity are accelerated, those with slightly higher velocity will decelerate. If the former gain more energy than the latter loose (i.e. because there are more slow than fast electrons), then there is an overall transfer of energy from the wave to the electrons and the wave is damped [2].

Larmor radius The gyroradius (also known as radius of gyration, Larmor radius or cyclotron radius) is the radius of the circular motion of a charged particle in the presence of an uniform magnetic field.

$$\rho = \frac{m v_\perp}{|Z|B} \tag{C.4}$$

where m is the mass of the charged particle, $\underline{v}_\perp = \underline{v} - \underline{v}(\underline{v}, \underline{B}/B)$ is the velocity component perpendicular to the direction of the magnetic field, Z is the charge of the particle, and B is the constant magnetic field.
For ions the Larmor radius in tokamaks is of the order of millimetres, while the electron Larmor radius is approximately an order of magnitude smaller, due to the smaller mass.

LFS Short for low field side. Depicts the outer side of the torus, where the toroidal magnetic field is lower, due to the $1/R$ dependence. Opposite to HFS.

microinstabilities Instabilities with a wavelength of the order of the Larmor radius.

microtearing mode (MTM) Tearing modes are characterized by a tearing of the field, which causes reconnection and the formation of an island. For a microtearing mode, the perturbations are on the length scale of a few ion Larmor radii, and they are driven by free energy in electron temperature gradient [122]

$\mu = m v_\perp^2/(2B)$ Magnetic moment, related to the velocity perpendicular to the magnetic field.

parallel/perpendicular (direction) (The direction) parallel/perpendicular to the magnetic background field.

plasma an ionized gas, which is overall charge neutral. The high charge density means small separations of the species would lead to high forces, therefore the

plasma is quasineutral.
This can be cast down to three basic properties [3], two that compare the macroscopic properties with the characteristic properties of the system

- Debye length is small $\lambda_D \ll L$.
- Plasma frequency is high $\omega_p \gg \omega_T = v_T/L$,

and one that compares the microscopic Coulomb collisions to the characteristic properties of the system

- Collisionality must be low, which requires $\Lambda_D \gg 1$.

For a fusion plasma there are additional constraints due to the magnetic field [3]

- Gyrofrequency ω_c of electrons and ions must be large compared to the thermal transit time $\omega_{c,e}, \omega_{c,i} \gg \omega_T$.
- The gyroradius r_g of electrons and ions must be small compared to the dimension of the system $r_{g,e}, r_{g,i} \ll L$.

If these where not fulfilled, the system would not be magnetically confined.

ψ Radial direction.

R Major radius of the torus.

ρ_* Is the Larmor radius of ions with thermal velocity, divided by major radius. If the size of a tokamak is increased, the other dimensionless parameters can remain the same (collisionality, beta, aspect ratio, safety factor, etc.), except for ρ_*, which will decrease under these circumstances.[123]

s Parallel direction.

safety factor q The ratio of toroidal to poloidal turns of a magnetic field line is the safety factor. For circular flux surfaces at low aspect ratio $q = r/RB_\phi/B_\theta$.

Temperature T Depicts within this thesis k_BT (if not stated otherwise), as is usual in plasma physics.

tokamak Type of magnetic confinement fusion reactor. Poloidal part of the magnetic field is created via current(s) in the plasma. The toroidal part is created via coils. The need to drive the current allows so far only pulsed operation.

$v_{||}$ Velocity parallel to the magnetic field.

$\underline{X}$ Gyrocentre position

ζ Binormal direction.

Appendix D

Conversion of parameter between GKW and GYRO

beta_ref The definition in GKW is

$$\text{beta} = \frac{2\mu_0 n_e T_e}{B_{ref}^2}, \tag{D.1}$$

while those of gyro is

$$\text{BETAE\_UNIT} = \frac{2\mu_0 n_e T_e}{B_{unit}^2}. \tag{D.2}$$

If the reference values for the density and temperature are the same, the conversion can thus be done with

$$c_{gs2\to gyro} = \left(\frac{B_{ref}}{B_{unit}}\right)^2 \tag{D.3}$$

$$c_{gyro\to gs2} = \left(\frac{B_{unit}}{B_{ref}}\right)^2 \tag{D.4}$$

See the paragraph "Reference magnetic field" for a description, how to get the ratio B_{unit}/B_{ref}.

Rmil The definitions in GKW and GYRO are the same (within the Miller-geometry), so the conversion factor is

$$c_{gyro\to gkw} = 1 \tag{D.5}$$

dRmil $\leftrightarrow$ SHIFT The definitions in GKW and GYRO are the same (within the Miller-geometry), so the conversion factor is

$$c_{gyro\to gkw} = 1 \tag{D.6}$$

Table D.1: Conversion of parameters and variables from GKW to GYRO.

Parameter GKW	Factor $c_{gkw\to gyro}$	Parameter GYRO
$k\rho$	$1/\sqrt{2}$	$k\rho$[1]
γ	$\frac{a}{R}\frac{v_{thref}}{c_s} = \frac{a}{\sqrt{2}R}$	γ
beta_ref	$\frac{8\pi}{2\mu_0}\frac{B_{ref}^2}{B_{unit}^2}$	BETAE_UNIT
eps	R/a	RADIUS
$\hat{s}$	1	$\hat{s}$
ω	$\frac{a}{R}\frac{v_{thref}}{c_s} = \frac{a}{\sqrt{2}R}$	ω
rlt	a/R	DLNTDR[2]
rln	a/R	DLNNDR
	Miller geometry	
Rmil	1	
dRmil	1	SHIFT
delta	1	DELTA
sdelta	$\sqrt{1-delta^2}$	S_DELTA
zmil	R/a	ZMAG

Zmil $\leftrightarrow$ ZMAG Definition in GKW is

$$\text{Zmil} = \frac{Z_0}{Rmil}, \tag{D.7}$$

with Z_0 the parameter from the geometry. The definition in GYRO is

$$\text{ZMAG} = \frac{Z_0}{a}, \tag{D.8}$$

thus the conversion factor is

$$c_{gyro\to gkw} = \frac{1}{\text{ASPECT\_RATIO}} \tag{D.9}$$

dZmil $\leftrightarrow$ DZMAG Definition in GKW is

$$\begin{aligned}
\text{dZmil} &= \frac{d\text{Zmil}}{dr} && \text{(D.10)}\\
&= \frac{d}{dr}\frac{Z_0}{Rmil} && \text{(D.11)}\\
&= \frac{1}{\text{Rmil}}\frac{dZ_0}{dr} - \frac{Z_0}{\text{Rmil}^2}\frac{d\text{Rmil}}{dr} && \text{(D.12)}\\
&= \frac{1}{\text{Rmil}}\left(\frac{dZ_0}{dr} - \text{ZmildRmil}\right), && \text{(D.13)}
\end{aligned}$$

and those in GYRO

$$\text{DZMAG} = \frac{dZ_0}{dr} \tag{D.14}$$

For the conversions we get the following relations

$$\text{dZmil} = \frac{1}{\text{Rmil}}\left(\text{DZMAG} - \frac{\text{ZMAG}}{\text{ASPECT\_RATIO}}\text{SHIFT}\right) \tag{D.15}$$

delta The definitions in GKW and GYRO are the same (within the Miller-geometry), so the conversion factor is

$$c_{gyro\to gkw} = 1 \tag{D.16}$$

sdelta Definition in GKW is

$$sdelta = \frac{r}{\sqrt{1-delta^2}}\frac{\partial delta}{\partial r}, \tag{D.17}$$

while those in GYRO is

$$S\_DELTA = r\frac{\partial delta}{\partial r}, \tag{D.18}$$

thus the conversion factor is

$$c_{gyro\to gkw} = \frac{1}{\sqrt{1-DELTA^2}} \tag{D.19}$$

kappa, skappa These are defined in the same way in GKW and GYRO, so no conversion needed.

square, ssquare These are defined in the same way in GKW and GYRO, so no conversion needed.

Reference magnetic field NOTE: This paragraph describes the conversion between GS2 and GYRO.
Reference value B_a for GS2 is the vacuum field at the centre midplane of the LCFS. In GYRO is the reference value $B_{unit} = B_0\rho/rd\rho/dr$ (r is the midplane minor radius, ρ is the radial coordinate using the square root of toroidal flux, divided by 2π, $\chi_t = B_0\rho^2/2$ and B_0 is the field at the reference major radius,

center midplane at surface of interest).
To get the connection between the two variables we use the two relations

$$\frac{\partial\psi}{\partial r} = \frac{r}{q}B_{unit} \qquad \text{Eq. 1.29 [124]} \tag{D.20}$$

$$\frac{\partial\psi}{\partial r} = \left(\frac{\partial\psi_N}{\partial\hat{r}}\right)^{GS2}\frac{B_a a_{ref}^2}{a_{ref}} \qquad [125], \tag{D.21}$$

(first from GYRO, second from GS2) where $\hat{r} = r/a_{ref}$ and a_{ref} is the GS2 normalizing scale length (here the midplane minor radius of the LCFS). From these we get the relation between B_{unit} and B_a

$$\frac{B_{unit}}{B_a} = \frac{q}{\hat{r}}\left(\frac{\partial\psi}{\partial\hat{r}}\right)^{GS2} \tag{D.22}$$

$$= \frac{q}{\hat{r}_{GYRO}}\left(\frac{\partial\psi}{\partial\hat{r}}\right)^{GS2}\frac{a_{ref}}{a_{ref,GYRO}} \tag{D.23}$$

For a conversion between GYRO and GKW one can use the same scheme, it must only taken into account that normalization in GKW is done with R, so the replacement $a_{ref} \to R_{ref}$ in the above equation has to be done.

Rotation velocity The definition in GKW is

$$\text{vcor} = \frac{R_{ref}\Omega}{v_{thref}} = \Omega_N \tag{D.24}$$

and those in GYRO

$$\text{MACH} = \frac{Romega}{c_s}. \tag{D.25}$$

The the conversion factor is therefore

$$c_{gyro\to gkw} = \frac{1}{\sqrt{2}} \tag{D.26}$$

due to $v_{thref}/c_s = \sqrt{2}$.

Rotation gradient The definition of GKW is

$$\text{uprim} = -\frac{R_{ref}^2\nabla\Omega}{v_{thref}}. \tag{D.27}$$

On the other hand the definition of GYRO is

$$\text{GAMMA\_P} = -R\frac{d(omega)}{dr}\frac{a}{c_s}. \tag{D.28}$$

Assuming $R = R_{ref}$ one gets due to $v_{thref}/c_s = \sqrt{2}$

$$c_{gyro\to gkw} = \frac{\text{ASPECT\_RATIO}}{\sqrt{2}} \tag{D.29}$$

$E \times B$ **shear** In GKW the shear is defined as

$$\text{shear\_rate} \quad = \tag{D.30}$$

which has to be compared with the definition of GYRO

$$\begin{aligned} \text{GAMMA\_E} &= -\frac{r}{q}\frac{d\omega}{dr}\frac{a}{c_s} && \text{(D.31)} \\ &= \frac{r}{qR}\text{GAMMA\_P}. && \text{(D.32)} \end{aligned}$$

Appendix E

Vector formulas

Vector formulas taken from Ref. [2]

$$\underline{a}\cdot(\underline{b}\times\underline{c}) = \underline{b}\cdot(\underline{c}\times\underline{a}) = \underline{c}\cdot(\underline{a}\times\underline{b}) \tag{E.1}$$

$$\underline{a}\times(\underline{b}\times\underline{c}) = (\underline{a}\cdot\underline{c})\underline{b} - (\underline{a}\cdot\underline{b})\underline{c} \tag{E.2}$$

$$(\underline{a}\times\underline{b})\cdot(\underline{c}\times\underline{d}) = (\underline{a}\cdot\underline{c})(\underline{b}\cdot\underline{d}) - (\underline{a}\cdot\underline{d})(\underline{b}\cdot\underline{c}) \tag{E.3}$$

$$\nabla\cdot(\phi\underline{a}) = \phi\nabla\cdot\underline{a} + (\underline{a}\cdot\nabla)\phi \tag{E.4}$$

$$\nabla\times(\phi\underline{a}) = (\nabla\phi)\times\underline{a} + \phi\nabla\times\underline{a} \tag{E.5}$$

$$\nabla(\underline{a}\cdot\underline{b}) = (\underline{a}\cdot\nabla)\underline{b} + (\underline{b}\cdot\nabla)\underline{a} + \underline{a}\times(\nabla\times\underline{b}) + \underline{b}\times(\nabla\times\underline{a}) \tag{E.6}$$

$$\nabla\cdot(\underline{a}\times\underline{b}) = \underline{b}\cdot\nabla\times\underline{a} - \underline{a}\cdot\nabla\times\underline{b} \tag{E.7}$$

$$\nabla\times(\underline{a}\times\underline{b}) = \underline{a}(\nabla\cdot\underline{b}) - \underline{b}(\nabla\cdot\underline{a}) + (\underline{b}\cdot\nabla)\underline{a} - (\underline{a}\cdot\nabla)\underline{b} \tag{E.8}$$

$$\nabla\times\nabla\times\underline{a} = \nabla(\nabla\cdot\underline{a}) - \nabla^2\underline{a} \tag{E.9}$$

Eq. (E.9) is only valid in Cartesian coordinates.

Appendix F

ITER reference values

The reference values for ITER parameters are

$$
\begin{aligned}
R_{ref} &= 6.2m && \text{(F.1)}\\
T_{ref} &= 8.5k\text{eV} && \text{(F.2)}\\
B_{ref} &= 5.3\text{T} && \text{(F.3)}\\
v_{thref} &= \sqrt{\frac{2T_{ref}}{m_{ref}}} && \text{(F.4)}\\
&= 905000\frac{m}{s} && \text{(F.5)}\\
\rho_{ref} &= \frac{m_{ref}v_{thref}}{qB_{ref}} = \frac{\sqrt{2Tm}}{qB} && \text{(F.6)}\\
&= 3.54\cdot 10^{-3}m = 3.54mm && \text{(F.7)}\\
\rho_* &= \frac{\rho_{ref}}{R_0} && \text{(F.8)}\\
&= 5.71\cdot 10^{-4} && \text{(F.9)}\\
t_{ref} &= \frac{R_{ref}}{v_{thref}} && \text{(F.10)}\\
&= 6.85\cdot 10^{-6}s = 6.85\mu s. && \text{(F.11)}
\end{aligned}
$$

Bibliography

[1] K. Ikeda, *ITER on the road to fusion energy*, Nuclear Fusion **50**, 014002 (2010).

[2] K. Miyamoto, *Controlled fusion and plasma physics*, Series in Plasma Physics, CRC Press Taylor & Francis Group, 6000 Broken Sound Parkway NW, Suite 300 (2007).

[3] J. Freidberg, *Plasma Physics and Fusion Energy*, Cambridge University Press, The Edinburgh Building, Cambridge CB2 8RU, UK, 1 edition (2007).

[4] A. H. Boozer, *Physics of magnetically confined plasmas*, Reviews of Modern Physics **76**, 1071 (2005).

[5] G. Grieger, W. Lotz, P. Merkel, J. Nührenberg, J. Sapper, E. Strumberger, H. Wobig, R. Burhenn, V. Erckmann, U. Gasparino, L. Giannone, H. J. Hartfuss, R. Jaenicke, G. Kühner, H. Ringler, A. Weller, F. Wagner, the W7–X Team and the W7–AS Team, *Physics optimization of stellarators*, Physics of Fluids B **4**, 2081 (1992).

[6] H.-S. Bosch, V. Erckmann, R. W. T. Konig, F. Schauer, R. J. Stadler and A. Werner, *Construction of Wendelstein 7-X–engineering a steady-state stellarator*, IEEE Transactions on Plasma Science **38**, 265 (2010).

[7] M. Kikuchi, *Steady state tokamak reactor based on the bootstrap current*, Nuclear Fusion **30**, 265 (1990).

[8] C. E. Kessel, *Bootstrap current in a tokamak*, Nuclear Fusion **34**, 1221 (1994).

[9] W. A. Houlberg, K. C. Shaing, S. P. Hirshman and M. C. Zarnstorff, *Bootstrap current and neoclassical transport in tokamaks of arbitrary collisionality and aspect ratio*, Physics of Plasmas **4**, 3230 (1997).

[10] T. Fujita, S. Ide, Y. Kamada, T. Suzuki, T. Oikawa, S. Takeji, Y. Sakamoto, Y. Koide, A. Isayama, T. Hatae, H. Kubo, S. Higashijima, O. Naito, H. Shirai and T. Fukuda, *Quasisteady high-confinement reversed shear*

plasma with large bootstrap current fraction under full noninductive current drive condition in JT-60U, Phys. Rev. Lett. **87**, 085001 (2001).

[11] P. A. Politzer, A. W. Hyatt, T. C. Luce, F. W. Perkins, R. Prater, A. D. Turnbull, D. P. Brennan, J. R. Ferron, C. M. Greenfield, J. Jayakumar, R. J. L. Haye, C. C. Petty and M. R. Wade, *Stationary, high bootstrap fraction plasmas in DIII-D without inductive current control*, Nuclear Fusion **45**, 417 (2005).

[12] F. Wagner, G. Becker, K. Behringer, D. Campbell, A. Eberhagen, W. Engelhardt, G. Fussmann, O. Gehre, J. Gernhardt, G. v. Gierke, G. Haas, M. Huang, F. Karger, M. Keilhacker, O. Klüber, M. Kornherr, K. Lackner, G. Lisitano, G. G. Lister, H. M. Mayer, D. Meisel, E. R. Müller, H. Murmann, H. Niedermeyer, W. Poschenrieder, H. Rapp, H. Röhr, F. Schneider, G. Siller, E. Speth, A. Stäbler, K. H. Steuer, G. Venus, O. Vollmer and Z. Yü, *Regime of improved confinement and high beta in neutral-beam-heated divertor discharges of the ASDEX tokamak*, Phys. Rev. Lett. **49**, 1408 (1982).

[13] I. H. Hutchinson, R. Boivin, F. Bombarda, P. Bonoli, S. Fairfax, C. Fiore, J. Goetz, S. Golovato, R. Granetz, M. Greenwald, S. Horne, A. Hubbard, J. Irby, B. LaBombard, B. Lipschultz, E. Marmar, G. McCracken, M. Porkolab, J. Rice, J. Snipes, Y. Takase, J. Terry, S. Wolfe, C. Christensen, D. Garnier, M. Graf, T. Hsu, T. Luke, M. May, A. Niemczewski, G. Tinios, J. Schachter and J. Urbahn, *First results from Alcator-C-MOD*, Physics of Plasmas **1**, 1511 (1994).

[14] O. Gruber, R. Arslanbekov, C. Atanasiu, A. Bard, G. Becker, W. Becker, M. Beckmann, K. Behler, K. Behringer, A. Bergmann, R. Bilato, D. Bolshukin, K. Borrass, H.-S. Bosch, B. Braams, M. Brambilla, R. Brandenburg, F. Braun, H. Brinkschulte, R. Brückner, B. Brüsehaber, K. Büchl, A. Buhler, H. Bürbaumer, A. Carlson, M. Ciric, G. Conway, D. P. Coster, C. Dorn, R. Drube, R. Dux, S. Egorov, W. Engelhardt, H.-U. Fahrbach, U. Fantz, H. Faugel, M. Foley, P. Franzen, P. Fu, J. C. Fuchs, J. Gafert, G. Gantenbein, O. Gehre, A. Geier, J. Gernhardt, E. Gubanka, A. Gude, S. Günter, G. Haas, D. Hartmann, B. Heinemann, A. Herrmann, J. Hobirk, F. Hofmeister, H. Hohenöcker, L. Horton, L. Hu, D. Jacobi, M. Jakobi, F. Jenko, A. Kallenbach, O. Kardaun, M. Kaufmann, A. Kendl, J.-W. Kim, K. Kirov, R. Kochergov, H. Kollotzek, W. Kraus, K. Krieger, B. Kurzan, G. Kyriakakis, K. Lackner, P. T. Lang, R. S. Lang, M. Laux, L. Lengyel, F. Leuterer, A. Lorenz, H. Maier, K. Mank, M.-E. Manso, M. Maraschek, K.-F. Mast, P. J. McCarthy, D. Meisel, H. Meister, F. Meo, R. Merkel, V. Mertens, J. Meskat, R. Monk, H. Müller,

M. Münich, H. Murmann, G. Neu, R. Neu, J. Neuhauser, J.-M. Noterdaeme, I. Nunes, G. Pautasso, A. G. Peeters, G. Pereverzev, S. Pinches, E. Poli, R. Pugno, G. Raupp, T. Ribeiro, R. Riedl, S. Riondato, V. Rohde, H. Röhr, J. Roth, F. Ryter, H. Salzmann, W. Sandmann, S. Sarelma, S. Schade, H.-B. Schilling, D. Schlögl, K. Schmidtmann, R. Schneider, W. Schneider, G. Schramm, J. Schweinzer, S. Schweizer, B. D. Scott, U. Seidel, F. Serra, S. Sesnic, C. Sihler, A. Silva, A. Sips, E. Speth, A. Stäbler, K.-H. Steuer, J. Stober, B. Streibl, E. Strumberger, W. Suttrop, A. Tabasso, A. Tanga, G. Tardini, C. Tichmann, W. Treutterer, M. Troppmann, N. Tsois, W. Ullrich, M. Ulrich, P. Varela, O. Vollmer, U. Wenzel, F. Wesner, R. Wolf, E. Wolfrum, R. Wunderlich, N. Xantopoulos, Q. Yu, M. Zarrabian, D. Zasche, T. Zehetbauer, H.-P. Zehrfeld, A. Zeiler and H. Zohm, *Overview of ASDEX Upgrade results*, Nuclear Fusion **41**, 1369 (2001).

[15] B. W. Rice, K. H. Burrell, L. L. Lao, G. Navratil, B. W. Stallard, E. J. Strait, T. S. Taylor, M. E. Austin, T. A. Casper, M. S. Chu, C. B. Forest, P. Gohil, R. J. Groebner, W. W. Heidbrink, A. W. Hyatt, H. Ikezi, R. J. L. Haye, E. A. Lazarus, Y. R. Lin-Liu, M. E. Mauel, W. H. Meyer, C. L. Rettig, D. P. Schissel, H. E. S. John, P. L. Taylor and A. D. T. the DIII-D Team, *Demonstration of high-performance negative central magnetic shear discharges in the DIII-D tokamak*, Physics of Plasmas **3**, 1983 (1996).

[16] B. Wan and I. Collaborators, *Recent experiments in the EAST and HT-7 superconducting tokamaks*, Nuclear Fusion **49**, 104011 (2009).

[17] JET Team, *Fusion energy production from a deuterium-tritium plasma in the JET tokamak*, Nuclear Fusion **32**, 187 (1992).

[18] T. Fukuda and the JT-60 Team, *Steady-state improved confinement studies in the JT-60U tokamak*, Physics of Plasmas **2**, 2249 (1995).

[19] R. J. Akers, J. W. Ahn, G. Y. Antar, L. C. Appel, D. Applegate, C. Brickley, C. Bunting, P. G. Carolan, C. D. Challis, N. J. Conway, G. F. Counsell, R. O. Dendy, B. Dudson, A. R. Field, A. Kirk, B. Lloyd, H. F. Meyer, A. W. Morris, A. Patel, C. M. Roach, V. Rohzansky, A. Sykes, D. Taylor, M. R. Tournianski, M. Valovic, H. R. Wilson, K. B. Axon, R. J. Buttery, D. Ciric, G. Cunningham, J. Dowling, M. R. Dunstan, S. J. Gee, M. P. Gryaznevich, P. Helander, D. L. Keeling, P. J. Knight, F. Lott, M. J. Loughlin, S. J. Manhood, R. Martin, G. J. McArdle, M. N. Price, K. Stammers, J. Storrs, M. J. Walsh and the MAST and NBI Team, *Transport and confinement in the mega ampère spherical tokamak (MAST) plasma*, Plasma Physics and Controlled Fusion **45**, A175 (2003).

[20] M. Ono, S. M. Kaye, Y.-K. M. Peng, G. Barnes, W. Blanchard, M. D. Carter, J. Chrzanowski, L. Dudek, R. Ewig, D. Gates, R. E. Hatcher, T. Jarboe, S. C. Jardin, D. Johnson, R. Kaita, M. Kalish, C. E. Kessel, H. W. Kugel, R. Maingi, R. Majeski, J. Manickam, B. McCormack, J. Menard, D. Mueller, B. A. Nelson, B. E. Nelson, C. Neumeyer, G. Oliaro, F. Paoletti, R. Parsells, E. Perry, N. Pomphrey, S. Ramakrishnan, R. Raman, G. Rewoldt, J. Robinson, A. L. Roquemore, P. Ryan, S. Sabbagh, D. Swain, E. J. Synakowski, M. Viola, M. Williams, J. R. Wilson and NSTX Team, *Exploration of spherical torus physics in the NSTX device*, Nuclear Fusion **40**, 557 (2000).

[21] A. Peeters, Y. Camenen, F. Casson, W. A. Hornsby, A. P. Snodin, D. Strintzi and G. Szepesi, *The nonlinear gyro-kinetic flux tube code GKW*, Computer Physics Communications **180**, 2650 (2009).

[22] A. G. Peeters, Y. Camenen, F. J. Casson, W. A. Hornsby, P. Manas, A. P. Snodin, D. Strintzi and G. Szepesi, *Gkw source*, https://bitbucket.org/gkw/gkw.git.

[23] A. A. Vlasov, *The vibrational properties of an electron gas*, Soviet Physics Uspekhi **10**, 721 (1968).

[24] Y. Camenen, A. G. Peeters, C. Angioni, F. J. Casson, W. A. Hornsby, A. P. Snodin and D. Strintzi, *Impact of the background toroidal rotation on particle and heat turbulent transport in tokamak plasmas*, Physics of Plasmas **16**, 012503 (2009).

[25] A. G. Peeters, D. Strintzi, Y. Camenen, C. Angioni, F. J. Casson, W. A. Hornsby and A. P. Snodin, *Influence of the centrifugal force and parallel dynamics on the toroidal momentum transport due to small scale turbulence in a tokamak*, Physics of Plasmas **16**, 042310 (2009).

[26] A. G. Peeters, D. Strintzi, Y. Camenen, C. Angioni, F. J. Casson, W. A. Hornsby and A. P. Snodin, *Erratum: "influence of the centrifugal force and parallel dynamics on the toroidal momentum transport due to small scale turbulence in a tokamak" [Phys. Plasmas 16, 042310 (2009)]*, Physics of Plasmas **19**, 099901 (2012).

[27] H. Biglari, P. H. Diamond and P. W. Terry, *Influence of sheared poloidal rotation on edge turbulence*, Physics of Fluids B **2**, 1 (1990).

[28] R. C. Wolf, *Internal transport barriers in tokamak plasmas*, Plasma Physics and Controlled Fusion **45**, R1 (2003).

[29] A. Bondeson and D. J. Ward, *Stabilization of external modes in tokamaks by resistive walls and plasma rotation*, Phys. Rev. Lett. **72**, 2709 (1994).

[30] Y. Camenen, Y. Idomura, S. Jolliet and A. Peeters, *Consequences of profile shearing on toroidal momentum transport*, Nuclear Fusion **51**, 073039 (2011).

[31] A. G. Peeters, Y. Camenen, F. J. Casson, W. A. Hornsby, P. Manas, A. P. Snodin, D. Strintzi and G. Szepesi, *GKW how and why*, various, various (2014), still in development.

[32] G. Szepsi, *Derivation of the fully electro-magnetic, non-linear, gyrokinetic Vlasov–Maxwell equations in a rotating frame of reference for gkw with Lie transform perturbation method* (2012), part of gkw documentation.

[33] A. J. Brizard and T. S. Hahm, *Foundations of nonlinear gyrokinetic theory*, Reviews of Modern Physics **79**, 421 (2007).

[34] F. J. Casson, *Turbulent transport in rotating tokamak plasmas*, Phd thesis, Department of Physics, University of Warwick (2011).

[35] A. J. Brizard, *Nonlinear gyrokinetic Vlasov equation for toroidally rotating axisymmetric tokamaks*, Physics of Plasmas **2**, 459 (1995).

[36] J. W. Connor, R. J. Hastie and J. B. Taylor, *Shear, periodicity, and plasma ballooning modes*, Physical Review Letters **40**, 396 (1978).

[37] X. Lapillonne, S. Brunner, T. Dannert, S. Jolliet, A. Marinoni, L. Villard, T. Görler, F. Jenko and F. Merz, *Clarifications to the limitations of the $s-\alpha$ equilibrium model for gyrokinetic computations of turbulence*, Physics of Plasmas **16**, 032308 (2009).

[38] R. L. Miller, M. S. Chu, J. M. Greene, Y. R. Lin-Liu and R. E. Waltz, *Noncircular, finite aspect ratio, local equilibrium model*, Physics of Plasmas **5**, 973 (1998).

[39] R. E. Waltz, G. D. Kerbel and J. Milovich, *Toroidal gyro-Landau fluid model turbulence simulations in a nonlinear ballooning mode representation with radial modes*, Physics of Plasmas **1**, 2229 (1994).

[40] T. S. Hahm and K. H. Burrell, *Flow shear induced fluctuation suppression in finite aspect ratio shaped tokamak plasma*, Physics of Plasmas **2**, 1648 (1995).

[41] L.-G. Eriksson, E. Righi and K.-D. Zastrow, *Toroidal rotation in ICRF-heated H-modes on JET*, Plasma Physics and Controlled Fusion **39**, 27 (1997).

[42] J. E. Rice, M. Greenwald, I. H. Hutchinson, E. S. Marmar, Y. Takase, S. M. Wolfe and F. Bombarda, *Observations of central toroidal rotation in ICRF heated Alcator C-Mod plasmas*, Nuclear Fusion **38**, 75 (1998).

[43] I. H. Hutchinson, J. E. Rice, R. S. Granetz and J. A. Snipes, *Self-acceleration of a tokamak plasma during ohmic h mode*, Phys. Rev. Lett. **84**, 3330 (2000).

[44] A. G. Peeters and C. Angioni, *Linear gyrokinetic calculations of toroidal momentum transport in a tokamak due to the ion temperature gradient mode*, Physics of Plasmas **12**, 072515 (2005).

[45] F. I. Parra, M. Barnes and A. G. Peeters, *Up-down symmetry of the turbulent transport of toroidal angular momentum in tokamaks*, Physics of Plasmas **18**, 062501 (2011).

[46] A. G. Peeters, C. Angioni, A. Bortolon, Y. Camenen, F. J. Casson, B. Duval, L. Fiederspiel, W. A. Hornsby, Y. Idomura, T. Hein, N. Kluy, P. Mantica, F. I. Parra, A. P. Snodin, G. Szepesi, D. Strintzi, T. Tala, G. Tardini, P. de Vries and J. Weiland, *Overview of toroidal momentum transport*, Nuclear Fusion **51**, 094027 (2011).

[47] V. Hernandez, J. E. Roman and V. Vidal, *SLEPc: A scalable and flexible toolkit for the solution of eigenvalue problems*, ACM Trans. Math. Software **31**, 351 (2005).

[48] S. Balay, J. Brown, K. Buschelman, V. Eijkhout, W. D. Gropp, D. Kaushik, M. G. Knepley, L. C. McInnes, B. F. Smith and H. Zhang, *PETSc users manual*, Technical Report ANL-95/11 - Revision 3.3, Argonne National Laboratory (2012).

[49] J. E. Roman, C. Campos, E. Romero and A. Tomas, *SLEPc users manual*, Technical Report DSIC-II/24/02 - Revision 3.6, D. Sistemes Informàtics i Computació, Universitat Politècnica de València (2015).

[50] Y. Saad, *Iterative Methods for Sparse Linear Systems*, Society for Industrial and Applied Mathematics, 3600 University Science Center, Philadelphia, PA 19104-2688, 2 edition (2003).

[51] V. Hernández, J. E. Román, A. Tomás and V. Vidal, *Arnoldi methods in SLEPc*, Technical Report STR-4, Universitat Politècnica de València (2006), available at http://www.grycap.upv.es/slepc.

[52] V. Hernández, J. E. Román, A. Tomás and V. Vidal, *Krylov-Schur methods in SLEPc*, Technical Report STR-7, Universitat Politècnica de València (2007), available at http://www.grycap.upv.es/slepc.

[53] J. E. Román, *Practical implementation of harmonic Krylov-Schur*, Technical Report STR-9, Universitat Politècnica de València (2009), available at http://www.grycap.upv.es/slepc.

[54] J. E. Roman, M. Kammerer, F. Merz and F. Jenko, *Fast eigenvalue calculations in a massively parallel plasma turbulence code*, Parallel Computing **36**, 339 (2010).

[55] F. J. Casson, E. Poli, C. Angioni, R. Buchholz and A. G. Peeters, *Effect of turbulence on electron cyclotron current drive and heating in iter*, Nuclear Fusion **55**, 012002 (2015).

[56] R. Buchholz, Y. Camenen, F. J. Casson, S. R. Grosshauser, W. A. Hornsby, P. Migliano and A. G. Peeters, *Toroidal momentum transport in a tokamak due to profile shearing*, Physics of Plasmas **21**, 062304 (2014).

[57] R. E. Waltz, G. D. Kerbel, J. Milovich and G. W. Hammett, *Advances in the simulation of toroidal gyro-landau fluid model turbulence*, Physics of Plasmas **2**, 2408 (1995).

[58] G. M. Staebler, R. E. Waltz, J. Candy and J. E. Kinsey, *New paradigm for suppression of gyrokinetic turbulence by velocity shear*, Physical Review Letters **110**, 055003 (2013).

[59] J. E. Rice, P. T. Bonoli, J. A. Goetz, M. J. Greenwald, I. H. Hutchinson, E. S. Marmar, M. Porkolab, S. M. Wolfe, S. J. Wukitch and C. S. Chang, *Central impurity toroidal rotation in ICRF heated Alcator C-Mod plasmas*, Nuclear Fusion **39**, 1175 (1999).

[60] J. E. Rice, J. A. Goetz, R. S. Granetz, M. J. Greenwald, A. E. Hubbard, I. H. Hutchinson, E. S. Marmar, D. Mossessian, T. S. Pedersen, J. A. Snipes, J. L. Terry and S. M. Wolfe, *Impurity toroidal rotation and transport in Alcator C-Mod ohmic high confinement mode plasmas*, Physics of Plasmas **7**, 1825 (2000).

[61] G. T. Hoang, P. Monier-Garbet, T. Aniel, C. Bourdelle, R. V. Budny, F. Clairet, L.-G. Eriksson, X. Garbet, C. Grisolia, P. Platz and J. C. Vallet, *An h minority heating regime in tore supra showing improved l mode confinement*, Nuclear Fusion **40**, 913 (2000).

[62] J. S. deGrassie, K. H. Burrell, L. R. Baylor, W. Houlberg and J. Lohr, *Toroidal rotation in DIII-D in electron cyclotron heating and ohmic h-mode discharges*, Physics of Plasmas **11**, 4323 (2004).

[63] M. Yoshida, Y. Koide, H. Takenaga, H. Urano, N. Oyama, K. Kamiya, Y. Sakamoto, G. Matsunaga, Y. Kamada and the JT-60 Team, *Momentum*

transport and plasma rotation profile in toroidal direction in JT-60U L-mode plasmas, Nuclear Fusion **47**, 856 (2007).

[64] A. Scarabosio, A. Bortolon, B. P. Duval, A. Karpushov and A. Pochelon, *Toroidal plasma rotation in the tcv tokamak*, Plasma Physics and Controlled Fusion **48**, 663 (2006).

[65] A. Bortolon, B. P. Duval, A. Pochelon and A. Scarabosio, *Observation of spontaneous toroidal rotation inversion in ohmically heated tokamak plasmas*, Physical Review Letters **97**, 235003 (2006).

[66] J. E. Rice, A. Ince-Cushman, J. S. deGrassie, L.-G. Eriksson, Y. Sakamoto, A. Scarabosio, A. Bortolon, K. H. Burrell, B. P. Duval, C. Fenzi-Bonizec, M. J. Greenwald, R. J. Groebner, G. T. Hoang, Y. Koide, E. S. Marmar, A. Pochelon and Y. Podpaly, *Inter-machine comparison of intrinsic toroidal rotation in tokamaks*, Nuclear Fusion **47**, 1618 (2007).

[67] Y. Camenen, A. Bortolon, B. P. Duval, L. Federspiel, A. G. Peeters, F. J. Casson, W. A. Hornsby, A. N. Karpushov, F. Piras, O. Sauter, A. P. Snodin, G. Szepesi and the TCV Team, *Experimental demonstration of an up-down asymmetry effect on intrinsic rotation in the TCV tokamak*, Plasma Physics and Controlled Fusion **52**, 124037 (2010).

[68] N. Mattor and P. H. Diamond, *Momentum and thermal transport in neutral-beam-heated tokamaks*, Physics of Fluids **31**, 1180 (1988).

[69] A. G. Peeters, C. Angioni and D. Strintzi, *Toroidal momentum pinch velocity due to the coriolis drift effect on small scale instabilities in a toroidal plasma*, Physical Review Letters **98**, 265003 (2007).

[70] T. S. Hahm, P. H. Diamond, O. D. Gurcan and G. Rewoldt, *Nonlinear gyrokinetic theory of toroidal momentum pinch*, Physics of Plasmas **14**, 072302 (2007).

[71] Y. Camenen, A. G. Peeters, C. Angioni, F. J. Casson, W. A. Hornsby, A. P. Snodin and D. Strintzi, *Transport of parallel momentum induced by current-symmetry breaking in toroidal plasmas*, Physical Review Letters **102**, 125001 (2009).

[72] Y. Camenen, A. G. Peeters, C. Angioni, F. J. Casson, W. A. Hornsby, A. P. Snodin and D. Strintzi, *Intrinsic rotation driven by the electrostatic turbulence in up-down asymmetric toroidal plasmas*, Physics of Plasmas **16**, 062501 (2009).

[73] F. I. Parra and P. J. Catto, *Turbulent transport of toroidal angular momentum in low flow gyrokinetics*, Plasma Physics and Controlled Fusion **52**, 045004 (2010).

[74] R. R. Dominguez and G. M. Staebler, Physics of Fluids B **5** (1993).

[75] X. Garbet, Y. Sarazin, P. Ghendrih, S. Benkadda, P. Beyer, C. Figarella and I. Voitsekhovitch, *Turbulence simulations of transport barriers with toroidal velocity*, Physics of Plasmas **9**, 3893 (2002).

[76] O. D. Gürcan, P. H. Diamond, T. S. Hahm and R. Singh, *Intrinsic rotation and electric field shear*, Physics of Plasmas **14**, 042306 (2007).

[77] R. E. Waltz, G. M. Staebler, J. Candy and F. L. Hinton, *Gyrokinetic theory and simulation of angular momentum transport*, Physics of Plasmas **14**, 122507 (2007).

[78] F. J. Casson, A. G. Peeters, Y. Camenen, W. A. Hornsby, A. P. Snodin, D. Strintzi and G. Szepesi, *Anomalous parallel momentum transport due to $e \times b$ flow shear in a tokamak plasma*, Physics of Plasmas **16**, 092303 (2009).

[79] O. D. Gürcan, P. H. D. P. Hennequin, C. J. McDevitt, X. Garbet and C. Bourdelle, *Residual parallel Reynolds stress due to turbulence intensity gradient in tokamak plasmas*, Physics of Plasmas **17**, 112309 (2010).

[80] R. E. Waltz, G. M. Staebler and W. M. Solomon, *Gyrokinetic simulation of momentum transport with residual stress from diamagnetic level velocity shears*, Physics of Plasmas **18**, 042504 (2011).

[81] T. Sung, R. Buchholz, F. J. Casson, E. Fable, S. R. Grosshauser, W. A. Hornsby, P. Migliano and A. G. Peeters, *Toroidal momentum transport in a tokamak caused by symmetry breaking parallel derivatives*, Physics of Plasmas **20**, 042506 (2013).

[82] Y. Idomura, *Full-f gyrokinetic simulation over a confinement time*, Physics of Plasmas **21**, 022517 (2014).

[83] C. Angioni, R. M. McDermott, F. J. Casson, E. Fable, A. Bottino, R. Dux, R. Fischer, Y. Podoba, T. Pütterich, F. Ryter, E. Viezzer and ASDEX Upgrade Team, *Intrinsic toroidal rotation, density peaking, and turbulence regimes in the core of tokamak plasmas*, Physical Review Letters **107**, 215003 (2011).

[84] M. Barnes, F. I. Parra, J. P. Lee, E. A. Belli, M. F. F. Nave and A. E. White, *Intrinsic rotation driven by non-maxwellian equilibria in tokamak plasmas*, Phys. Rev. Lett. **111**, 055005 (2013).

[85] Y. Kishimoto, J.-Y. Kim, W. Horton, T. Tajima, M. J. LeBrun and H. Shirai, *Toroidal mode structure in weak and reversed magnetic shear*

plasmas and its role in the internal transport barrier, Plasma Physics and Controlled Fusion **41**, A663 (1999).

[86] Z. Lin, S. Ethier, T. S. Hahm and W. M. Tang, *Size scaling of turbulent transport in magnetically confined plasmas*, Physical Review Letters **88**, 195004 (2002).

[87] J. Candy, R. E. Waltz and W. Dorland, *The local limit of global gyrokinetic simulations*, Physics of Plasmas **11**, L25 (2004).

[88] B. F. McMillan, X. Lapillonne, S. Brunner, , L. Villard, S. Jolliet, A. Bottino, T. Görler and F. Jenko, *System size effects on gyrokinetic turbulence*, Physical Review Letters **105**, 155001 (2010).

[89] J. Kinsey, *The gyro nonlinear gyrokinetic simulation database*, Technical Report (2008), available at https://github.com/gafusion/doc/raw/master/database/gyro-database.pdf.

[90] J. Candy, R. E. Waltz, S. E. Parker and Y. Chen, *Relevance of the parallel nonlinearity in gyrokinetic simulations of tokamak plasmas*, Physics of Plasmas **13**, 074501 (2006).

[91] Z. Lin, G. Rewoldt, S. Ethier, T. S. Hahm, W. W. Lee, J. L. V. Lewandowski, Y. Nishimura and W. X. Wang, *Particle-in-cell simulations of electron transport from plasma turbulence: recent progress in gyrokinetic particle simulations of turbulent plasmas*, Journal of Physics: Conference Series **16**, 16 (2005).

[92] R. Buchholz, S. Grosshauser, W. Guttenfelder, W. A. Hornsby, P. Migliano, A. G. Peeters and D. Strintzi, *Influence of centrifugal effects on particle and momentum transport in national spherical torus experiment*, Physics of Plasmas **22**, 082307 (2015).

[93] P. J. Catto, M. N. Rosenbluth and C. S. Liu, *Parallel velocity shear instabilities in an inhomogeneous plasma with a sheared magnetic field*, Physics of Fluids **16**, 1719 (1973).

[94] F. J. Casson, A. G. Peeters, C. Angioni, Y. Camenen, W. A. Hornsby, A. P. Snodin and G. Szepesi, *Gyrokinetic simulations including the centrifugal force in a rotating tokamak plasma*, Physics of Plasmas **17**, 102305 (2010).

[95] Y.-K. M. Peng and D. J. Strickler, *Features of spherical torus plasmas*, Nuclear Fusion **26**, 769 (1986).

[96] Y.-K. M. Peng, *The physics of spherical torus plasmas*, Physics of Plasmas **7**, 1681 (20000).

[97] S. M. Kaye, W. Solomon, R. E. Bell, B. P. LeBlanc, F. Levinton, J. Menard, G. Rewoldt, S. Sabbagh, W. Wang and H. Yuh, *Momentum transport in electron-dominated NSTX spherical torus plasmas*, Nuclear Fusion **49**, 045010 (2009).

[98] W. Guttenfelder, J. L. Peterson, J. Candy, S. M. Kaye, Y. Ren, R. E. Bell, G. W. Hammett, B. LeBlanc, D. R. Mikkelsen, W. M. Nevins and H. Yuh, *Progress in simulating turbulent electron thermal transport in NSTX*, Nuclear Fusion **53**, 093022 (2013).

[99] F. J. Casson, R. M. McDermott, C. Angioni, Y. Camenen, R. Dux, E. Fable, R. Fischer, B. Geiger, P. Manas, L. Menchero, G. Tardini and the ASDEX Upgrade Team, *Validation of gyrokinetic modelling of light impurity transport including rotation in ASDEX Upgrade*, Nuclear Fusion **53**, 063026 (2013).

[100] F. Scotti, V. A. Soukhanovskii, R. E. Bell, S. Gerhardt, W. Guttenfelder, S. Kaye, R. Andre, A. Diallo, R. Kaita, B. P. LeBlanc, M. Podestá and the NSTX Team, *Core transport of lithium and carbon in ELM-free discharges with lithium wall conditioning in NSTX*, Nuclear Fusion **53**, 083001 (2013).

[101] L. Delgado-Aparicio, D. Stutman, K. Tritz, M. Finkenthal, S. Kaye, R. Bell, R. Kaita, B. LeBlanc, F. Levinton, J. Menard, S. Paul, D. Smith and H. Yuh, *Impurity transport studies in NSTX neutral beam heated H-mode plasmas*, Nuclear Fusion **49**, 085028 (2009).

[102] L. Delgado-Aparicio, D. Stutman, K. Tritz, F. Volpe, K. L. Wong, R. Bell, M. Finkenthal, E. Fredrickson, S. P. Gerhardt, S. Kaye, B. LeBlanc, J. Menard, S. Paul and L. Roquemore, *Impurity transport experiments and effects on MHD in the national spherical torus experiment (NSTX)*, Nuclear Fusion **51**, 083047 (2011).

[103] D. J. Clayton, K. Tritz, D. Stutman, M. Finkenthal, S. M. Kaye, D. Kumar, B. P. LeBlanc, S. Paul and S. A. Sabbagh, *Multi-energy soft-x-ray technique for impurity transport measurements in the fusion plasma edge*, Plasma Physics and Controlled Fusion **54**, 105022 (2012).

[104] R. Maingi, T. H. Osborne, B. P. LeBlanc, R. E. Bell, J. Manickam, P. B. Snyder, J. E. Menard, D. K. Mansfield, H. W. Kugel, R. Kaita, S. P. Gerhardt, S. A. Sabbagh and F. A. Kelly, *Edge-localized-mode suppression through density-profile modification with lithium-wall coatings in the national spherical torus experiment*, Physical Review Letters **103**, 075001 (2009).

[105] S. M. Kaye, S. Gerhardt, W. Guttenfelder, R. Maingi, R. E. Bell, A. Diallo, B. P. LeBlanc and M. Podesta, *The dependence of H-mode energy confinement and transport on collisionality in NSTX*, Nuclear Fusion **53**, 063005 (2013).

[106] W. Guttenfelder, J. Candy, S. M. Kaye, W. M. Nevins, E. Wang, R. E. Bell, G. W. Hammett, B. P. LeBlanc, D. R. Mikkelsen and H. Yuh, *Electromagnetic transport from microtearing mode turbulence*, Physical Review Letters **106**, 155004 (2011).

[107] H. Doerk, F. Jenko, M. J. Pueschel and D. R. Hatch, *Gyrokinetic microtearing turbulence*, Phys. Rev. Lett. **106**, 155003 (2011).

[108] W. Guttenfelder, J. Candy, S. M. Kaye, W. M. Nevins, R. E. Bell, G. W. Hammett, B. P. LeBlanc and H. Yuh, *Scaling of linear microtearing stability for a high collisionality national spherical torus experiment discharge*, Physics of Plasmas **19**, 022506 (2012).

[109] W. Guttenfelder, J. Candy, S. M. Kaye, W. M. Nevins, E. Wang, J. Zhang, R. E. Bell, N. A. Crocker, G. W. Hammett, B. P. LeBlanc, D. R. Mikelsen, Y. Ren and H. Yuh, *Simulation of microtearing turbulence in national spherical torus experiment*, Physics of Plasmas **19**, 056119 (2012).

[110] J. Candy and R. Waltz, *An eulerian gyrokinetic-maxwell solver*, Journal of Computational Physics **186**, 545 (2003).

[111] M. Podestà, R. E. Bell, A. Diallo, B. P. LeBlanc, F. Scotti and the NSTX Team, *Measurements of core lithium concentration in a Li-conditioned tokamak with carbon walls*, Nuclear Fusion **52**, 033008 (2012).

[112] E. A. Belli and J. Candy, *Fully electromagnetic gyrokinetic eigenmode analysis of high-beta shaped plasmas*, Physics of Plasmas **17**, 112314 (2010).

[113] S. Moradi, I. Pusztai, W. Guttenfelder, T. Fülöp and A. Mollén, *Microtearing modes in spherical and conventional tokamaks*, Nuclear Fusion **53**, 063025 (2013).

[114] S. Moradi, I. Pusztai, A. Mollén and T. Fülöp, *Impurity transport due to electromagnetic drift wave turbulence*, Physics of Plasmas **19**, 032301 (2012).

[115] G. F. Matthews, M. Beurskens, S. Brezinsek, M. Groth, E. Joffrin, A. Loving, M. Kear, M.-L. Mayoral, R. Neu, P. Prior, V. Riccardo, F. Rimini, M. Rubel, G. Sips, E. Villedieu, P. de Vries, M. L. Watkins and EFDA-JET contributors, *JET ITER-like wall–overview and experimental programme*, Physica Scripta **2011**, 014001 (2011).

[116] D. Strintzi, A. G. Peeters and J. Weiland, *The toroidal momentum diffusivity in a tokamak plasma: A comparison of fluid and kinetic calculations*, Physics of Plasmas **15**, 044502 (2008).

[117] T. Hein, C. Angioni, E. Fable, J. Candy and A. G. Peeters, *Gyrokinetic study of electromagnetic effects on toroidal momentum transport in tokamak plasmas*, Physics of Plasmas **18**, 072503 (2011).

[118] J. E. Menard, S. Gerhardt, M. Bell, J. Bialek, A. Brooks, J. Canik, J. Chrzanowski, M. Denault, L. Dudek, D. A. Gates, N. Gorelenkov, W. Guttenfelder, R. Hatcher, J. Hosea, R. Kaita, S. Kaye, C. Kessel, E. Kolemen, H. Kugel, R. Maingi, M. Mardenfeld, D. Mueller, B. Nelson, C. Neumeyer, M. Ono, E. Perry, R. Ramakrishnan, R. Raman, Y. Ren, S. Sabbagh, M. Smith, V. Soukhanovskii, T. Stevenson, R. Strykowsky, D. Stutman, G. Taylor, P. Titus, K. Tresemer, K. Tritz, M. Viola, M. Williams, R. Woolley, H. Yuh, H. Zhang, Y. Zhai, A. Zolfaghari and the NSTX Team, *Overview of the physics and engineering design of NSTX upgrade*, Nuclear Fusion **52**, 083015 (2012).

[119] J. M. Greene and M. S. Chance, *The second region of stability against ballooning modes*, Nuclear Fusion **21**, 453 (1981).

[120] A. . G. Peeters, *The bootstrap current and its consequences*, Plasma Physics and Controlled Fusion **42**, B231 (2000).

[121] P. B. Snyder, *Gyrofluid theory and simulation of electromagnetic turbulence and transport in tokamak plasmas*, Ph.d., Princeton University (1999).

[122] D. J. Applegate, C. M. Roach, J. W. Connor, S. C. Cowley, W. Dorland, R. J. Hastie and N. Joiner, *Micro-tearing modes in the mega ampere spherical tokamak*, Plasma Physics and Controlled Fusion **49**, 1113 (2007).

[123] R. E. Waltz, *Rho-star scaling and physically realistic gyrokinetic simulations of transport in DIII-D*, Fusion Science and Technology **48**, 1051 (2005).

[124] J. Candy, *GYRO Technical Guide* (2012).

[125] W. Dorland and M. Kotschenreuther, *Notes on Local Equilibrium Implementation* (2012), http://gs2.sourceforge.net.

Index